Oncogenic virus hijacks SOX18 pioneer function to enhance viral persistence

Krista Tuohinto[1]*, Matthew S. Graus[2]*, Peyton Staab[1], Ville Tiusanen[3], Fei Liangru[4,5], Susav Pradhan[2], Yew Yan Wong[2], Simon Weissmann[6], Jieqiong Lou[7], Elizabeth Hinde[7], Justin Wong[2], Quintin Lee[2], Alexey Terskikh[8], Martin Alvarez-Kuglen[8], Tara Karnezis[9], Thomas Günther[6], Adam Grundhoff[6], Biswajyoti Sahu[3,4,5], Mathias Francoís[2#], Päivi M. Ojala[1,10#]

[1] Translational Cancer Medicine Research Program, University of Helsinki, Finland.
[2] The University of Sydney, School of Medical Sciences, Sydney, New South Wales, 2006, Australia.
[3] Applied Tumor Genomics Research Program, University of Helsinki, Finland.
[4] Norwegian Center for Molecular Biosciences and Medicine, University of Oslo, Norway.
[5] Institute for Cancer Research, Department of Cancer Genetics, Oslo University Hospital, Norway.
[6] Leibniz Institute of Virology, Germany.
[7] The University of Melbourne, School of Physics, Melbourne, Victoria, 3010, Australia.
[8] Harry Perkins Institute of Medical Research, The University of Western Australia, Australia.
[9] Gertrude Biomedical Pty Ltd., Bio21, Melbourne, Victoria, Australia.
[10] Department of Pathology, Medicum, Faculty of Medicine, University of Helsinki, Finland.

** Equal contribution.*
[#] Corresponding authors.

Päivi Ojala (Tel: +358 50 3377557)
paivi.ojala@helsinki.fi
Mathias Francois (Tel: +61 28627 9497)
mathias.francois@sydney.edu.au

***Keywords**:* Transcription factor, pioneer, SOX18, BRG1, KSHV, herpesvirus, small molecule inhibitor, endothelial cell, chromatin

Brief title: Oncogenic virus takes control of SOX18 pioneer function for its genome persistence

Abstract

Kaposi's sarcoma herpesvirus (KSHV) establishes lifelong oncogenic infection in lymphatic endothelial cells (LECs) by ensuring episomal maintenance of its genome via the viral protein LANA. Efficient viral genome maintenance typically involves host DNA replication and episome tethering, but the extent of cell-type-specific regulation remains unclear. Here, we identify that KSHV hijacks the pioneering function of the endothelial-specific transcription factor SOX18 to facilitate persistence of viral episomes. Upon infection, LANA co-opts SOX18 to recruit the SWI/SNF chromatin-remodeling complex via its ATPase subunit BRG1, enhancing chromatin accessibility and enabling efficient viral genome persistence. Disruption of SOX18 or BRG1—genetically or pharmacologically—leads to reduced episome load and attenuated hallmarks of virus infection. This work highlights how viruses can harness lineage-specific transcriptional regulators to establish persistent nuclear retention of their episome into the host genome.

Introduction

Kaposi's sarcoma (KS) is caused by an oncogenic human gamma herpesvirus (KSHV/HHV-8), during periods of immune deficiencies such as organ transplantations and among the 40 million people living with HIV worldwide. KS is considered to originate from endothelial cells and consists of excessive malformed vasculature with KSHV-infected spindle-shaped cells as a pathological hallmark (Gramolelli & Ojala, 2017). Due to the paucity of validated molecular targets, and a limited understanding of the molecular mechanisms that underpin long-term persistence, there is a clear limitation of current KS therapies, of which none are curative. Clinical outcomes are unfavorable especially in the lower income countries with the highest KS burden, such as sub-equatorial Africa, where it remains life-threatening for patients resistant to advanced anti-retroviral therapy (ART) (Cesarman et al., 2019).

We and others have shown that lymphatic endothelial cells (LEC) are exceptionally susceptible to KSHV infection in striking contrast to other cell types (Choi et al., 2020; DiMaio et al., 2020; Golas et al., 2019; Gramolelli et al., 2020). KSHV can reprogram blood vascular endothelial cells (BECs) toward a lymphatic endothelial-like state, driving a Kaposi's sarcoma (KS) gene signature that more closely resembles LECs than BECs (Aguilar et al., 2012; Carroll et al., 2004; Hong et al., 2004; Wang et al., 2004). Remarkably, when KSHV infects LECs, the resulting KLECs undergo profound changes in morphology, proliferation, and identity—acquiring features characteristic of KS spindle cells (Cheng et al., 2011; Gasperini et al., 2012; Ojala & Schulz, 2014). However, the stepwise progression of the virus-driven molecular mechanisms that underpin this cell transformation are not well understood.

Latency is considered the default, quiescent mode of infection, where the circularized dsDNA KSHV genome persists as an extrachromosomal episome attached to host chromatin. A switch to lytic replication, triggered by the viral ORF50/RTA gene leads to the expression of all viral genes, resulting in the production and release of new virus particles (Han et al., 2024). Persistence of KSHV episomes is crucial for the establishment of a lifelong infection and for clinically evident KS to develop. KSHV Latency-Associated Nuclear Antigen (LANA) is required for tethering the viral episomes to host chromatin and for enabling KSHV to exploit the host replication machinery to replicate and maintain viral DNA in latently infected host cells (Ballestas & Kaye, 2001; Purushothaman et al., 2016; Uppal et al., 2014). LANA binds to the conserved terminal repeat (TR) sequences on the KSHV genome through its C-terminal domain and docks onto the host chromatin via histones H2A/B through its N-terminal domain (Barbera et al., 2006). Thus, LANA is required for viral episome tethering, latent replication and maintenance of the replicated genomes in daughter cells during mitosis. While LANA has been shown to generally bind to open or active chromatin (Hu et al., 2014; Kumar et al., 2022; Lotke et al., 2020; Lu et al., 2012; Mercier et al., 2014; Ye et al., 2024), how LANA may select for specific chromatin regions and which protein complexes are involved in stabilizing viral genomes remains a major question in the field.

KLECs display a unique infection program characterized by high numbers of intracellular viral episomes. In our previous work, we showed that SOX18 and PROX1, two key developmental transcription factors (TFs) for LEC fate, are widely expressed in KS tumors and critical to support this unique KSHV infection program in LECs by two distinct mechanisms (Gramolelli et al., 2020). SOX18 binds to the KSHV origins of replication, and its expression increases viral genome copies, while PROX1 plays a role in the reactivation of the lytic cycle.

The SOX18 TF is essential for embryonic development. It belongs to the SOXF group, which plays a role in vascular development angiogenesis, wound healing and cancer metastasis (Downes & Koopman, 2001; Schock & LaBonne, 2020). It is also involved in LEC differentiation by co-regulating PROX1 with NR2F2, a key regulator of lymphatic cell identity (Aranguren et al., 2013; Duong et al., 2012; Francois et al., 2008; Srinivasan et al., 2010). Because of its role in solid cancer development, SOX18 has long been a target for drug development. Despite long-standing challenges in targeting TFs with small molecules, the SOX18 inhibitor, Sm4, was identified (Fontaine et al., 2017; Overman et al., 2017). Mechanistically, Sm4 exerts its effects by selectively disrupting SOX18 dimerization, thereby suppressing its transcriptional activity. Importantly, SOX18 genetic depletion or its chemical inhibition by specific inhibitors, Sm4 or the R(+) enantiomer of propranolol (Holm et al., 2025; Overman et al., 2019; Seebauer et al., 2022), dramatically decreased the number of intracellular KSHV genome copies in KLEC indicating that SOX18 contributes to the maintenance of the high viral episome copies in KLECs (Gramolelli et al., 2020). Moreover, Sm4 also significantly decreased the

102 infected spindle cell phenotype (hallmark of KSHV infection) and relative KSHV genome copies *in*
103 *vivo* (Tuohinto et al., 2023), suggesting SOX18 as an attractive therapeutic target for KS.

104 To uncover how SOX18 regulates KSHV episome maintenance, we combined genomics, proteomics,
105 and quantitative molecular imaging in infected lymphatic (LECs) and venous (HUVECs) endothelial
106 cells. Using genome-wide chromatin profiling (ATAC-seq), proximity proteomics (BioID), and high-
107 resolution imaging platforms—including MIEL for epigenetic landscape mapping (Farhy et al., 2019),
108 Number and Brightness (N&B; (Hinde et al., 2016), and single-molecule tracking (Chen et al., 2014;
109 McCann et al., 2021)—we dissected the step wise progression of the early molecular mechanisms
110 that drive viral persistence. This integrative approach reveals a novel interplay between LANA,
111 SOX18, and the chromatin remodeler BRG1 that orchestrates episome persistence and sustains
112 KSHV latency.

113

114 **Results**

115 **SOX18 recruits SWI/SNF chromatin remodeling complex upon KSHV infection**

116 Our recent finding that SOX18 acts as a central hub for controlling viral genome copies during KSHV
117 infection in LECs (Gramolelli et al., 2020) prompted us to investigate the molecular mechanism by
118 which a host TF contributes to the maintenance of high viral genome levels and viral persistence. We
119 first investigated whether SOX18 transactivation activity would be responsible for an increase in
120 genome copies by activating expression of viral genes. To this end, we transduced lentiviruses
121 expressing wild-type (wt) SOX18, two SOX18 mutants: a transactivation deficient, dominant negative
122 mutant (C240X) and a DNA-binding HMG box deletion mutant (HMGdel; Fig S1A), or a Cherry
123 expressing mock control, into HeLa cells inherently lacking SOX18 expression (Fig S1B). These cells
124 were then subsequently infected with rKSHV.219 and analyzed for expression of selected latent
125 (LANA, vCyclin, and vFLIP) and lytic (RTA, K-bZIP, and K8.1) viral genes at 72h.p.i. Intriguingly, no
126 significant effects on transcription of the selected viral genes were seen in KSHV-HeLa cells
127 expressing wt or either of the SOX18 mutants (Fig S1C). To further validate this observation, we
128 measured mRNA levels of the same viral genes in KLECs treated with the SOX18 inhibitor (Sm4) and
129 DMSO, as a control. As shown in (Fig S1D), the SOX18 inhibitor had no significant effects on
130 transcription of the viral genes in KLECs within 24 hours, suggesting that SOX18 does not support
131 high numbers of viral episomes via direct activation of viral gene expression. To further investigate
132 another alternative mode of action, we next opted for an unbiased, proteomics-based approach to
133 uncover SOX18 protein partners in KSHV-infected cells.

134 For this, a proximity-dependent biotinylation screen coupled with mass spectrometry (BioID) was
135 carried out, allowing comprehensive and unbiased identification of proteins in proximity of SOX18. To

136 this end, we transduced a lentivirus expressing BirA*-fusion of SOX18 into KSHV-infected cancer
137 cells (iSLK.219; (Myoung & Ganem, 2011) and uninfected, parental (SLK) cells to differentiate
138 interactions specific for KSHV-infection. The detection of SOX18 as one of the most highly enriched
139 protein in both conditions served as an internal positive control for successful pull-down efficiency
140 (Fig 1A-B). The BioID screen revealed cellular SWI/SNF chromatin remodeling complex (CRC)
141 proteins as high confidence SOX18 interactors in the KSHV-infected cells (Fig 1A), but not in the
142 parental uninfected cell line (Fig 1B-C). Most of the top SOX18 interactors in infected cells are
143 components of the same CRC complex (Fig 1C).

144 SWI/SNF complex, also known as canonical BAF (cBAF), is a multi-subunit entity that confers ATPase
145 activity to alter DNA-nucleosome contacts, thereby generating chromatin accessibility (Centore et al.,
146 2020) (Fig 1D). SWI/SNF complex subunits BRG1 and ARID1A were among the top hits of SOX18
147 protein interaction partners in the infected cells. BRG1 is the catalytic ATPase remodelling the
148 chromatin via nucleosome eviction and needed for efficient replication fork progression, whereas
149 ARID1A serves as a stabilizing core of the complex, directing ATPase activity with high affinity to bind
150 to chromatin and shown to interact with TFs (Cohen et al., 2010; Wanior et al., 2021).

151 To determine if ARID1A or BRG1 are modulated by KSHV infection or SOX18 inhibition in LECs, we
152 confirmed the nuclear localization and protein expression levels in LECs and KLECs (Fig S1E-F).
153 ARID1A levels were almost two-fold higher in KLECs over LECs and further increased with Sm4.
154 Moreover, consistent with our previous findings, SOX18 levels were elevated following KSHV
155 infection (Gramolelli et al., 2020). Next, we analyzed the interactions of SOX18 with BRG1 and
156 ARID1A in LECs and KLECs treated with Sm4 using quantitative proximity ligation assay (PLA) image
157 analysis (Fig 1E). In accordance with the BioID data, significantly higher number of PLA dots of
158 SOX18-BRG1 and SOX18-ARID1A were seen in KLECs over uninfected LECs (Fig 1F-G). Further,
159 uninfected cells treated with Sm4 showed negligible changes in the number of PLA puncta whereas
160 in KLECs these interactions were significantly diminished by SOX18 pharmacological blockade
161 without reducing their total protein levels (Fig 1F-G & Fig S1E-F).

162 As the interaction between SOX18 and SWI/SNF subunits was more pronounced in KLECs (Fig 1A,
163 1F-G), this led us to investigate whether a viral protein mediates these interactions. We recently
164 demonstrated that SOX18 binds near the terminal repeat (TR) region of the KSHV genome (Gramolelli
165 et al., 2020), which is also the binding site for LANA - a key initiator of latent viral DNA replication
166 (Juillard et al., 2016; Schulz et al., 2023). Thus, we tested whether BRG1 or ARID1A also interact
167 with LANA in KLECs. Interestingly, while LANA showed a clear interaction with BRG1 (Fig 1H, I), its
168 interaction with ARID1A (Fig 1H, J) was only moderate in comparison to its interaction with SOX18
169 (Fig S1E, G). Notably, treatment with Sm4 significantly reduced the number of PLA dots, indicating
170 that these interactions are SOX18-dependent. Collectively, these findings suggest that LANA

171 facilitates SOX18 to recruit SWI/SNF primarily via BRG1 in KLECs. The discovery of a SOX18-
172 SWI/SNF axis in KSHV-infected cells suggested a potential role for SOX18 as a virus-engaged
173 pioneer factor. To test if KSHV infection enables SOX18 to function as a pioneer factor, we next set
174 out to address whether SOX18 can influence chromatin organization independently of KSHV.

175

176 **Perturbations to SOX18 activity causes changes in chromatin accessibility**

177 To address this, we used human umbilical vein endothelial cells (HUVECs) as a model system due
178 to the endogenous expression of SOX18. We started by imaging HUVECs with two different
179 techniques: 1) confocal microscopy and 2) stimulated emission depletion (STED). Imaging was
180 performed on HUVECs treated with Sm4 and stained with SiR-DNA, a live-cell nuclear stain that
181 preferentially intercalates into A-T rich regions, increasing fluorescent signal from heterochromatin
182 due to its condensed form which can be seen as an increase in SiR-DNA signal (Fig 2A-B). STED
183 imaging further shows at higher resolution the increased distribution and intensity of the
184 heterochromatin (Fig 2A-C).

185 This observation is corroborated at the cell population level using a high-content, image-based, multi-
186 parametric method known as microscopic imaging of epigenetic landscapes (MIEL; Farhy et al., 2019)
187 (Fig S2A). Although we did not investigate epigenetic marks for these experiments, MIEL analysis is
188 still able to measure differences in chromatin features on DAPI intensity across cell populations. To
189 specifically evaluate if SOX18 dimerization influences chromatin organization, we examined HUVECs
190 with ectopic over-expression of SOX18 to mimic the increase in SOX18 levels upon KSHV infection
191 in LECs (Gramolelli et al., 2020). Similar to previous studies using MIEL analysis (Alvarez-Kuglen et
192 al., 2024; Farhy et al., 2019), raw data was acquired from single cells (nuclei) of similar size and then
193 pooled. The number of nuclei per pool was optimized to identify the minimum sample size yielding
194 the maximal separation accuracy (n = 60 cells/point) (Fig S2B-D). As shown in Fig 2D MIEL analysis
195 revealed significant changes in chromatin compaction upon SOX18 over-expression (oe; orange)
196 whereas the opposite effect is observed after seven days of SOX18 inhibitor treatment (Sm4; blue),
197 when compared to DMSO baseline control conditions (grey). In addition, gain-of-SOX18 function is
198 rescued by its pharmacological inhibition, restoring a chromatin state close to the control conditions
199 (green) (Fig 2D-E & Fig S2E). Importantly, TF-induced condensation is different from accessibility.
200 Here, we suggest that SOX18, with its strong intrinsically disordered region (IDR; Fig S2F), may be
201 driving chromatin into a more phase-separated, condensed state that still allows for transcriptional
202 activity similarly to enhancer hubs or active transcriptional condensates (Boija et al., 2018; Erdos &
203 Dosztanyi, 2024; Sabari et al., 2018).

204 To investigate whether SOX18 influences chromatin accessibility in LECs in the absence of KSHV
205 infection, we performed Assay for Transposase-Accessible Chromatin-sequencing (ATAC-seq) on

206 LECs treated for 24 hours with Sm4. This approach shows that pharmacological disruption of SOX18
207 activity significantly alters global LEC chromatin organization, when compared to DMSO treatment
208 (Fig 2F), with over 10,000 differentially accessible regions (DAR) showing decreased accessibility
209 (Fig 2F) and altered TF binding motifs in these DARs (Fig 2G). Global changes in chromatin
210 accessibility can also be observed as a lower peak intensity in the heatmap showing the top 1000
211 sites with reduced accessibility (Fig S2G). Together, these observations demonstrate that SOX18
212 dimerization helps to maintain an open chromatin state, while its inhibition by Sm4 leads to a
213 significant loss of chromatin accessibility.

214

215 **Chromatin compaction state feedback on SOX18 mobility and oligomeric states**

216 To assess the interplay between different chromatin topological configurations and SOX18
217 biophysical behaviors, we combined two quantitative molecular imaging methods. Number and
218 brightness (N&B; (Digman et al., 2008) analysis provides a map of SOX18 oligomeric states (Fig
219 S3A), while single molecule tracking (SMT; (Chen et al., 2014) measures the mobility and chromatin
220 binding dynamics of labeled molecules in real-time (Fig S3B). To perform these assays in live cells,
221 we induced changes in the chromatin compaction state in HeLa cells using either Actinomycin D
222 (ActD) to induce chromatin condensation, or Trichostatin A (TSA) to promote chromatin opening
223 (Hinde et al., 2015; Hinde et al., 2016), while Halo-tagged SOX18 is ectopically expressed to enable
224 live imaging at single molecule resolution.

225 Previous studies have shown that SOX18 dimer formation modulates an endothelial specific
226 transcriptional signature (Moustaqil et al., 2018). The SOX18 protein dimerizes in a DNA-dependent
227 manner via a cooperative binding mechanism on an inverted-repeat SOX motif spaced by five
228 nucleotides (IR5), suggesting that molecular imaging should reveal at least a SOX18 population
229 containing two states: monomers and dimers. Under baseline conditions (DMSO-treated, Fig 3A, top
230 panels), N&B analysis revealed that SOX18 exists in a mixture of oligomeric states, with monomers
231 being the most abundant, followed by dimers, which are relatively evenly distributed throughout the
232 nucleus followed by the rare formation of higher-order oligomers, indicating that SOX18 can coexist
233 in multiple multimeric states (Fig 3A-D). Induction of chromatin compaction with ActD led to an overall
234 reduction of dimer formation and a higher-order oligomers formation with the whole population pre-
235 dominantly found in a monomeric configuration (Fig 3A, bottom panels & Fig 3B-D). Conversely,
236 chromatin opening with TSA treatment caused a significant increase in the formation of higher-order
237 dimers and oligomers (Fig 3A, middle panels& Fig 3C-D), with monomers being found in between the
238 higher-order collections. These observations are consistent with the fact that SOX18 dimer has low
239 to no diffusion rates and further validate that its ability to self-assemble relies on template availability
240 from the open chromatin (Moustaqil et al., 2018).

241 To further assess the impact of chromatin accessibility on SOX18 behavior, we next measured its
242 chromatin interaction dynamics under varying amounts of chromatin compaction using the SMT
243 method. Here, we performed SMT on TSA treated cells and imaged SOX18 to assess its mobility
244 profile and temporal occupancy (Chen et al., 2014; McCann et al., 2021). In all cells we can detect
245 two populations of molecules based on their diffusion coefficient (Fig 3E). Cells treated with TSA
246 showed a significant reduction in the diffusing population and an increase in the confined fraction
247 compared to DMSO control (Fig 3E-F). These results parallel the N&B findings, which demonstrated
248 an increase in SOX18 oligomerization in open chromatin conditions (TSA treatment; Fig 3A-D). We
249 next questioned whether chromatin accessibility affects the SOX18-chromatin interaction lifetime. To
250 test this, we measured the temporal occupancy of cells treated with TSA. The imaging determined
251 that SOX18 short occupancy time, known as the target search mechanism for binding sites, remained
252 unchanged compared to DMSO treatment (Fig 3G). By contrast, SOX18 long occupancy time,
253 identified as a mechanism directly involved with transcriptional regulation per se, was significantly
254 prolonged (Fig 3H). Additionally, the proportion of molecules that had prolonged interaction was not
255 affected (Fig 3I). These results suggest that increased chromatin accessibility favours more stable
256 SOX18-chromatin interactions involved with transcriptional modulation but not target genes search.

257 Taken together, the findings demonstrate that SOX18 forms higher-order oligomers (N&B) and that
258 there is more SOX18 interacting with chromatin for a prolonged period of time (SMT) when more
259 chromatin is accessible (TSA treated) (Table S1). These results then suggest that higher-order
260 oligomers of SOX18 may have a more stable configuration, leading to increased duration of protein
261 organizations. Studies in the p53 protein have also observed similar trends in high-order oligomers
262 affecting its dissociation kinetics (Rajagopalan et al., 2011). Overall, the N&B and SMT analyzes
263 reveal that SOX18 mobility, chromatin interaction dynamics and oligomeric states are directly
264 dependent on open chromatin accessibility, supporting the notion that its pioneering function may play
265 a role to promote its own activity as a transcriptional regulator.

266 Collectively, findings arising from a combination of genomics, super resolution and cell population-
267 based quantitative imaging demonstrate that SOX18 activity significantly influences chromatin
268 organization at multiple levels, via the modulation of mesoscale architecture and local regulatory
269 regions accessibility.

270

271 **KSHV hijacks SOX18 pioneer activity to increase chromatin accessibility in LECs**

272 The identification of a pioneer function for SOX18 in LECs prompted us to perform an ATAC-seq upon
273 infection to investigate whether this role might be specifically hijacked by KSHV, as *de novo* infection
274 increases SOX18 protein levels in LECs (Gramolelli et al., 2020). Since genomes of viral progeny
275 resulting from spontaneous reactivation by rKSHV.219 in LECs would interfere with ATAC-seq

276 analysis on viral genome, we opted to infect LECs with a strictly latent KSHV-BAC16 strain (ΔORF50;
277 (Weissmann et al., 2025). Infection of LECs with ΔORF50 was first validated to induce the typical
278 SOX18-dependent infection phenotypes as rKSHV.219 (see Materials and Methods & Fig S4) and
279 confirming that the SOX18 upregulation and its critical functions occur during latency.

280 To investigate the link between SOX18-mediated chromatin changes and KSHV infection, we first
281 sought out to delineate the effect KSHV has on chromatin organization by comparing ATAC-seq
282 peaks of uninfected LECs to LECs infected with ΔORF50 (ΔORF50-KLEC). To ensure high quality
283 data, we performed PCA and Pearson's correlation analysis that indicated the robustness of the
284 experimental reproducibility (Fig S5A-B). ATAC-seq analysis revealed that KSHV infection led to
285 significant increases in chromatin accessibility on the host genome (Fig 4A, red), with over 22,000
286 regions becoming more accessible (red) and over 10,000 regions becoming less accessible (blue)
287 when compared to uninfected LECs (Fig 4A, DARs: side panel). This indicates that KSHV infection
288 alters host chromatin towards a more open state.

289 With the understanding that KSHV infection increases chromatin accessibility and SOX18 inhibition
290 reduces chromatin accessibility in uninfected LECs (Fig 2F-G & Fig S2G), we next assessed if the
291 increased chromatin accessibility upon KSHV-infection is SOX18-dependent. To test this, we
292 compared the ATAC-seq peaks upon DMSO and Sm4 treatment in ΔORF50-KLECs. ATAC-seq
293 showed only minor changes on the viral chromatin itself (Fig S5C), further supporting that SOX18
294 does not contribute to high numbers of KSHV episomes in KLECs (Gramolelli et al., 2020) primarily
295 by altering the transcription of viral genes (Fig S1C-D). However, chromatin accessibility of the host
296 genome was significantly reduced when ΔORF50-KLECs were treated with Sm4 for 24 hours (Fig
297 4B), showing that inhibition of SOX18 is able to counter KSHV's ability to induce increased chromatin
298 accessibility. Importantly, the majority (76.7%) of chromatin regions that showed reduced accessibility
299 with Sm4 were the same regions that were originally becoming accessible upon KSHV infection of
300 LECs (Fig 4C, dark blue; shared).

301 We next examined the genomic regions that become more or less accessible due to infection or Sm4
302 treatment. Since we have determined that SOX18 dimerization contributes to chromatin organization,
303 we asked whether SOX18 binding motifs become more accessible upon KSHV infection, which can
304 lead to increased or sustained chromatin accessibility. The ATAC-seq data showed several SOX
305 motifs becoming more accessible in infected LECs compared to the uninfected LECs (Fig 4D, yellow),
306 which could be reversed upon Sm4 treatment (Fig 4E, yellow). We next determined through HOMER
307 analysis that KSHV infection causes an enrichment for *de novo* motifs from bZIP (FRA1) and ETS
308 (ETV2) TF families, in addition to SOX factors, while Sm4 treatment reciprocally showed reduced
309 accessibility in the regions of corresponding TF family motifs (Fig 4F). This is further supported
310 through KSHV-infection of LECs, which shows increased chromatin accessibility in enhancer regions

311 (Fig 4G, red; DMSO), and SOX18 inhibition causing an opposite effect in the infected cells (Fig 4G,
312 blue; Sm4). The enhancer regions also have an enrichment of the SOX18 motif. Here we use the
313 variation in ATAC-seq peak height as a measure of chromatin accessibility to show that Sm4
314 treatment decreases accessibility (Fig 4G, red vs blue). These results further support the notion that
315 SOX18 pioneer function plays a central role to enable KSHV-induced host chromatin accessibility in
316 LECs.

317 We also assessed the chromatin compaction state by looking at HP1α, which is a known marker of
318 heterochromatin formation and integrity (Schoelz & Riddle, 2022) as it can spontaneously phase-
319 separate in solution, forming liquid-like droplets that preferentially sequester heterochromatin
320 components such as nucleosomes and DNA, thereby promoting gene silencing (Bartkova et al., 2011;
321 Larson et al., 2017; Strom et al., 2017). We did this by imaging LECs and KLECs treated with Sm4
322 and measuring HP1α intensity per cell and at the population level through MIEL analysis. Supporting
323 the ATAC-seq findings, mean HP1α intensity was reduced upon KSHV-infection, whereas HP1α-
324 associated heterochromatin foci were widespread and significantly more intense following Sm4
325 treatment both in LECs and KLECs (Fig 4H-I).

326 To assess whether SOX18 influences chromatin organization in LECs and KLECs, we performed
327 MIEL as previously described in HUVECs (Fig 2D–E & S2A–E). In this experiment, we stained the
328 cells with DAPI and an antibody for HP1α, comparing uninfected LECs to KLECs with and without
329 Sm4 treatment (Fig S5D-H). As expected, KLECs (orange) have a distinctly different chromatin
330 organization and HP1α distribution compared to uninfected LECs (grey). Additionally, we also find
331 that the LEC and KLEC populations treated with Sm4 (respectively, blue and green) are more similar
332 to each other than their respective DMSO controls (Fig 4J-L). An interesting observation from this
333 experiment is the point distribution of LECs (grey) and KLECs (orange) that aligns with the Anna
334 Karenina principle (Zaneveld et al., 2017), which posits healthy systems tending to be similar, while
335 each dysfunctional system is abnormal in its own way. This is reflected in the broader distribution of
336 chromatin features in DMSO treated KLECs where KSHV-infection is asynchronous compared to the
337 more compact LEC populations (Fig 4L & Fig S5I). Interestingly, Sm4 treatment leads to a more
338 compact chromatin feature distribution in KLECs, resembling the uninfected LEC state. This indicates
339 that SOX18 inhibition can counteract the chromatin-altering effects of the asynchronous KSHV
340 infection.

341 Taken together, the data demonstrates that KSHV hijacks SOX18 pioneer function and leads to a
342 genome-wide change of host chromatin accessibility. To further investigate whether targeting the
343 virus-induced host genome remodeling is a viable molecular strategy to reduce KSHV genome copies
344 and hallmarks of infection, we next set out to target the SWI/SNF complex using either a
345 pharmacological or a genetic interference approach.

346

347 **SWI/SNF ATPase activity is required for the hallmarks of KSHV infection in LECs**

348 The observation of pharmacological blockade of SOX18 disrupting its interaction with ARID1A and
349 BRG1 (Fig 1E-G) in KLECs prompted us to assess whether disruption of the SWI/SNF complex
350 activity affects KSHV infection efficacy. To this end, we genetically depleted BRG1 and ARID1A by
351 siRNA knockdown in KLECs (Fig 5A). Knockdown of either BRG1 or ARID1A resulted in a clear
352 decrease in cell spindling (Fig 5B) and reduced the relative intracellular KSHV genome copies in
353 KLECs (Fig 5C). Interestingly, depletion of BRG1 had a more pronounced impact on viral genome
354 copy numbers compared to siARID1A, consistent with the stronger observed interaction between
355 LANA and BRG1, than with ARID1A (Fig 1H-I & Fig S1G-H). Although significant, the reduction in
356 KSHV genome copies was not as dramatic as seen with SOX18 inhibition by Sm4 (Fig S4D). This
357 could be due to compensation by the ATPase BRM, also found among the SOX18 interactors by
358 BioID (Fig 1A, C), and previously shown to be able to rescue BRG1 depletion (Hoffman et al., 2014).

359 To avoid possible compensation by BRM, we obtained three specific inhibitors of the SWI/SNF
360 complex. ACBI1 is a PROTAC (proteolysis-targeting chimera) inducing ubiquitylation and
361 proteasomal degradation of the whole ATPase unit (BRG1/BRM), while FHT-1015 is an allosteric
362 inhibitor of the BRG1/BRM ATPase (Battistello et al., 2023; Farnaby et al., 2019). PFI-3 is a selective
363 bromodomain inhibitor for BRG1/BRM but does not detach the SWI/SNF from chromatin nor inhibit
364 its ATPase activity (Singh et al., 2023; Wanior et al., 2021). A CTG cell viability assay using increasing
365 concentrations of the inhibitors in LECs and KLECs showed a clear sensitization of KLECs to the
366 BRG1/BRM ATPase inhibitors ACBI1 and FHT-1015, but not to PFI-3, when compared to uninfected
367 LECs (Fig S6A-C). Degradation of BRG1 with the PROTAC ACBI1 was confirmed by Western blot,
368 while the allosteric inhibitor FHT-1015 led to accumulation of BRG1 in the cells (Fig 5D). Moreover,
369 relatively low concentrations of ACBI1 and FHT-1015 (30 nM and 10 nM, respectively) reduced the
370 spindling phenotype of KLECs that showed reversal to the normal cobblestone EC morphology, while
371 even high concentrations of PFI-3 did not (Fig 5E). Importantly, only inhibitors of the ATPase activity
372 significantly decreased the KSHV genome copy numbers (Fig 5F), without affecting proliferation rates
373 of treated cells (Fig S6D). In accordance with the significant reduction of relative KSHV episomes,
374 LANA protein levels were decreased in cells treated with the ATPase inhibitors for 72 hours.
375 Interestingly, PFI-3 moderately reduced LANA levels without significantly affecting the KSHV episome
376 numbers. As siARID1A having a milder effect on infection than siBRG1 was already observed (Fig
377 5A-C), the inhibitor results further highlight the importance of the BRG1/BRM ATPase activity for
378 KSHV infection over the core subunit ARID1A.

379 Immunofluorescence staining of HP1α in DMSO treated KLECs shows weaker signal when compared
380 to either of the BRG1 ATPase inhibitor treated cells (Fig 5G). HP1α-associated heterochromatin foci

381 were significantly more intense following ACBI1 and FHT-1015 but not PFI-3 treatment (Fig 5H),
382 further supporting BRG1 ATPase activity involvement in SOX18 pioneer function in KLEC. The similar
383 effects on heterochromatin upon Sm4 (Fig 4H-I) and FHT-1015 treatments prompted us to further
384 compare the chromatin landscape following BRG1 or SOX18 blockade in KLECs. To this end, we
385 performed ATAC-seq on KLECs following Sm4 or FHT-1015 inhibitor treatment (Fig S6E-F) and
386 observed a striking overlap (61.5%) between the shared regions showing reduced accessibility upon
387 SOX18 or BRG1 inhibition (Fig S6E, shared loss: dark blue peak).

388 These results demonstrate that KSHV instructs SOX18 to form a complex with the host SWI/SNF
389 CRC and exploit its ATPase activity to alter host chromatin architecture and thereby maintain
390 hallmarks of KSHV infection and high genome copy numbers in KLECs. To validate further the
391 functional effects of SOX18 blockade on viral episomes, we next set out to disturb SOX18 activity.

392

393 **Effective KSHV episome maintenance relies on a functional SOX18**

394 To uncover the molecular mode of action of SOX18 regulating the KSHV episome copies, we next
395 assessed the effect of wtSOX18 and its C240X and HMGdel mutants on relative intracellular KSHV
396 episome numbers. KSHV-HeLa cells transduced with mock (Cherry), wt and mutant SOX18-
397 expressing lentiviruses prior to KSHV infection showed that only cells with wt, but not the mutants,
398 contained a significantly higher relative number of intracellular episomes compared to Cherry control
399 (Fig 6A). Moreover, confocal microscopy revealed that wtSOX18 expressing cells had the highest
400 number of characteristic nuclear LANA speckles, which can be used as a surrogate marker for the
401 viral episome numbers (Adang et al., 2006) (Fig S7A).

402 Our recent study demonstrated that SOX18 binds to DNA sequences within the terminal repeats (TR)
403 of the viral episome (Gramolelli et al., 2020). Since LANA also binds to the TR, we next addressed if
404 SOX18 contributes to LANA binding to the TR. Cherry, wtSOX18, or its mutant expressing KSHV-
405 HeLa cells were subjected to LANA ChIP-PCR using primers for known LANA binding sites (LBS) on
406 the TR. LANA ChIP-qPCR showed that LANA occupancy to TR was significantly increased in cells
407 expressing wtSOX18 when compared to the mutants or the Cherry control (Fig 6B). We then sought
408 to investigate if SOX18, as a secondary effect, would promote latent viral DNA replication directed by
409 LANA from the TR origin of replication. To this end, we subjected the transduced KSHV-HeLa cells
410 to a BrdU-pulldown assay. Only wtSOX18, but neither of the mutants, could significantly increase the
411 newly synthesized, nascent viral DNA when compared to Cherry control (Fig 6C). KSHV, as other
412 DNA viruses, utilize the host cell replication machinery to replicate their latent DNA genome once
413 during the cell cycle. We therefore performed EdU cell proliferation assay and confirmed that the
414 increases in KSHV episomes and DNA synthesis were not simply due to increased proliferation of
415 wtSOX18-expressing cells (Fig S7B). These findings suggest that SOX18 needs both its intact

416 transactivation and DNA binding domains to increase the occupancy of LANA to TR, thereby leading
417 to more efficient latent viral DNA synthesis and increase in viral episome copies.

418 The correlation between SOX18 with increased LANA occupancy to TR prompted us to address if
419 SOX18 itself interacts with LANA in KLECs. Interaction of SOX18 with LANA was confirmed by PLA
420 and abolished by Sm4 treatment (Fig 6D-E). These findings indicate that SOX18 binds not only to the
421 TR (Gramolelli et al., 2020) but also to LANA leading to higher occupancy of LANA on the KSHV
422 origin of latent replication. Since we identified a critical SOX18-SWI/SNF axis on maintaining the high
423 episome numbers, we next assessed the functional role of BRG1 in the LANA-SOX18 complex.
424

425 **BRG1 activity increases LANA occupancy at TRs in a SOX18-dependent manner**

426 Since LANA interacts with both SOX18 (Fig 6D–E) and BRG1 (Fig 1H–I) in KLECs, we first
427 investigated the contribution of BRG1 to the SOX18-dependent increase in the binding of LANA to
428 TR in KLECs as described in (Fig 6B). To confirm specificity, we chose to add two primers for non-
429 LANA binding sites on KSHV genome as well as two additional primers for human genome as
430 negative controls. As shown by ChIP-QPCR in (Fig 6F), both inhibitors reduced the occupancy of
431 LANA to TR within 24 hours but had no significant effects on the negative control sites on viral or host
432 genome (Fig S7C). Immunoblotting confirmed that the reduced LANA binding was not due to lower
433 levels of LANA protein in the inhibitor treated cells (Fig S7D-E), indicating that both inhibitors can
434 specifically reduce LANA binding at TR. We then again performed the BrdU-pulldown assay to
435 investigate the effects of Sm4 and FHT-1015 on nascent viral DNA synthesis, which showed a
436 significantly reduced viral DNA synthesis rate following inhibitor treatments when compared to the
437 DMSO control (Fig 6G). In conclusion, gain of SOX18 in KSHV-HeLa and in KLECs increases LANA
438 occupancy at TR as a primary effect, and consequently leads to higher viral DNA synthesis rate and
439 increased number of intracellular episomes. Both LANA binding to TR and latent viral DNA synthesis
440 can be significantly diminished by chemical blockade of the SOX18-BRG1 axis.

441 Importantly, upon treatment with both inhibitors the number of LANA speckles originating from LANA
442 clustering and formation of higher-order oligomers decreased at TRs, (Hellert et al., 2015) with the
443 signal of LANA pattern appearing less dense (Fig 6H, top and middle panels, Fig 6I). This indicates a
444 more diffusive behaviour of LANA with reduced binding to KSHV episomes. To address whether the
445 SOX18-BRG1 axis would contribute to LANA-mediated KSHV episome tethering onto host chromatin
446 via histone H2A and H2B (Ballestas & Kaye, 2001; Barbera et al., 2006; Verma et al., 2013), we
447 analyzed histone expression upon Sm4 or FHT-1015 treatment of KLEC. IF analysis revealed a
448 significant concurrent reduction in LANA speckles and H2A intensity in inhibitor-treated KLECs (Fig
449 6H-J). Reduction in both H2A and H2B was further confirmed by immunoblotting in Sm4 and FHT-
450 1015 treated KLECs (Fig S7F).

451 These findings reveal that the SOX18–BRG1 axis contributes to the high KSHV episome numbers in
452 KLECs by initially promoting host chromatin reorganization and LANA occupancy to TR, thereby
453 potentially facilitating more efficient LANA-mediated replication and tethering of viral episomes to host
454 chromatin, which ensures persistent and unique infection phenotype in KLECs.

455

456 **Discussion**

457 Beyond transcriptional regulation, TFs are increasingly recognized as key regulators of chromatin
458 organization and condensation state, processes that are essential for homeostasis, differentiation,
459 and cell fate (Shaban et al., 2024). TFs have been classified in three classes: pioneer (control
460 chromatin accessibility), settler (maintain chromatin conformation), and migrant (modulate
461 transcription rates) (Sherwood et al., 2014). Pioneering activity is a unique ability of some TFs to bind
462 directly to condensed chromatin to initiate chromatin remodeling events and increase chromatin
463 accessibility (Bulyk et al., 2023). While direct evidence of viruses specifically hijacking pioneer
464 transcription factors is limited, there are notable examples where viruses interact with host
465 transcription machinery in a manner reminiscent of pioneer factor activity (HBV/HNF4a and HPV/E2)
466 (Neugebauer et al., 2023).

467 Our study reveals how the endotheliotropic, oncogenic KSHV exploits two previously unrecognized
468 aspects of SOX18 biology to promote viral persistence in LECs. First, SOX18 exhibits pioneer
469 transcription factor activity by recruiting the SWI/SNF complex, thereby altering the host chromatin
470 architecture by modulating other TFs' accessibility. Second, through its interaction with the
471 multifunctional, viral protein LANA, SOX18 facilitates the docking and stabilization of viral episomes
472 onto the remodeled host chromatin, acting as a settler-like TF. These newly identified functions of
473 SOX18 underscore its pivotal role in viral infection and provide a mechanistic basis for the virus-
474 induced upregulation of SOX18 at both mRNA and protein levels in infected endothelial cells.

475 A classic example of a TF with pioneer function is SOX2, which maintains the pluripotency of
476 embryonic stem cells through its pioneer activity (Hagey et al., 2022). Despite their disparate roles,
477 previous works have indicated that certain SOX factors, including SOX18, can replace SOX2 during
478 stem cell reprogramming, albeit with a significantly lower efficiency (Nakagawa et al., 2008). The
479 structure of SOX2 HMG domain, needed for pioneer DNA binding, was recently shown to be
480 conserved among several SOX factors, including SOX18 (Dodonova et al., 2020). Previous studies
481 have found SOX18 expression in stromal-derived adipose cells can induce endothelial cell markers,
482 such as PECAM1, VE-Cadherin, KDR, and CD34, or induce hemogenic endothelium derived
483 progenitors towards NK lymphoid pathways, demonstrating SOX18's ability to reprogram cell identity
484 (Fontijn et al., 2014; Jung et al., 2023). Our discovery of SOX18 pioneer function now enforces the
485 capacity of SOX18 to exert pioneering activity and reprogramming, in a context-dependent manner.

486 In pathological conditions, such as cancer or infection, otherwise non-pioneering TFs at physiological
487 levels can gain pioneer activity due to mutation or overexpression (Bulyk et al., 2023). This virus-
488 instructed SOX18 pioneering activity also likely contributes to the KSHV-driven reprogramming of
489 ECs, as reported in our prior studies and those of others (Aguilar et al., 2012; Carroll et al., 2004;
490 Cheng et al., 2011; Gasperini et al., 2012; Hong et al., 2004; Wang et al., 2004). Here we demonstrate
491 that SOX18 does not directly regulate viral gene expression but is redirected by KSHV to remodel the
492 host chromatin architecture. This provides a novel perspective on viral infection, showing that a host
493 transcriptional regulator can be hijacked to perform alternative molecular roles that favor viral DNA
494 replication and genome maintenance. Notably, Epstein Barr virus (EBV), a close gamma herpesvirus
495 family member of KSHV, has also been found to induce reprogramming through chromatin
496 accessibility (Ka-Yue Chow et al., 2022), albeit the molecular mechanisms that drive these changes
497 of the epigenome landscape remain unknown.

498 The identified LANA–SOX18–BRG1 axis promotes a permissive chromatin environment, essential for
499 LANA binding to the TRs on viral episome, efficient latent viral DNA replication and possibly also
500 episome docking to the host genome. Our findings are nicely corroborated by a previous report
501 demonstrating an interaction between BRG1 and TR (Si et al., 2006). The importance of the SWI/SNF
502 complex in KSHV pathobiology is further supported by its previously described role in RTA/ORF50-
503 mediated viral lytic replication (Gwack et al., 2003; Lu et al., 2003). However, this study demonstrates
504 that the interaction of SOX18 with the SWI/SNF complex and the phenotypic changes upon SOX18
505 or BRG1 inhibition in KLECs occur during latency.

506 Our work suggests a new approach to target oncogenic viral infection by demonstrating that targeting
507 host transcriptional modulators that directly engage with KSHV are viable molecular targets. This
508 redefines the current dogma for anti-viral therapies that mostly relies on targeting viral effectors rather
509 than host targets. As critical regulators of gene expression and key drivers of cancer and other
510 diseases, components of the SWI/SNF chromatin remodelling complex have emerged as promising
511 therapeutic targets. Pharmacological inhibition of SWI/SNF, particularly through agents targeting its
512 catalytic subunits or via proteolysis-targeting chimeras (PROTACs), has demonstrated substantial
513 therapeutic potential in extensive preclinical studies across a wide range of cancer types (Battistello
514 et al., 2023; Centore et al., 2020; Farnaby et al., 2019). Importantly, some of these agents have
515 progressed from preclinical research to clinical trials, showing promise of developing effective cancer
516 therapeutics targeting the SWI/SNF complex functions (Dreier et al., 2024; Malone & Roberts, 2024).
517 In our KLEC model, only ATPase inhibitors targeting BRG1 were effective in reducing key hallmarks
518 of infection, whereas inhibition of the BRG1 bromodomain by PFI-3 had no observable effect. This
519 suggests that while PFI-3 may disrupt the recruitment or stabilization of SWI/SNF complex at
520 chromatin, thereby impairing remodeling activity (Lee et al., 2021; Wanior et al., 2021), it may not
521 inhibit the ATPase function of BRG1 once it is already recruited to chromatin by LANA and SOX18.

522 Our previous findings suggested SOX18 as an attractive therapeutic target for KS (Gramolelli et al.,
523 2020; Tuohinto et al., 2023) and that this TF activity is directly modulated as part of R(+) -Propranolol
524 off-target effects (Holm et al., 2025; Overman et al., 2019; Seebauer et al., 2022) in the context of
525 infantile hemangioma. This is further endorsed by a recent study where a 6-month oral propranolol
526 treatment of a patient with classic KS resulted in a substantial decrease in the size of skin KS lesions
527 associated with a reduction in KSHV infection (Salido-Vallejo et al., 2022). We further identify the
528 SOX18–BRG1 axis as a key regulator of viral latency maintenance in LEC with important implications
529 for the development of therapeutic strategies targeting chromatin regulators as a potential molecular
530 approach for managing both KSHV infection and Kaposi Sarcoma.
531

532 **Limitations of the study**

533 One of the limitations of our study is that we do not confirm all the findings in LECs. We used HUVECs
534 and HeLa cells as model systems to investigate how SOX18 navigates the nuclear environment.
535 Specifically, how pharmacological inhibition of SOX18 changes the chromatin organization (HUVECs)
536 and, in turn, how chromatin organization alters SOX18 genome navigation in real-time (HeLa). In
537 venous HUVECs, SOX18 is expressed to differentiate towards lymphatic endothelial lineage, whereas
538 LECs are considered the KS cell of origin and display a unique KSHV infection program with SOX18
539 upregulation. Nevertheless, combining unbiased proteomics screen (BioID), genomics-approach
540 (ATAC-seq), and large-scale chromatin imaging (MIEL), we have discovered SOX18 pioneer function
541 in both ECs independently, in physiological and pathological conditions, and via various approaches
542 that all support SOX18 pioneer function.

543 Another limitation of our current study is that our results only provide circumstantial evidence that
544 SOX18 increases KSHV latent DNA replication and indicate that SOX18 is required to alter the host
545 chromatin for efficient episome stabilization and thereby support higher viral DNA synthesis rates by
546 ensuring higher numbers of template episome genomes. Our aim here was to define the mechanism
547 of how SOX18 promotes high numbers of viral episomes, to pave way for future translational studies
548 where the efficacy of inhibiting chromatin remodelers can be assessed. Therefore, we did not test the
549 efficacy of BRG1 ATPase inhibitors or PROTACs in a preclinical KS model as this was not in the
550 scope of this study.

551 **Acknowledgements**

552 We acknowledge and are extremely grateful to Endrit Elbasani, Silvia Gramolelli, Veijo Nurminen,
553 Lorenza Cutrone, and Riikka Kallinen for their valuable contributions to this study, and Nadezhda
554 Zinovkina for technical assistance. We also acknowledge the technical staff of Biomedicum Imaging
555 Unit (BIU) and Finnish Institute of Molecular Medicine (FIMM) for their help in IFA imaging, and

Proteomics Unit (Institute of Biotechnology, University of Helsinki) in BioID processing and analysis. We thank Norwegian Sequencing Centre, Oslo, Norway, for sequencing services. We kindly thank Riikka Kivelä (University of Jyväskylä and RPU, University of Helsinki, Finland), Bala Chandran (USF, FL, USA), Carolina Arias (Biohub SF, CA, USA) for reagents, and Paul Lieberman (Wistar Institute, PA, USA) for valuable comments.

We also acknowledge the technical and scientific staff of Sydney Microscopy & Microanalysis, the University of Sydney node of Microscopy Australia for their consultation and assistance with the STED, MIEL, and SMT experiments. The authors thank Dr. Rosemary Steinberg for her consultation and advice on statistical analysis and Dr. Kenta Ninomiya for his consultation and advice on MIEL analysis.

Funding

PMO: Sigrid Juselius Foundation, Finnish Cancer Foundation, The Gertrude Biomedical Pty Ltd.

KT: Doctoral program in Biomedicine, University of Helsinki, Finnish Cultural Foundation, Biomedicum Foundation, Magnus Ehrnrooth foundation.

PS: ICANDOC doctoral pilot program.

MF: NHMRC Idea Grants (APP2019904 and APP2029719) and NIH grant 5R01HL096384.

MG: NIH grant 5R01HL096384.

BS: Finnish Cancer Foundation, Sigrid Jusélius Foundation, Jane and Aatos Erkko Foundation, iCAN Digital Precision Cancer Medicine Flagship (320185), Norwegian Cancer Society (274630), South-Eastern Norway Health Authority (2025083) and Norwegian Centre for Molecular Biosciences and Medicine, University of Oslo.

VT: Doctoral program in Integrative Life Sciences, University of Helsinki

SW, TG, AG: Deutsche Forschungsgemeinschaft (DFG) grant GR 3318/5-1 (Research Unit FOR5200 DEEP-DV, project number 443644894).

Author contributions

KT, MG, MF and PMO conceived and designed the experiments with the help of SW, TG, AG, TK and BS. KT, MG, PS, LF, SW, SP and JQ performed the experiments. KT, MG, PS, VT, YW, EH, AT, and MK analyzed the data. QL and JW produced reagents for experiments. KT, MG, MF and PMO wrote the original draft of the manuscript. Manuscript editing and reviewing – PS, VT, SW, AG, BS, KT, MG, MF and PMO.

587 **Declaration of interests**

588 Gertrude Biomedical Pty Ltd. participated in the study design and provided grant support. The authors
589 declare no other competing interests.

590

591 **Materials and methods**

592 **Cell culture**

593 Primary human dermal lymphatic endothelial cells LEC (Promocell; C-12216) were maintained in
594 Microvascular MV-2 (Promocell; C-22121) medium supplemented with 5% fetal bovine serum, basic
595 fibroblast growth factor, insulin-like growth factor 3, epidermal growth factor, gentamicin
596 sulfate/amphotericin, ascorbic acid, and hydrocortisone; VEGF was not added. LECs were used until
597 passage five. HUVEC cells (ATCC) were grown in EGM-2 media supplemented with EGM-2 bullet kit
598 (Lonza; CC-3202).

599 iSLK.219 (Myoung & Ganem, 2011) is an RTA -inducible renal-cell carcinoma SLK cell line, stably
600 infected with a recombinant KSHV.219. HeLa, SLK and iSLK.219 were grown in DMEM (BioNordika;
601 ECB7501L), supplemented with 10% FBS (Gibco; 10270-106), 1% L-glutamate (BioNordika;
602 ECB3000D), and 1% penicillin/ streptomycin (BioNordika; ECB3001D). iSLK.219 cells were also
603 supplied with 10µg/mL puromycin (Sigma; P8833), 600µg/mL hygromycin B (Invitrogen; 687010), and
604 400µg/mL Geneticin G418 (Roche; 04727878001). iSLK.BAC16-ΔORF50 cells were supplemented
605 with 0.5µg/ml puromycin, 200µg/ml hygromycin, and 1000µg/ml G418. Cell lines were used for
606 approximately 15-20 passages.

607 All cells were propagated in a humified incubator at standard conditions. Cells were regularly tested
608 negative for *Mycoplasma* (MycoAlert Mycoplasma Detection Kit, Lonza; LT07-705).

609 *Table 1. Cells used in this study.*

Name	Description	Reference
LEC	Primary cells used in assays	Promocell C-12216
HUVEC	Cell line used in assays	ATCC CRL-4053
HeLa	Cell line used in assays	ATCC CCL-2; RRID:CVCL_0030
iSLK.219	Cell line used in assays rKSHV.219 virus production	Myoung & Ganem, 2011. A kind gift from Arias, C.
SLK	Cell line used in assays	A kind gift from Arias, C.
iSLK.BAC16-ΔORF50	KSHV-ΔORF50 virus production	Weissmann et al. 2025.
HEK293FT	Cherry, wt SOX18 and mutant lentivirus production	Thermo Fisher Scientific, R70007; RRID:CVCL_6911

610

611 **Virus production and infections**

612 Lentivirus production was performed as described in (Gramolelli et al., 2018). The concentrated virus
613 preparation of recombinant KSHV.219 virus was produced from iSLK.219 (Myoung & Ganem, 2011)
614 as described in (Tuohinto et al., 2023) and the virus was precipitated with PEG-it (Systems
615 Biosciences; LV825A-1). Cells infected with rKSHV.219 express green fluorescent protein (GFP) from
616 the constitutively active human elongation factor 1-a (EF-1a) promoter and red fluorescent protein
617 (RFP) under the control of RTA-responsive polyadenylated nuclear (PAN) promoter, expressed only
618 during lytic replication. An ORF50 deletion mutant KSHV-BAC16-ΔORF50 (KSHV-ΔORF50) virus
619 was generated as described in (Weissmann et al., 2025) and produced and concentrated from
620 iSLK.BAC16-ΔORF50 cells similarly as rKSHV.219. Cells infected with KSHV-ΔORF50 express
621 green fluorescent protein (GFP) from the constitutively active human elongation factor 1-a (EF-1a)
622 promoter. The concentrated virus was resuspended in ice-cold PBS, snap-frozen and stored at -80°C.

623 For experimental assays, cells were infected with low titers (MOI 1-2) of rKSHV.219, KSHV-ΔORF50,
624 or transduced with lentiviruses in media with supplements in the presence of 8 µg/mL polybrene
625 (Sigma; H9268) and spinoculation at 450 x g for 30 min, RT with the 5804R centrifuge (Eppendorf).
626 Around 90-100% KSHV infection efficiency was achieved without selection. Virus titers were
627 determined by infecting naïve LECs using serial dilutions of the concentrated virus and assessing the
628 amount of GFP+ and LANA+ cells 72h post-infection with Phenix Opera 20x.

629 **Plasmid constructs**

630 The BirA*SOX18 plasmid construct for BioID was generated from pFuW-myc-BirA-NLS-mCherry (a
631 kind gift by R. Kivelä, University of Helsinki), used as a BirA*Cherry control. The wild-type human
632 SOX18 insert sequence was codon optimized and synthesized by GeneArt (Thermo Fisher) to reduce
633 G-C content, and pFuW-myc-BirA-NLS was inserted to N-terminus of SOX18. The resulting
634 BirA*SOX18 consists of biotin-binding BirA, a nuclear localization signal (NLS), an SOX18 ORF
635 (1152-5bp), including DNA-binding HMG domain (247-462bp), homodimerization domain (463-
636 597bp), and transactivation domain (502-780bp).

637 A pFuW-myc backbone was also used to produce the Cherry, SOX18wt, and mutant plasmids C240X
638 and HMGdel. The C240X and HMGdel mutants are described in (McCann et al., 2021). The codon
639 optimized SOX18wt, C240X, and HMGdel sequences were then cloned in a pFuW-myc plasmid by
640 Gibson Assembly. Both the backbone and gene inserts for SOX18wt, C240X, and HMGdel were
641 assembled using NEB HiFi DNA assembly (NEB; E2611). Sanger Sequencing performed verification
642 of the inserts while restriction analysis was performed to verify the integrity of the backbone.

643 **Inhibitor treatments**

644 Small molecule SOX18 inhibitor Sm4 (Sigma; SML1999 / or a kind gift from Gertrude Biomedical Pty
645 Ltd., Australia) was solubilized in DMSO (Sigma; D8418), stored in -80°C, and mixed with cell media
646 at 20μM for LECs and KLECs and 30μM for HUVECs. ACBI1 (MedChemExpress; 128359) was
647 solubilized in DMSO, stored in -80°C and mixed with cell media at 30nM. FHT-1015
648 (MedChemExpress; 144896) was solubilized in DMSO, stored in -80°C and mixed with cell media at
649 10nM. PFI-3 (Sigma; SML0939) was solubilized in DMSO, stored in -80°C and mixed with cell media
650 at 50μM.

651 **Transfections**

652 Transient transfection of siRNA of a semi-confluent culture of KSHV-infected LEC was done using
653 OptiMEM (Gibco; 31985047), 1.5μl of Lipofectamine RNAiMAX (Invitrogen; 13778075) and 25nM
654 siRNA per well in a 12-well plate according to manufacturer's instructions with MV-2 media. Next day
655 cells were supplied with fresh full MV-2 media. The following siRNAs were used: ON-TARGETplus
656 SMARCA4/BRG1 siRNA (L-010431-00), ARID1A siRNA (L-017263-00) and Nontargeting pool siRNA
657 (D-001810-10) from Dharmacon.

658 Transfection of HeLa cells was completed using a combination of OptiMEM Serum Reduced (Gibco),
659 FuGENE HD Transfection Reagent (Promega), and plasmid DNA constructs for SOX18 wt, mutants
660 or mChery. A mixture of OptiMEM and FuGENE HD (Promega) 4 μL/1000 ng DNA was created to a
661 total volume of 100 μL, after which an appropriate amount of plasmid DNA was added. The mixture
662 was then vortexed at 1000 rpm for a few seconds before being incubated at RT for 20 minutes. Then,
663 the mixture was added to the cells with 900μl of fresh DMEM media per well and incubated at 37°C
664 for total of 72 hours.

665 **BioID coupled with mass spectrometry**

666 Protein-protein interaction screen BioID (Roux et al., 2018) was performed from stably KSHV-infected
667 iSLK.219 and parental uninfected SLK cell line, transduced with BirA*SOX18 or BirA*mCherry
668 construct containing lentiviruses. iSLK.219 was not induced, thus KSHV infection was strictly latent.
669 Following transduction, cells were incubated and expanded for 72h before 80% full cultures were
670 incubated with 50μM biotin (Pierce; B4639) for 24 hours. Cells were washed with PBS before scraping
671 and pelleted before snap-frozen with liquid nitrogen and stored in -80°C. Next, the 1ml pellets were
672 resuspended in 3x volume (3ml) of ice cold BioID lysis buffer (wash buffer (see below) with 0.1%
673 SDS) and 1:3000 benzonase nuclease was added. The samples were vortexed and kept on ice for
674 15 min and sonicated with low output settings 45s on ice for 3 cycles, 5 min on ice in between. After,
675 samples were centrifuged at 16.000g for 15 min at 4°C, and supernatants were transferred to new
676 tubes and spin was repeated. From final supernatant, 50 μl inputs were removed for Western blot to
677 check the expression of transduced plasmids. The supernatant samples were transferred through
678 Bio-Spin chromatography columns (BioRad; 7326008), containing 200μl of Strep-Tactin Sepharose

679 beads (IBA; 2-1201-002, 50% suspension), prewashed 3x 1ml with wash buffer (HENN-buffer with
680 0.5% IGEPAL, 1mM DTT, 1mM PMSF, 1,5mM Na_3VO_4, protease inhibitors; Sigma) for affinity
681 purification. After supernatants were drained under gravity flow, the columns were washed four times
682 with HENN-buffer (50mM HEPES pH 8.0, 5mM EDTA, 150mM NaCl, 50mM NaF, stored at 4°C in the
683 dark). Then, the columns were closed, and biotin-bound proteins were eluted from the beads in the
684 column with 300µl of fresh Biotin-HENN buffer (HENN-buffer with 0.5mM biotin) by incubating 5 min
685 before opening the columns and flow-through was collected, and these steps were repeated. Final
686 elution (600µl) was then frozen in -80°C before further processed and analyzed in Proteomics Unit
687 (Institute of Biotechnology, University of Helsinki). Briefly, reduction of the cysteine bonds with 5mM
688 Tris(2-carboxyethyl) phosphine (TCEP) for 30 mins at 37°C and alkylation with 10mM iodoacetamide
689 was performed. The proteins were then digested to peptides with sequencing grade modified trypsin
690 (Promega, #V5113) at 37°C overnight. After quenching with 10% TFA, the samples were desalted by
691 C18 reversed-phase spin columns according to the manufacturer's instructions (Harvard Apparatus).
692 The eluted peptide sample was dried in vacuum centrifuge and reconstituted to a final volume of 30µl
693 in 0.1% TFA and 1% CH_3CN. BioID was performed with liquid chromatography-mass spectrometry
694 (LC-MS) and analyzed as described in (Liu et al., 2018) by Proteomics Unit (Institute of Biotechnology,
695 University of Helsinki). The high-confidence interacting proteins were identified by first filtering the
696 data using Contaminant Repository for Affinity Purification (CRAPome) and Significance Analysis of
697 INTeractome (SAINT)-express version 3.6.0. Then, only interacting proteins with ≥2 found unique
698 peptides were selected, and finally BirA*SOX18 interacting proteins were bait-normalized to
699 BirA*Cherry interacting proteins using the PSM (peptide spectral match) values.

700 **Cell viability assay**

701 For measuring the viability of cells, CellTiter-Glo (Promega; G7572) luminescent viability assay (CTG)
702 was performed on black 96-well ViewPlates (Revvity; 6005182) for 10 min and the luminescence from
703 live cells were measured with FLUOstar Omega microplate reader (BMG Labtech). The viability %
704 was calculated as an average of luminescent signal from triplicates comparing to DMSO treated cells
705 considered as control with 100% viability.

706 **Cell proliferation assay**

707 To compare the proliferation rates, low number of cells were plated on 96-well ViewPlates (Revvity;
708 6005182) and the next day the cells were treated with 10µM 5-ethynyl-2'-deoxyuridine EdU (Thermo
709 Fisher) for 4 h with LEC/KLEC, and 2 h with HeLa cells, and fixed in 4% PFA in PBS. The proliferating
710 cells were visualized using Click-iT EdU Alexa Fluor 647 (Molecular Probes; C10340) staining
711 according to manufacturer's instructions, and Hoechst 33342. Images were taken using Phenix Opera
712 20x and the portion of EdU-containing nuclei was quantified with Harmony software.

713 **Quantitative RT-qPCR**

714 Total RNA was isolated from cells using the NucleoSpin RNA extraction kit (Macherey-Nagel; 740955)
715 according to manufacturer's protocols. Real time quantitative Polymerase chain reaction (RT-qPCR)
716 and LightCycler480 PCR 384 multiwell plates (4titude FrameStar; 4ti-0382) were used to measure
717 relative mRNA expression of samples. Primer sequences used to amplify the indicated targets are
718 listed in Table 2. Relative abundances of viral mRNA were normalized by the delta threshold cycle
719 method to the abundance of actin.

720 **Quantification of intracellular viral episome copies**

721 Total DNA was isolated from cells using NucleoSpin Tissue Kit (Macherey-Nagel; 74098) and the
722 KSHV genome episome copies were quantified by qPCR using 2XSYBR reaction mix (Fermentas;
723 K0223) and unlabelled primers specific for LANA, K8.1, and genomic actin, listed in Table 2.

724 *Table 2. Oligonucleotides used in this study.*

Target	Forward primer	Reverse primer	Used in
Actin	*TCACCCACACTGTGCCATCTACGA*	*CAGCGGAACCGCTCATTGCCAATGG*	mRNA
LANA	*CGGAGCTAAAGAGTCTGGTG*	*GCAGTCTCCAGAGTCTTCTC*	mRNA
vFLIP	*GCGGGCACAATGAGTTATTT*	*GGCGATAGTGTTGGGAGTGT*	mRNA
vCyclin	*AGCTGCGCCACGAAGCAGTCA*	*CAGGTTCTCCCATCGACGA*	mRNA
ORF50/RTA	*CACAAAAATGGCGCAAGATGA*	*TGGTAGAGTTGGGCCTTCAGTT*	mRNA
K-bZIP	*CCCGGGAACGGACAATTCTGAG*	*CCACTTTGGGAAGGCGCTGTAAG*	mRNA
K8.1	*AAAGCGTCCAGGCCACCACAGA*	*GGCAGAAAATGGCACACGGTTAC*	mRNA, KSHV copies
LANA	*ACTGAACACACGGACAACGG*	*CAGGTTCTCCCATCGACGA*	KSHV copies
G. actin	*AGAAAATCTGGCACCACACC*	*AACGGCAGAAGAGAGAACCA*	KSHV copies
TR-1	*TGTGTGTGAGCCTGTTTG*	*TGTTCACGTAGTGTCCAG*	ChIP LBS
TR-2	*TGCGAGGAGTCTGGGCTGTC*	*CGTAGCAAGCACTGAGGAGGC*	ChIP LBS
ORF73	*AAGTCCGTATGGGTCATTGC*	*GGATGGAAGACGAGATCCAA*	ChIP control
ORF75	*AGCGAGCACCGTCTGTATTT*	*GCACCGGCGGCTACTATCTG*	ChIP control
hsZNF268	*AATGCATTTCCACACTGCAA*	*AAAGAGGTTGCTGCCAAGAC*	ChIP control
hsZNF544	*GCCCTATGAGTGCAACCTGT*	*CTCCAGTGTGAATTCGCTGA*	ChIP control

725

726 **Immunoblotting**

727 Cell lysis, SDS-PGE and immunoblot were performed as described in (Gramolelli et al., 2018). The
728 following primary antibodies were used for KSHV: rat monoclonal anti-HHV-8 LANA (Abcam; LN-35;
729 ab4103); rabbit polyclonal RTA/ORF50 (a kind gift from C. Arias, University of CA), mouse monoclonal
730 anti-K-bZIP and K8.1 (Santa Cruz; sc-69797, sc-65446) and for human: mouse monoclonal anti-β
731 actin (Santa Cruz; sc-8432); mouse monoclonal anti-Vinculin (Santa Cruz; sc-73614); mouse
732 monoclonal anti-SOX18 (Santa Cruz; sc-166025); rabbit monoclonal anti-ARID1A and anti-BRG1
733 (Abcam; ab182560, EPR13501 and ab110641, EPNCIR111A); anti-H2A (Cell Signaling; D6O3A,
734 12349S) or anti-H2B (Cell Signaling; D2H6, 12364S) and mouse monoclonal anti-HP1α (Santa Cruz;

735 sc-515341). Following secondary antibodies were used: anti-mouse, anti-rabbit and anti-rat IgG HRP
736 conjugated (Cell Signaling; 7076, 7074, 7077).

737 **Proximity ligation assay (PLA)**

738 Proximity ligation assay (PLA) was performed using Duolink PLA technology (Sigma-Aldrich). LECs
739 and KLECs were plated on a PhenoPlate (Revvity; 6055300) and infected with rKSHV.219. Cells were
740 fixed with 4% PFA then permeabilized with Triton X-100 (Sigma; T9284) and 1µg/mL of Hoechst
741 33342 (Fluka Biochemicka) in PBS. Blocking with Duolink Blocking Solution in a 37ºC humidity
742 chamber for 60 minutes and then stained with antibodies against rabbit polyclonal anti-LANA (a kind
743 gift from B. Chandran lab), mouse monoclonal anti-SOX18 (Santa Cruz; sc-166025), anti-BRG1 (sc-
744 17796), or anti-ARID1A (sc-32761) or either normal mouse IgG or normal rabbit IgG (sc-2025;
745 sc2027). Wells were washed five times with 1x wash buffer A and then treated with PLA probe solution
746 composed of anti-mouse PLUS (DUO92001) and anti-rabbit MINUS (DUO92005) probes diluted in
747 Duolink antibody diluent and incubated in a 37ºC humidity chamber for 60 minutes. Probes were
748 detected with *in situ* far-red detection reagent (DUO92013). Ligation was performed by treating cells
749 with 1:40 dilution of Ligase in 1x Ligation Buffer and incubating and 37ºC humidity chamber for 30
750 minutes. Wells were washed five times with 1x wash buffer A and Amplification was performed by
751 treating cells with 1:80 dilution of Ligase in 1x ligation buffer and incubating and 37ºC humidity
752 chamber for 100 minutes. Wells were washed five times with 1x wash buffer B and a 0.01x wash
753 buffer B was added. Imaging of interaction PLA dot signals were accomplished using Opera Phenix
754 (PerkinElmer) and quantified using Harmony software.

755 **Chromatin immunoprecipitation (ChIP)**

756 HeLa cells transfected with Cherry, SOX18, C240X, or HMGdel cDNAs, or LECs were infected with
757 rKSHV.219. After 72 hours, the infection efficiency was confirmed by GFP signal. For KLEC, cells
758 were treated with inhibitors or DMSO control and incubated for another 24 hours. For each ChIP, one
759 or three 10-cm dish for HeLa and KLEC, respectively, was cross-linked and protocol according to
760 SimpleChIP Enzymatic Chromatin IP Kit (Cell Signaling; 9003S) was used. Antibodies against rat
761 monoclonal anti-HHV-8 LANA (Abcam; LN-35, ab4103) and IgG control (Cell Signaling; 9003S) and
762 were used, also listed in Table 3. Chromatin was eluted and de-crosslinked and DNA was purified
763 using a DNA Clean & Concentrator kit (Zymo Research; D5205). The experiments were done at least
764 two independent times. The purified DNA was amplified with RT-qPCR with two set of TR primers
765 (mean) on known LBS (LANA-binding sites), and primers for non-LBS on KSHV genome as well as
766 two additional primers for human genome as negative controls listed in Table 2, and differences in
767 samples is shown as % of input as individual values for each biological replicate.

768 **Bromodeoxyuridine (BrdU) incorporation assay**

769 HeLa cells transfected with Cherry, SOX18, C240X, or HMGdel cDNAs, or LECs were infected with
770 rKSHV.219. After 72 hours, the infection efficiency was confirmed by GFP signal. For KLEC, cells
771 were treated and incubated for another 72 hours. Cell culture media with 100μM of BrdU (Sigma; B-
772 5002) was added and incubated for 2 hours for HeLa and 4 hours for KLECs before cell samples were
773 trypsinized and collected. The samples were centrifuged for 5 minutes at 1500 rpm to collect a cell
774 pellet. The cell pellet was then used for DNA extraction using the Nucleospin Tissue kit (Macherey-
775 Nagel; 740952.250) with T1 lysis buffer and Proteinase K. DNA samples were eluted and sonicated
776 for 3 cycles for 30 seconds, with the samples cooling on ice between each cycle. For BrdU pulldown,
777 DNA was first denatured at 95ºC for 10 minutes and cooled on ice. For input samples, 10% of each
778 sample was aliquoted and stored. Following, 4μL of mouse monoclonal BrdU antibody (BD
779 Biosciences; 555627) or normal mouse IgG (Santa Cruz; sc-2025) was added to the remaining
780 samples and incubated overnight at 4ºC while rotating. Additionally, a total of 130μL of DynabeadsTM
781 Protein G magnetic beads (Invitrogen; 10003D) were washed twice with 1mL IP wash buffer (50mM
782 HEPES-NaOH pH 7.55, 250mM LiCl, 1mM EDTA, 1% NP-40, 0.7% sodium deoxycholate) and once
783 with IP buffer (10mM HEPES-NaOH pH 7.9, 100mM NaCl, 1mM EDTA, 0.5 mM EGTA, 0.1% sodium
784 deoxycholate) with the magnetic rack (Bio-Rad). The beads were then blocked with 1mg/mL of BSA
785 and 0.25mg/mL of Salmon sperm DNA (Fisher; 10605543) overnight at 4ºC, rotating. The next day,
786 the blocking buffer in the magnetic beads were removed using the magnetic rack and washed once
787 with IP buffer. Then, 130μL of IP buffer were mixed by pipetting and 15μL of the beads were added
788 to each sample and mixed. The samples were then incubated for 3 hours at RT, rotating. Following,
789 the beads in the samples were washed 5 times with IP wash buffer using 1mL for each sample. The
790 samples were then eluted in 200μL of elution buffer (50mM Tris-HCl pH 8, 10mM EDTA, 1% SDS) at
791 65ºC for 1 hour. Following elution, the samples were added to the magnetic stand and the supernatant
792 was transferred to new, clean tubes. The samples and inputs were then purified with the ChIP DNA
793 Clean and Concentrator kit (Zymo Research; D5205). A total of 40μL of elution buffer was used for
794 the final DNA product for a subsequent RT-qPCR run conducted using primers for KSHV and the
795 human housekeeping genes of interest listed in Table 2 and the differences in samples are shown as
796 % of BrdU incorporation normalized to human BrdU.

797 **Antibodies**

798 Primary antibodies used in Western Blotting (WB), immunofluorescence staining (IF), Proximity
799 Ligation Assay (PLA), chromatin immunoprecipitation (ChIP), and bromodeoxyuridine
800 immunoprecipitation (BrdU-IP) assays of this study are listed in Table 3.

801 *Table 3. Antibodies used in this study.*

Antibody stain	Species	Source/reference	Dilution	Used in
BrdU	Mouse monoclonal	BD Biosciences, 555627	1:60	BrdU-IP
LANA	Rat monoclonal	Abcam, ab4103	1:1000	IF

			1:500	WB
LANA	Rabbit	A kind gift from B. Chandran University of	1:1000	PLA
ORF50/RTA	Rabbit polyclonal	A kind gift from C. Arias, University of CA	1:1000	WB
K-bZIP	Mouse monoclonal	Santa Cruz, sc-69797	1:1000	WB
K8.1	Mouse monoclonal	Santa Cruz, sc-65446	1:1000	WB
β-actin	Mouse monoclonal	Santa Cruz, sc-47778	1:1000	WB
Vinculin	Mouse monoclonal	Santa Cruz, sc-73614	1:1000	WB
Mouse IgG	Mouse	Santa Cruz, sc-2025	1:250 1:1000	BrdU-IP PLA
Rabbit IgG	Rabbit	Cell Signaling 2729S	1:1000	PLA
BrdU	Mouse monoclonal	BD Biosciences, 555627	1:60	BrdU-IP
SOX18	Mouse monoclonal	Santa Cruz, sc-166025	1:1000	IF, WB, PLA
ARID1A	Rabbit monoclonal	Abcam, ab182560	1:500	IF, WB, PLA
ARID1A	Mouse monoclonal	Santa Cruz, sc-32761	1:1000	PLA
BRG1	Rabbit monoclonal	Abcam, ab110641	1:500	IF, WB, PLA
BRG1	Mouse monoclonal	Santa Cruz, sc-17796	1:1000	PLA
HP1α	Mouse monoclonal	Santa Cruz, sc-515341	1:1000	IF
H2A	Rabbit monoclonal	Cell Signaling, 12349S	1:1000	IF, WB
H2B	Rabbit monoclonal	Cell Signaling, 12364S	1:1000	WB

Image acquisition for LECs

Immunofluorescence

Cells were plated on a 96-well PhenoPlate (Revvity; 6055300) and infected with rKSHV.219 and treated or cells were seeded on fibronectin (from human plasma, Sigma; F0895) -coated glass coverslips on 24-well plate, and treated. Cells were fixed with 4% PFA, permeabilized with Triton X-100 (Sigma; T9284) and stained for KSHV proteins with antibody against rat monoclonal anti-HHV-8 LANA (Abcam; LN-35; ab4103) and for human proteins with antibodies against mouse monoclonal anti-SOX18 (Santa Cruz; sc-166025), rabbit monoclonal anti-BRG1 (Abcam; EPNCIR111A) or anti-ARID1A (EPR13501), anti-H2A (Cell Signaling; D6O3A, 12349S) or mouse monoclonal anti-HP1α (Santa Cruz; sc-515341). Alexa Fluor anti-rat 647 or anti-mouse 596 (Invitrogen; A48272, A21203) were used as secondary antibodies. Nuclei were visualized with Hoechst 33342 (Sigma; 14533).

High-throughput imaging

From 96-well plates, images were taken using an automated cell imaging system ImageXpress Pico (Molecular Devices) with 10x objective or Opera Phenix (PerkinElmer) with either 20x or 40x objectives with z-stack of 5 images. Cells were quantified using pipeline created in Harmony. Briefly, LANA speckles were quantified as mean number of nuclear objects from 10 fields (n > 200 nuclei) for each biological replicate (n = 3) shown as individual values ±SD. Signal from PLA dots were quantified as mean number of nuclear objects from 10 fields (n = 100 nuclei) combined from (n=3) biological replicates shown as violin plots with median and quantiles.

822 ***Confocal***

823 Coverslip images were taken with LSM880 (Zeiss) PMT confocal with Plan-Apochromat 63x oil
824 objective with 405, 561 and 633nm lasers. Cells were quantified using macro pipeline created in Fiji-
825 imageJ. Briefly, maximum image projections (MIP) were created from z-stack of 15 images for each
826 channel. Signal intensity thresholds were acquired for 16-bit depth MIP images with default settings,
827 and particles (nuclei) were analyzed for mean arbitrary unit (a.u.) intensity within each nucleus (n =
828 100 or 200) shown as individual values ±SD. LANA speckles were quantified as mean number of
829 nuclear objects in each nucleus (n = 100) shown as violin plots with median and quantiles.

830 **Image acquisition for HUVEC**

831 ***Confocal***

832 HUVEC cells were seeded on 0.5% gelatin coated 8-well microscope slide (Ibidi; 80827) at a density
833 of 50,000 cells/well in EBM-2 media overnight. HUVEC cells were then treated overnight with either
834 DMSO or Sm4 (30μM). The next day cells were stained with SiR-DNA (Spirochrome) at a 1:2000
835 dilution for 1 hour prior to imaging. Cells were imaged on a Leica TCS SP8 (Leica Microsystems
836 GmbH) microscope at 37°C and 5% CO_2 using a 93x 1.30NA glycerol immersion objective and a
837 tunable white light laser unit.

838 ***STED***

839 Live cell STED gated imaging was performed on a Leica TCS SP8 microscope (Leica Microsystems),
840 using a 93x 1.30 NA glycerol immersion motCORR STED White objective and a tunable white light
841 laser unit. Spy650-DNA labelled nuclei were imaged with a 647nm excitation running at ~5% power,
842 and with emission wavelengths set between 660 and 750nm. Fluorescence depletion used a 775nm
843 laser running at 50% output power. Pinhole was set at 129.5μm. Emitted fluorescence intensity was
844 filtered by a notch filter (775nm). Images (1024 by 1024 pixels) were collected with a pixel size range
845 of ~ 25nm – 30nm (Zoom range between 4 to 5) and with a Z-stack step size of 0.15μm (typical range
846 of 0.3 – 0.5μm). A line average of 3 with no frame accumulation was used. All scans were performed
847 at a scan speed of 400 Hz. Deconvolution of images was performed with Huygens Professional
848 software (Scientific Volume Imaging). Average intensity of the samples was analyzed on cell profiler
849 and the line profiles were determined using ImageJ.

850 **Microscopic imaging of epigenetic landscape MIEL**

851 ***Preparation***

852 HUVEC cells were seeded at a density of 50,000 cells/well in an 8-well chamber slide (Ibidi; 80827).
853 Cells were then treated with either DMSO or Sm4 overnight. LECs were seeded at a density of
854 100,000 cells/well in a 12-well plate and the next day either left uninfected or infected with rKSHV.219.
855 The next day cells were moved to fibronectin (from human plasma, Sigma; F0895) coated glass
856 coverslips on 24-well plate. After 72 hours post infection, cells were then treated with either DMSO or
857 Sm4 for 24 hours.

858 The following day both ECs were fixed with 4% PFA for 10 mins at room temperature, then washed
859 with PBS. Cells were then permeabilized with 0.3% Triton X-100/PBS for 5 minutes, followed by
860 washing with PBS and blocking with 0.5% BSA/PBS for 1 hour. Cells were then stained with 5 ug/ml
861 of DAPI for 3 minutes and then washed with PBS. LECs and KLECs were additionally stained with
862 mouse monoclonal anti-HP1α (Santa Cruz; sc-515341) overnight, washed with PBS and Alexa Fluor
863 anti-mouse 596 (Invitrogen; A21203) was used as secondary antibody. Coverslips were washed with
864 PBS and dH2O before mounting to microscope slides.

865 ***Confocal acquisition***

866 HUVEC cells were acquired on a Nikon A1R confocal microscope using the 20x 0.75 NA air objective
867 and LECs/KLECs were acquired on a Zeiss LSM880 confocal microscope using the 63x oil objective.

868 ***Data Processing***

869 Image features for each cell were extracted using the MIEL pipeline (Farhy et al., 2019). Feature
870 values were normalized using z-score transformation. For each experimental condition, individual cell
871 profiles were condensed into an averaged center representing the population-level feature vector.
872 The number of cells used to compute each averaged center was determined through bootstrap
873 analysis, as described in Bootstrap analysis. The condensed centers were then subjected to principal
874 component analysis (PCA), using four principal components, to construct a reduced-dimensional
875 representation of cellular behavior.

876 ***Distance Matrix***

877 To assess phenotypic similarity between conditions, the Euclidean distance between all pairwise
878 centers was calculated. To evaluate within-condition variability, the average distance between all
879 centers belonging to the same experimental condition was computed, providing a measure of
880 dispersion in cellular behavior across replicates.

881 ***Confusion Matrix***

882 Support Vector Machine (SVM) classification was performed using Python's scikit-learn library
883 (version 1.2.2) to evaluate the separability of the condensed centers. Eighty percent of the data from
884 each condition were used as a training set, while the remaining 20% served as the test set.
885 Classification accuracy was assessed on the test set, and results were summarized in a confusion
886 matrix to visualize performance across conditions.

887 ***Bootstrap Analysis***

888 To determine the optimal number of cells required to generate a representative averaged center, we
889 conducted a bootstrap-based optimization. First, PCA was performed using all available cells from all
890 conditions. From this analysis, we selected conditions that exhibited clear separation in the PCA
891 space. Using these separable conditions, 1,000 bootstrap iterations were performed. In each iteration,
892 80% of the total cell count per condition was randomly sampled with replacement. These subsampled

893 datasets were condensed into centers, and PCA followed by SVM classification was applied.
894 Classification accuracy was recorded for each iteration. The optimal condensation number was
895 defined as the smallest number of cells that achieved ≥95% classification accuracy in ≥95% of the
896 bootstrap iterations. This ensured robust and reproducible discrimination of experimental conditions
897 while minimizing cell input requirements.

898 **Quantitative Molecular Imaging**

899 ***Single molecule tracking (SMT)***

900 ***Preparation***

901 SMT was performed as described in (McCann et al., 2021). In summary, HeLa cells were seeded at
902 a density of 23,000 cells/well in 8-well chamber glass slides (Ibidi; 80827) coated with 0.5% gelatine
903 24h prior to transfection. 300ng of plasmid DNA/well of either Halo-tagged SOX18 was transiently
904 transfected into the cells using X-tremeGENE 9 Transfection Reagent kit (Roche; XTG9RO). Cells
905 were then incubated at 37°C with 5% CO_2 overnight prior to imaging then washed three times. Culture
906 media was replaced with imaging media (FluoroBrite DMEM, Gibco; A1896701), 10% FBS, 1%
907 HEPES, 1% GlutaMax along with 400nM of Trichostatin A for four hours prior to imaging. 45 minutes
908 before imaging 1nM of JF549 Halo-tag ligand (Promega; GA1111) was added directly to the media
909 and cells were incubated for 10 minutes at 37 ° C with 5% of CO_2. Following incubation, cells were
910 washed twice 15 minutes apart and replaced with imaging media.

911 ***SMT acquisition***

912 Images were acquired on a Nikon TIRF microscope at a TIRF angle of 61 degrees to achieve HILO
913 illumination. Samples were recorded with an iXon Ultra 888 EMCCD camera, filter cube TRF49909 –
914 ET – 561 laser bandpass filter and 100 X oil 1.49 NA TIRF objective. Cells were imaged using a
915 561nm excitation laser at a power density of 10.3μW to perform two different acquisition techniques.
916 A fast frame rate which uses a 50 Hz (20ms acquisition speed) to acquire 6000 frames without
917 intervals to measure displacement distribution and fraction bound, and a slow frame rate which uses
918 a 2 Hz (500ms acquisition speed) to acquire 500 frames without intervals to measure residence
919 times.

920 ***SMT analysis***

921 Masking and segmentation of the nucleus was performed in ImageJ for all files. To identify and track
922 molecules a custom-written MATLAB implementation of the multiple target tracing (MTT) algorithm,
923 known as SLIMfast was used (Serge et al., 2008). Parameters used for fast frame rate analysis:
924 Localization error: $10^{-6.5}$, blinking (frames) = 1, max # of competitors: 3, max expected diffusion
925 coefficient = 3μm^2/sec, box size = 7, timepoints = 7, clip factor = 4. Cells with less than 500 trajectories
926 based on the above parameters were excluded from analysis. The first four frames of each trajectory
927 were used to calculate the mean squared displacement. Diffusion coefficient was calculated from

928 each trajectory's mean squared displacement and plotted. An inflection point was determined on
929 SOX18 diffusion profile and used as a boundary to determine confined vs non-confined states for all
930 conditions. The confined fraction and non-confined fraction of each cell were calculated by computing
931 the number of trajectories whose mean diffusion coefficient were defined as confined and non-
932 confined respectively. Parameters used for slow frame rate analysis: Localization error: 10^{-7}, blinking
933 (frames): 1, max # of competitors: 3, max expected diffusion coefficient = 0.33μm^2/sec, box size = 9.
934 Slow-tracking analysis was performed using custom MATLAB code based on (Chen et al., 2014).

935 **Fluorescence fluctuation spectroscopy (FFS)**

936 ***Halo Tag labelling for FFS experiment***

937 To saturate all Halo Tags with Janelia Farm dyes 549 or 646 for single or dual-color labelling, HeLa
938 cells transiently expressing Halo Tag-tagged Sox7 and SOX18 constructs were incubated with a
939 saturating concentration of a single JF dye (JF549, 100nM) or two JF dyes (JF549 : JF646, 100nM :
940 100nM) for 15 minutes at 37°C, similar to (McCann et al., 2021). Cells were washed twice with 1×
941 PBS before imaging experiments.

942 ***FFS acquisition***

943 All FFS measurements for Number and Brightness (NB) analysis and cross Raster Image Correlation
944 Spectroscopy (RICS) were performed on an Olympus FV3000 laser scanning microscope coupled to
945 an ISS A320 Fast FLIM box for fluorescence fluctuation data acquisition. For single channel NB FFS
946 measurements, HaloJF549 tagged plasmids were excited by a solid-state laser diode operating at
947 561 nm and the resulting fluorescence signal was directed through a 405/488/561 dichroic mirror to
948 an external photomultiplier detector (H7422P-40 of Hamamatsu) fitted with a mCherry 600-640 nm
949 bandwidth filter. For dual channel RICS FFS measurements (that enable cross RICS), the HaloJF546
950 and HaloJF646 combination were excited by solid-state laser diodes operating at 561 nm and 640
951 nm, respectively, and the resulting signal was directed through a 405/488/561/640 dichroic mirror to
952 two internal GaAsP photomultiplier detectors set to collect 600-640 nm and 650-750 nm, respectively.

953 All FFS data acquisitions (i.e., NB, cross RICS) employed a 60X water immersion objective (1.2 NA)
954 and first involved selecting a 10.6 μm region of interest (ROI) within a HeLa cell nucleus at 37°C in
955 5% CO2 that exhibited low protein expression level (nanomolar) to ensure observation of fluctuations
956 in fluorescence intensity. Then a single or simultaneous two channel frame scan acquisition was
957 acquired (N = 100 frames) in the selected ROI with a pixel frame size of 256 x 256 (i.e., pixel size ~
958 41nm) and a pixel dwell time of 12.5 μs. These conditions resulted in scanning pattern that was found
959 to be optimal for simultaneous capture of the apparent brightness and mobility of the Halo tagged
960 constructs being characterised by NB and cross RICS analysis; all of which was performed in the
961 SimFCS software developed at the Laboratory for Fluorescence Dynamics (LFD).

962 ***Number and brightness (NB) analysis***

963 The oligomeric state of the different HaloJF549-tagged plasmids investigated was extracted and
964 spatially mapped throughout single channel FFS measurements via a moment-based brightness
965 analysis that has been described in previously published papers [79,80]. In brief, within each pixel of an
966 NB FFS measurement there is an intensity fluctuation $\mathrm{F(t)}$ which has: (1) an average intensity $\langle \mathrm{F(t)} \rangle$
967 (first moment) and (2) variance σ^2 (second moment); and the ratio of these two properties describes
968 the apparent brightness (B) of the molecules that give rise to the intensity fluctuation. The true
969 molecular brightness (ε) of the fluorescent molecules being measured is related to B by $\mathrm{B} = \varepsilon + 1$,
970 where 1 is the brightness contribution of a photon counting detector. Thus, if we measure the B of
971 monomeric HaloJF549-Sox7 ($B_{monomer} = \varepsilon_{monomer} + 1$) under our NB FFS measurement conditions, then
972 we can determine $\varepsilon_{monomer}$ and extrapolate the expected B of HaloJF549-tagged dimers ($B_{dimer} = (2 \times$
973 $\varepsilon_{monomer}) + 1$) or oligomers (e.g., $B_{tetramer} = (4 \times \varepsilon_{monomer}) + 1$), and in turn define brightness cursors, to
974 extract and spatially map the fraction of pixels within a NB FFS measurement that contain these
975 different species. These cursors were used to extract the fraction of HaloJF549-SOX18 dimer and
976 oligomer (i.e., number of pixels assigned B_{dimer} or $B_{oligomer}$) within a NB FFS measurement and quantify
977 the degree of SOX18 self-association across multiple cells. Artefact due to cell movement or
978 photobleaching were subtracted from acquired intensity fluctuations via use of a moving average
979 algorithm and all brightness analysis was carried out in SimFCS from the Laboratory for Fluorescence
980 Dynamics.

981 **Assay for Transposase-Accessible Chromatin -sequencing (ATAC-seq)**

982 ***Cell preparation and infection comparison of KSHV strains***

983 LECs infected with rKSHV.219 display a unique infection program with spontaneous lytic reactivation
984 initiated by viral ORF50/RTA, leading to production of viral progeny (Choi et al., 2020; Gramolelli et
985 al., 2020). These viral particles contain nascent DNA that, upon lysis of the host cell, releases cell
986 free viral DNA that interferes with the ATAC-seq analysis resulting in high background signal. To avoid
987 this, we opted to infect LECs with a KSHV-BAC16-ΔORF50 strain that has ORF50/RTA stop-codon
988 prohibiting spontaneous lytic reactivation, and production of new viral particles (Weissmann et al.,
989 2025). Notably, although KSHV-ΔORF50 is an optimal viral strain for ATAC-seq, most of the infection
990 assays in this study are carried out using rKSHV.219 strain as it better recapitulates the natural
991 infection of KSHV in LECs.

992 Infection by ΔORF50 was first validated to induce similarly high levels of intranuclear episome copies
993 and hallmarks of KSHV infection in LECs as wt rKSHV.219 (Fig S4A-F). Importantly, the SOX18
994 upregulation is also evident in ΔORF50-KLECs (Fig S4A). CTG viability assay using increasing
995 concentrations of Sm4 to compare the viability of LECs infected with both strains show that infection
996 sensitizes LECs to Sm4 and that 20μM Sm4 is optimal for all SOX18 inhibition analyzes in LECs,
997 including ATAC-seq (Fig S4B). Infections in LECs resulted in identical spindling phenotypes, a
998 hallmark of KSHV-infected LECs, which were similarly reduced upon SOX18 blockade by Sm4 (Fig

999 S4C). Next, we checked the relative intracellular KSHV episome numbers by qPCR, which were
1000 reduced by Sm4 to the same extent (Fig S4D). LANA protein tethers KSHV episomes to host
1001 chromatin and its characteristic dotty IF staining pattern (LANA speckles) can therefore serve as a
1002 surrogate marker for intranuclear viral episomes (Adang et al., 2006). LECs infected with either viral
1003 strain showed comparable levels of nuclear LANA speckles (Fig S4E, left panels) confirming that
1004 infections yield similar levels of intranuclear episome copies in LECs. The amount of LANA speckles
1005 was similarly reduced by Sm4 in LECs (Fig S4E-F).

1006 ***Library preparation for sequencing***

1007 ATAC-seq libraries for uninfected LEC and ΔORF50-KLEC treated for 24h with DMSO or Sm4 were
1008 prepared in B. Sahu lab as previously described in (Buenrostro et al., 2015; Corces et al., 2017).
1009 Briefly, 50,000 cryopreserved cells were washed with ice-cold PBS and resuspended in 50µl of ATAC-
1010 seq lysis buffer and incubated for 3 min on ice. Nuclei were centrifuged at 500 x g for 10 min at 4°C,
1011 followed by transposition with Tn5 transposase (Illumina; 20034197). Tagmentation was carried out
1012 on a thermomixer at 37°C for 30 min at 1,000 rpm. The reaction was purified using MinElute PCR
1013 Purification Kit (Qiagen; 28004) and eluted in nuclease-free water. The samples were amplified for a
1014 total of 8 cycles and purified with AMPure beads (Agencourt; A63881). Libraries were paired end
1015 sequenced on Illumina Novaseq 6000.

1016 ATAC-seq for ΔORF50-KLEC treated for 72h with DMSO, Sm4 or FHT-1015, was performed in A.
1017 Grunhoff lab using the Omni-ATAC-seq protocol (Corces et al., 2017). Briefly, 50,000 cryopreserved
1018 cells were thawed, treated with DNase I (200U/ml, Worthington) at 4°C for 5 min and DNAse was
1019 inactivated by addition of EDTA (1.5mM final). Cells were washed with cold wash buffer (PBS + 0.04
1020 % BSA) twice and $1x10^5$ cells were resuspended in 1ml cold RSB buffer (10mM Tris-HCl pH 7.4,
1021 10mM NaCl, 3mM $MgCl_2$). Cells were pelleted again at 500 x g for 5 min and resuspended in 50µl of
1022 cold ATAC-NTD lysis buffer (RSB Buffer + 0.1% NP40, 0.1% Tween20, 0.01% Digitonin). Lysed cells
1023 were diluted in 1ml cold ATAC-T buffer (RSB + 0.1% Tween20) and inverted three times. The resulting
1024 nuclei were pelleted at 500 x g for 10 minutes and the supernatant was removed. Cell pellets were
1025 transposed with 50µl of transposition mix containing 25µl 2xTD Buffer (20mM 1M Tris-HCl pH 7.6,
1026 10mM $MgCl_2$, 20% Dimethyl Formamide) 2.5µl transposase (custom made, 100nM final), 16.5µl PBS,
1027 0.5µl 1% digitonin, 0.5µl 10% Tween-20 and 5µl H2O) at 37°C and 1000 rpm on a thermomixer for
1028 30 min. The reaction was stopped by adding 250µl of DNA Binding Buffer and DNA was isolated using
1029 the Clean and Concentrator-5 Kit (Zymo; D4013). Libraries were produced by PCR amplification of
1030 tagmented DNA and sequenced on a NextSeq 2000 sequencer 50bp Paired End.

1031 ***Bioinformatic analysis***

1032 The ATAC-seq data processed as previously described (Fei et al., 2023) and visualized with RPKM
1033 normalization and a binsize of 10. Briefly, for mapping of ATAC-seq data to both human genome

1034 and virus genome, we constructed a hybrid genome that included the hg38/GRCh38 version of human
1035 genome and Kaposi sarcoma herpesvirus genome (GenBank id: HQ404500.1) (referred as hybrid
1036 genome from now on). This hybrid genome included human chromosomes 1-21, X, Y and KSHV
1037 genome. The hybrid genome was used for all the ATAC-seq analysis steps. Briefly, Pearson
1038 correlation between the samples was calculated and visualized using deeptools (v.3.1.3) with outlier
1039 removal. Differential analysis of the chromatin accessibility in the ATAC-seq samples was done in R
1040 using Diffbind (v3.16.0). The analysis was conducted using alignment files and narrowPeak files. Sites
1041 with a false discovery rate (FDR) value of less than 0.05 were defined as differentially accessible.
1042 Differential site locations were compared using bedtools and visualized as heatmaps using deeptools
1043 with bigwig files. ATAC-seq signal in the viral genome was visualized using pyGenomeTracks (v3.9)
1044 with bigwig files. For the visualization of the human genome sites, the bigwig files were converted into
1045 bedGraph format using bigWigToBedGraph (v377) and the genomic coordinates were plotted using
1046 Spark (v2.6.2). Homer v4.10.4 was used to perform de novo motif analysis on the differential ATAC-
1047 seq sites. The chromatin accessibility loss and gain sites were ranked according to their
1048 log2FoldChange and up to 1000 differential accessibility sites with the highest fold change were
1049 selected for the motif analysis. findMotifsGenome.pl script was used to run de novo motif analysis
1050 with the hybrid genome using default parameters. Transcription factor Occupancy prediction By
1051 Investigation of ATAC-seq Signal (TOBIAS, v0.13.3) was used to predict transcription factor binding
1052 differences as previously described in (Fei et al., 2023). The gain and loss groups are defined as
1053 the TFs having -log10(p-value) above the 95% quantile or differential binding scores in the
1054 bottom or top 5% of the scores. Motifs were retrieved from Jaspar database.
1055 (https://jaspar.elixir.no/download/data/2024/CORE/JASPAR2024_CORE_vertebrates_non-
1056 redundant_pfms_jaspar.txt) and the results were visualized using ggplot2 (v3.5.1).

1057 **Statistical analysis**

1058 Graphical presentations and statistical analysis were generated with GraphPad Prism Software v9.0
1059 (Dotmatics). For statistical evaluation of the RT-qPCR data for relative KSHV genome copies, the
1060 logarithmic values were converted to linear log2 scale values by using the double delta CT (2-ΔΔ CT)
1061 method. Human genomic actin when measuring DNA, and actin when measuring mRNA were used
1062 as internal control and accounted in the calculations to correct differences in the RNA and DNA
1063 amount. The data is presented as individual values ± standard deviation (SD) between biological
1064 replicates unless otherwise reported. Statistical differences between groups were evaluated with
1065 either Student's *t*-test (two-tailed) or Welch's *t*-test, or ordinary one-way ANOVA followed by Dunnett
1066 or Tukey correction for multiple comparisons. Further details can be found from figure texts with p-
1067 values considered significant indicated by asterisk.

1068 **Resource availability**

Further information and requests for reagents may be directed to and will be fulfilled by the lead contacts PMO and MF.

Materials availability

This study did not generate new unique reagents.

Data and code availability

All original data is available upon request and will be made available as of the date of publication.

References

Adang, L. A., Parsons, C. H., & Kedes, D. H. (2006). Asynchronous progression through the lytic cascade and variations in intracellular viral loads revealed by high-throughput single-cell analysis of Kaposi's sarcoma-associated herpesvirus infection. *J Virol*, *80*(20), 10073-10082. https://doi.org/10.1128/JVI.01156-06

Aguilar, B., Choi, I., Choi, D., Chung, H. K., Lee, S., Yoo, J., Lee, Y. S., Maeng, Y. S., Lee, H. N., Park, E., Kim, K. E., Kim, N. Y., Baik, J. M., Jung, J. U., Koh, C. J., & Hong, Y. K. (2012). Lymphatic reprogramming by Kaposi sarcoma herpes virus promotes the oncogenic activity of the virus-encoded G-protein-coupled receptor. *Cancer Res*, *72*(22), 5833-5842. https://doi.org/10.1158/0008-5472.CAN-12-1229

Alvarez-Kuglen, M., Ninomiya, K., Qin, H., Rodriguez, D., Fiengo, L., Farhy, C., Hsu, W. M., Kirk, B., Havas, A., Feng, G. S., Roberts, A. J., Anderson, R. M., Serrano, M., Adams, P. D., Sharpee, T. O., & Terskikh, A. V. (2024). ImAge quantitates aging and rejuvenation. *Nat Aging*, *4*(9), 1308-1327. https://doi.org/10.1038/s43587-024-00685-1

Aranguren, X. L., Beerens, M., Coppiello, G., Wiese, C., Vandersmissen, I., Lo Nigro, A., Verfaillie, C. M., Gessler, M., & Luttun, A. (2013). COUP-TFII orchestrates venous and lymphatic endothelial identity by homo- or hetero-dimerisation with PROX1. *J Cell Sci*, *126*(Pt 5), 1164-1175. https://doi.org/10.1242/jcs.116293

Ballestas, M. E., & Kaye, K. M. (2001). Kaposi's sarcoma-associated herpesvirus latency-associated nuclear antigen 1 mediates episome persistence through cis-acting terminal repeat (TR) sequence and specifically binds TR DNA. *J Virol*, *75*(7), 3250-3258. https://doi.org/10.1128/JVI.75.7.3250-3258.2001

Barbera, A. J., Chodaparambil, J. V., Kelley-Clarke, B., Joukov, V., Walter, J. C., Luger, K., & Kaye, K. M. (2006). The nucleosomal surface as a docking station for Kaposi's sarcoma herpesvirus LANA. *Science*, *311*(5762), 856-861. https://doi.org/10.1126/science.1120541

Bartkova, J., Moudry, P., Hodny, Z., Lukas, J., Rajpert-De Meyts, E., & Bartek, J. (2011). Heterochromatin marks HP1gamma, HP1alpha and H3K9me3, and DNA damage response activation in human testis development and germ cell tumours. *Int J Androl*, *34*(4 Pt 2), e103-113. https://doi.org/10.1111/j.1365-2605.2010.01096.x

Battistello, E., Hixon, K. A., Comstock, D. E., Collings, C. K., Chen, X., Rodriguez Hernaez, J., Lee, S., Cervantes, K. S., Hinkley, M. M., Ntatsoulis, K., Cesarano, A., Hockemeyer, K., Haining, W. N., Witkowski, M. T., Qi, J., Tsirigos, A., Perna, F., Aifantis, I., & Kadoch, C. (2023). Stepwise activities of mSWI/SNF family chromatin remodeling complexes direct T cell activation and exhaustion. *Mol Cell*, *83*(8), 1216-1236 e1212. https://doi.org/10.1016/j.molcel.2023.02.026

Boija, A., Klein, I. A., Sabari, B. R., Dall'Agnese, A., Coffey, E. L., Zamudio, A. V., Li, C. H., Shrinivas, K., Manteiga, J. C., Hannett, N. M., Abraham, B. J., Afeyan, L. K., Guo, Y. E., Rimel, J. K., Fant, C. B., Schuijers, J., Lee, T. I., Taatjes, D. J., & Young, R. A. (2018). Transcription Factors Activate Genes through the Phase-Separation Capacity of Their Activation Domains. *Cell*, *175*(7), 1842-1855 e1816. https://doi.org/10.1016/j.cell.2018.10.042

Buenrostro, J. D., Wu, B., Chang, H. Y., & Greenleaf, W. J. (2015). ATAC-seq: A Method for Assaying Chromatin Accessibility Genome-Wide. *Curr Protoc Mol Biol*, *109*, 21 29 21-21 29 29. https://doi.org/10.1002/0471142727.mb2129s109

Bulyk, M. L., Drouin, J., Harrison, M. M., Taipale, J., & Zaret, K. S. (2023). Pioneer factors - key regulators of chromatin and gene expression. *Nat Rev Genet*, *24*(12), 809-815. https://doi.org/10.1038/s41576-023-00648-z

Carroll, P. A., Brazeau, E., & Lagunoff, M. (2004). Kaposi's sarcoma-associated herpesvirus infection of blood endothelial cells induces lymphatic differentiation. *Virology*, *328*(1), 7-18. https://doi.org/10.1016/j.virol.2004.07.008

1155 Centore, R. C., Sandoval, G. J., Soares, L. M. M., Kadoch, C., & Chan, H. M. (2020). Mammalian
1156 SWI/SNF Chromatin Remodeling Complexes: Emerging Mechanisms and Therapeutic
1157 Strategies. *Trends Genet*, *36*(12), 936-950. https://doi.org/10.1016/j.tig.2020.07.011
1158 Cesarman, E., Damania, B., Krown, S. E., Martin, J., Bower, M., & Whitby, D. (2019). Kaposi
1159 sarcoma. *Nat Rev Dis Primers*, *5*(1), 9. https://doi.org/10.1038/s41572-019-0060-9
1160 Chen, J., Zhang, Z., Li, L., Chen, B. C., Revyakin, A., Hajj, B., Legant, W., Dahan, M., Lionnet, T.,
1161 Betzig, E., Tjian, R., & Liu, Z. (2014). Single-molecule dynamics of enhanceosome assembly
1162 in embryonic stem cells. *Cell*, *156*(6), 1274-1285. https://doi.org/10.1016/j.cell.2014.01.062
1163 Cheng, F., Pekkonen, P., Laurinavicius, S., Sugiyama, N., Henderson, S., Gunther, T., Rantanen, V.,
1164 Kaivanto, E., Aavikko, M., Sarek, G., Hautaniemi, S., Biberfeld, P., Aaltonen, L., Grundhoff,
1165 A., Boshoff, C., Alitalo, K., Lehti, K., & Ojala, P. M. (2011). KSHV-initiated notch activation
1166 leads to membrane-type-1 matrix metalloproteinase-dependent lymphatic endothelial-to-
1167 mesenchymal transition. *Cell Host Microbe*, *10*(6), 577-590.
1168 https://doi.org/10.1016/j.chom.2011.10.011
1169 Choi, D., Park, E., Kim, K. E., Jung, E., Seong, Y. J., Zhao, L., Madhavan, S., Daghlian, G., Lee, H.
1170 H., Daghlian, P. T., Daghlian, S., Bui, K., Koh, C. J., Wong, A. K., Cho, I. T., & Hong, Y. K.
1171 (2020). The Lymphatic Cell Environment Promotes Kaposi Sarcoma Development by Prox1-
1172 Enhanced Productive Lytic Replication of Kaposi Sarcoma Herpes Virus. *Cancer Res*, *80*(15),
1173 3130-3144. https://doi.org/10.1158/0008-5472.CAN-19-3105
1174 Cohen, S. M., Chastain, P. D., 2nd, Rosson, G. B., Groh, B. S., Weissman, B. E., Kaufman, D. G., &
1175 Bultman, S. J. (2010). BRG1 co-localizes with DNA replication factors and is required for
1176 efficient replication fork progression. *Nucleic Acids Res*, *38*(20), 6906-6919.
1177 https://doi.org/10.1093/nar/gkq559
1178 Corces, M. R., Trevino, A. E., Hamilton, E. G., Greenside, P. G., Sinnott-Armstrong, N. A., Vesuna,
1179 S., Satpathy, A. T., Rubin, A. J., Montine, K. S., Wu, B., Kathiria, A., Cho, S. W., Mumbach,
1180 M. R., Carter, A. C., Kasowski, M., Orloff, L. A., Risca, V. I., Kundaje, A., Khavari, P.
1181 A.,…Chang, H. Y. (2017). An improved ATAC-seq protocol reduces background and enables
1182 interrogation of frozen tissues. *Nat Methods*, *14*(10), 959-962.
1183 https://doi.org/10.1038/nmeth.4396
1184 Digman, M. A., Dalal, R., Horwitz, A. F., & Gratton, E. (2008). Mapping the number of molecules
1185 and brightness in the laser scanning microscope. *Biophys J*, *94*(6), 2320-2332.
1186 https://doi.org/10.1529/biophysj.107.114645
1187 DiMaio, T. A., Vogt, D. T., & Lagunoff, M. (2020). KSHV requires vCyclin to overcome replicative
1188 senescence in primary human lymphatic endothelial cells. *PLoS Pathog*, *16*(6), e1008634.
1189 https://doi.org/10.1371/journal.ppat.1008634
1190 Dodonova, S. O., Zhu, F., Dienemann, C., Taipale, J., & Cramer, P. (2020). Nucleosome-bound SOX2
1191 and SOX11 structures elucidate pioneer factor function. *Nature*, *580*(7805), 669-672.
1192 https://doi.org/10.1038/s41586-020-2195-y
1193 Downes, M., & Koopman, P. (2001). SOX18 and the transcriptional regulation of blood vessel
1194 development. *Trends Cardiovasc Med*, *11*(8), 318-324. https://doi.org/10.1016/s1050-
1195 1738(01)00131-1
1196 Dreier, M. R., Walia, J., & de la Serna, I. L. (2024). Targeting SWI/SNF Complexes in Cancer:
1197 Pharmacological Approaches and Implications. *Epigenomes*, *8*(1).
1198 https://doi.org/10.3390/epigenomes8010007
1199 Duong, T., Proulx, S. T., Luciani, P., Leroux, J. C., Detmar, M., Koopman, P., & Francois, M. (2012).
1200 Genetic ablation of SOX18 function suppresses tumor lymphangiogenesis and metastasis of
1201 melanoma in mice. *Cancer Res*, *72*(12), 3105-3114. https://doi.org/10.1158/0008-5472.CAN-
1202 11-4026

1203 Erdos, G., & Dosztanyi, Z. (2024). AIUPred: combining energy estimation with deep learning for the
1204 enhanced prediction of protein disorder. *Nucleic Acids Res*, *52*(W1), W176-W181.
1205 https://doi.org/10.1093/nar/gkae385
1206 Farhy, C., Hariharan, S., Ylanko, J., Orozco, L., Zeng, F. Y., Pass, I., Ugarte, F., Forsberg, E. C.,
1207 Huang, C. T., Andrews, D. W., & Terskikh, A. V. (2019). Improving drug discovery using
1208 image-based multiparametric analysis of the epigenetic landscape. *Elife*, *8*.
1209 https://doi.org/10.7554/eLife.49683
1210 Farnaby, W., Koegl, M., Roy, M. J., Whitworth, C., Diers, E., Trainor, N., Zollman, D., Steurer, S.,
1211 Karolyi-Oezguer, J., Riedmueller, C., Gmaschitz, T., Wachter, J., Dank, C., Galant, M., Sharps,
1212 B., Rumpel, K., Traxler, E., Gerstberger, T., Schnitzer, R.,…Ciulli, A. (2019). Publisher
1213 Correction: BAF complex vulnerabilities in cancer demonstrated via structure-based PROTAC
1214 design. *Nat Chem Biol*, *15*(8), 846. https://doi.org/10.1038/s41589-019-0329-z
1215 Fei, L., Zhang, K., Poddar, N., Hautaniemi, S., & Sahu, B. (2023). Single-cell epigenome analysis
1216 identifies molecular events controlling direct conversion of human fibroblasts to pancreatic
1217 ductal-like cells. *Dev Cell*, *58*(18), 1701-1715 e1708.
1218 https://doi.org/10.1016/j.devcel.2023.08.023
1219 Fontaine, F., Overman, J., Moustaqil, M., Mamidyala, S., Salim, A., Narasimhan, K., Prokoph, N.,
1220 Robertson, A. A. B., Lua, L., Alexandrov, K., Koopman, P., Capon, R. J., Sierecki, E., Gambin,
1221 Y., Jauch, R., Cooper, M. A., Zuegg, J., & Francois, M. (2017). Small-Molecule Inhibitors of
1222 the SOX18 Transcription Factor. *Cell Chem Biol*, *24*(3), 346-359.
1223 https://doi.org/10.1016/j.chembiol.2017.01.003
1224 Fontijn, R. D., Favre, J., Naaijkens, B. A., Meinster, E., Paauw, N. J., Ragghoe, S. L., Nauta, T. D.,
1225 van den Broek, M. A., Weijers, E. M., Niessen, H. W., Koolwijk, P., & Horrevoets, A. J.
1226 (2014). Adipose tissue-derived stromal cells acquire endothelial-like features upon
1227 reprogramming with SOX18. *Stem Cell Res*, *13*(3 Pt A), 367-378.
1228 https://doi.org/10.1016/j.scr.2014.09.004
1229 Francois, M., Caprini, A., Hosking, B., Orsenigo, F., Wilhelm, D., Browne, C., Paavonen, K.,
1230 Karnezis, T., Shayan, R., Downes, M., Davidson, T., Tutt, D., Cheah, K. S., Stacker, S. A.,
1231 Muscat, G. E., Achen, M. G., Dejana, E., & Koopman, P. (2008). Sox18 induces development
1232 of the lymphatic vasculature in mice. *Nature*, *456*(7222), 643-647.
1233 https://doi.org/10.1038/nature07391
1234 Gasperini, P., Espigol-Frigole, G., McCormick, P. J., Salvucci, O., Maric, D., Uldrick, T. S.,
1235 Polizzotto, M. N., Yarchoan, R., & Tosato, G. (2012). Kaposi sarcoma herpesvirus promotes
1236 endothelial-to-mesenchymal transition through Notch-dependent signaling. *Cancer Res*, *72*(5),
1237 1157-1169. https://doi.org/10.1158/0008-5472.CAN-11-3067
1238 Golas, G., Alonso, J. D., & Toth, Z. (2019). Characterization of de novo lytic infection of dermal
1239 lymphatic microvascular endothelial cells by Kaposi's sarcoma-associated herpesvirus.
1240 *Virology*, *536*, 27-31. https://doi.org/10.1016/j.virol.2019.07.028
1241 Gramolelli, S., Cheng, J., Martinez-Corral, I., Vaha-Koskela, M., Elbasani, E., Kaivanto, E., Rantanen,
1242 V., Tuohinto, K., Hautaniemi, S., Bower, M., Haglund, C., Alitalo, K., Makinen, T., Petrova,
1243 T. V., Lehti, K., & Ojala, P. M. (2018). PROX1 is a transcriptional regulator of MMP14. *Sci*
1244 *Rep*, *8*(1), 9531. https://doi.org/10.1038/s41598-018-27739-w
1245 Gramolelli, S., Elbasani, E., Tuohinto, K., Nurminen, V., Gunther, T., Kallinen, R. E., Kaijalainen, S.
1246 P., Diaz, R., Grundhoff, A., Haglund, C., Ziegelbauer, J. M., Pellinen, T., Bower, M., Francois,
1247 M., & Ojala, P. M. (2020). Oncogenic Herpesvirus Engages Endothelial Transcription Factors
1248 SOX18 and PROX1 to Increase Viral Genome Copies and Virus Production. *Cancer Res*,
1249 *80*(15), 3116-3129. https://doi.org/10.1158/0008-5472.CAN-19-3103
1250 Gramolelli, S., & Ojala, P. M. (2017). Kaposi's sarcoma herpesvirus-induced endothelial cell
1251 reprogramming supports viral persistence and contributes to Kaposi's sarcoma tumorigenesis.
1252 *Curr Opin Virol*, *26*, 156-162. https://doi.org/10.1016/j.coviro.2017.09.002

1253 Gwack, Y., Baek, H. J., Nakamura, H., Lee, S. H., Meisterernst, M., Roeder, R. G., & Jung, J. U.
1254 (2003). Principal role of TRAP/mediator and SWI/SNF complexes in Kaposi's sarcoma-
1255 associated herpesvirus RTA-mediated lytic reactivation. *Mol Cell Biol*, *23*(6), 2055-2067.
1256 https://doi.org/10.1128/MCB.23.6.2055-2067.2003
1257 Hagey, D. W., Bergsland, M., & Muhr, J. (2022). SOX2 transcription factor binding and function.
1258 *Development*, *149*(14). https://doi.org/10.1242/dev.200547
1259 Han, C., Niu, D., & Lan, K. (2024). Rewriting Viral Fate: Epigenetic and Transcriptional Dynamics
1260 in KSHV Infection. *Viruses*, *16*(12). https://doi.org/10.3390/v16121870
1261 Hellert, J., Weidner-Glunde, M., Krausze, J., Lunsdorf, H., Ritter, C., Schulz, T. F., & Luhrs, T. (2015).
1262 The 3D structure of Kaposi sarcoma herpesvirus LANA C-terminal domain bound to DNA.
1263 *Proc Natl Acad Sci U S A*, *112*(21), 6694-6699. https://doi.org/10.1073/pnas.1421804112
1264 Hinde, E., Cardarelli, F., & Gratton, E. (2015). Spatiotemporal regulation of Heterochromatin Protein
1265 1-alpha oligomerization and dynamics in live cells. *Sci Rep*, *5*, 12001.
1266 https://doi.org/10.1038/srep12001
1267 Hinde, E., Pandzic, E., Yang, Z., Ng, I. H., Jans, D. A., Bogoyevitch, M. A., Gratton, E., & Gaus, K.
1268 (2016). Quantifying the dynamics of the oligomeric transcription factor STAT3 by pair
1269 correlation of molecular brightness. *Nat Commun*, *7*, 11047.
1270 https://doi.org/10.1038/ncomms11047
1271 Hoffman, G. R., Rahal, R., Buxton, F., Xiang, K., McAllister, G., Frias, E., Bagdasarian, L., Huber,
1272 J., Lindeman, A., Chen, D., Romero, R., Ramadan, N., Phadke, T., Haas, K., Jaskelioff, M.,
1273 Wilson, B. G., Meyer, M. J., Saenz-Vash, V., Zhai, H.,…Jagani, Z. (2014). Functional
1274 epigenetics approach identifies BRM/SMARCA2 as a critical synthetic lethal target in BRG1-
1275 deficient cancers. *Proc Natl Acad Sci U S A*, *111*(8), 3128-3133.
1276 https://doi.org/10.1073/pnas.1316793111
1277 Holm, A., Graus, M. S., Wylie-Sears, J., Tan, J. W. H., Alvarez-Harmon, M., Borgelt, L., Nasim, S.,
1278 Chung, L., Jain, A., Sun, M., Sun, L., Brouillard, P., Lekwuttikarn, R., Qi, Y., Teng, J., Vikkula,
1279 M., Kozakewich, H., Mulliken, J. B., Francois, M., & Bischoff, J. (2025). An endothelial
1280 SOX18-mevalonate pathway axis enables repurposing of statins for infantile hemangioma. *J*
1281 *Clin Invest*, *135*(7). https://doi.org/10.1172/JCI179782
1282 Hong, Y. K., Foreman, K., Shin, J. W., Hirakawa, S., Curry, C. L., Sage, D. R., Libermann, T., Dezube,
1283 B. J., Fingeroth, J. D., & Detmar, M. (2004). Lymphatic reprogramming of blood vascular
1284 endothelium by Kaposi sarcoma-associated herpesvirus. *Nat Genet*, *36*(7), 683-685.
1285 https://doi.org/10.1038/ng1383
1286 Juillard, F., Tan, M., Li, S., & Kaye, K. M. (2016). Kaposi's Sarcoma Herpesvirus Genome Persistence.
1287 *Front Microbiol*, *7*, 1149. https://doi.org/10.3389/fmicb.2016.01149
1288 Jung, H. S., Suknuntha, K., Kim, Y. H., Liu, P., Dettle, S. T., Sedzro, D. M., Smith, P. R., Thomson,
1289 J. A., Ong, I. M., & Slukvin, II. (2023). SOX18-enforced expression diverts hemogenic
1290 endothelium-derived progenitors from T towards NK lymphoid pathways. *iScience*, *26*(5),
1291 106621. https://doi.org/10.1016/j.isci.2023.106621
1292 Ka-Yue Chow, L., Lai-Shun Chung, D., Tao, L., Chan, K. F., Tung, S. Y., Cheong Ngan, R. K., Ng,
1293 W. T., Wing-Mui Lee, A., Yau, C. C., Lai-Wan Kwong, D., Ho-Fun Lee, V., Lam, K. O., Liu,
1294 J., Chen, H., Dai, W., & Lung, M. L. (2022). Epigenomic landscape study reveals molecular
1295 subtypes and EBV-associated regulatory epigenome reprogramming in nasopharyngeal
1296 carcinoma. *EBioMedicine*, *86*, 104357. https://doi.org/10.1016/j.ebiom.2022.104357
1297 Larson, A. G., Elnatan, D., Keenen, M. M., Trnka, M. J., Johnston, J. B., Burlingame, A. L., Agard,
1298 D. A., Redding, S., & Narlikar, G. J. (2017). Liquid droplet formation by HP1alpha suggests a
1299 role for phase separation in heterochromatin. *Nature*, *547*(7662), 236-240.
1300 https://doi.org/10.1038/nature22822

1301 Lee, D., Lee, D. Y., Hwang, Y. S., Seo, H. R., Lee, S. A., & Kwon, J. (2021). The Bromodomain
1302 Inhibitor PFI-3 Sensitizes Cancer Cells to DNA Damage by Targeting SWI/SNF. *Mol Cancer*
1303 *Res*, *19*(5), 900-912. https://doi.org/10.1158/1541-7786.MCR-20-0289
1304 Liu, X., Salokas, K., Tamene, F., Jiu, Y., Weldatsadik, R. G., Ohman, T., & Varjosalo, M. (2018). An
1305 AP-MS- and BioID-compatible MAC-tag enables comprehensive mapping of protein
1306 interactions and subcellular localizations. *Nat Commun*, *9*(1), 1188.
1307 https://doi.org/10.1038/s41467-018-03523-2
1308 Lu, F., Zhou, J., Wiedmer, A., Madden, K., Yuan, Y., & Lieberman, P. M. (2003). Chromatin
1309 remodeling of the Kaposi's sarcoma-associated herpesvirus ORF50 promoter correlates with
1310 reactivation from latency. *J Virol*, *77*(21), 11425-11435.
1311 https://doi.org/10.1128/jvi.77.21.11425-11435.2003
1312 Malone, H. A., & Roberts, C. W. M. (2024). Chromatin remodellers as therapeutic targets. *Nat Rev*
1313 *Drug Discov*, *23*(9), 661-681. https://doi.org/10.1038/s41573-024-00978-5
1314 McCann, A. J., Lou, J., Moustaqil, M., Graus, M. S., Blum, A., Fontaine, F., Liu, H., Luu, W., Rudolffi-
1315 Soto, P., Koopman, P., Sierecki, E., Gambin, Y., Meunier, F. A., Liu, Z., Hinde, E., & Francois,
1316 M. (2021). A dominant-negative SOX18 mutant disrupts multiple regulatory layers essential
1317 to transcription factor activity. *Nucleic Acids Res*, *49*(19), 10931-10955.
1318 https://doi.org/10.1093/nar/gkab820
1319 Moustaqil, M., Fontaine, F., Overman, J., McCann, A., Bailey, T. L., Rudolffi Soto, P., Bhumkar, A.,
1320 Giles, N., Hunter, D. J. B., Gambin, Y., Francois, M., & Sierecki, E. (2018). Homodimerization
1321 regulates an endothelial specific signature of the SOX18 transcription factor. *Nucleic Acids*
1322 *Res*, *46*(21), 11381-11395. https://doi.org/10.1093/nar/gky897
1323 Myoung, J., & Ganem, D. (2011). Generation of a doxycycline-inducible KSHV producer cell line of
1324 endothelial origin: maintenance of tight latency with efficient reactivation upon induction. *J*
1325 *Virol Methods*, *174*(1-2), 12-21. https://doi.org/10.1016/j.jviromet.2011.03.012
1326 Nakagawa, M., Koyanagi, M., Tanabe, K., Takahashi, K., Ichisaka, T., Aoi, T., Okita, K., Mochiduki,
1327 Y., Takizawa, N., & Yamanaka, S. (2008). Generation of induced pluripotent stem cells
1328 without Myc from mouse and human fibroblasts. *Nat Biotechnol*, *26*(1), 101-106.
1329 https://doi.org/10.1038/nbt1374
1330 Neugebauer, E., Bastidas-Quintero, A. M., Weidl, D., & Full, F. (2023). Pioneer factors in viral
1331 infection. *Front Immunol*, *14*, 1286617. https://doi.org/10.3389/fimmu.2023.1286617
1332 Ojala, P. M., & Schulz, T. F. (2014). Manipulation of endothelial cells by KSHV: implications for
1333 angiogenesis and aberrant vascular differentiation. *Semin Cancer Biol*, *26*, 69-77.
1334 https://doi.org/10.1016/j.semcancer.2014.01.008
1335 Overman, J., Fontaine, F., Moustaqil, M., Mittal, D., Sierecki, E., Sacilotto, N., Zuegg, J., Robertson,
1336 A. A. B., Holmes, K., Salim, A. A., Mamidyala, S., Butler, M. S., Robinson, A. S., Lesieur, E.,
1337 Johnston, W., Alexandrov, K., Black, B. L., Hogan, B. M., De Val, S.,…Francois, M. (2017).
1338 Pharmacological targeting of the transcription factor SOX18 delays breast cancer in mice.
1339 *Elife*, *6*. https://doi.org/10.7554/eLife.21221
1340 Overman, J., Fontaine, F., Wylie-Sears, J., Moustaqil, M., Huang, L., Meurer, M., Chiang, I. K.,
1341 Lesieur, E., Patel, J., Zuegg, J., Pasquier, E., Sierecki, E., Gambin, Y., Hamdan, M.,
1342 Khosrotehrani, K., Andelfinger, G., Bischoff, J., & Francois, M. (2019). R-propranolol is a
1343 small molecule inhibitor of the SOX18 transcription factor in a rare vascular syndrome and
1344 hemangioma. *Elife*, *8*. https://doi.org/10.7554/eLife.43026
1345 Purushothaman, P., Dabral, P., Gupta, N., Sarkar, R., & Verma, S. C. (2016). KSHV Genome
1346 Replication and Maintenance. *Front Microbiol*, *7*, 54.
1347 https://doi.org/10.3389/fmicb.2016.00054
1348 Rajagopalan, S., Huang, F., & Fersht, A. R. (2011). Single-Molecule characterization of
1349 oligomerization kinetics and equilibria of the tumor suppressor p53. *Nucleic Acids Res*, *39*(6),
1350 2294-2303. https://doi.org/10.1093/nar/gkq800

1351 Roux, K. J., Kim, D. I., Burke, B., & May, D. G. (2018). BioID: A Screen for Protein-Protein
1352 Interactions. *Curr Protoc Protein Sci*, *91*, 19 23 11-19 23 15. https://doi.org/10.1002/cpps.51
1353 Sabari, B. R., Dall'Agnese, A., Boija, A., Klein, I. A., Coffey, E. L., Shrinivas, K., Abraham, B. J.,
1354 Hannett, N. M., Zamudio, A. V., Manteiga, J. C., Li, C. H., Guo, Y. E., Day, D. S., Schuijers,
1355 J., Vasile, E., Malik, S., Hnisz, D., Lee, T. I., Cisse, II,…Young, R. A. (2018). Coactivator
1356 condensation at super-enhancers links phase separation and gene control. *Science*, *361*(6400).
1357 https://doi.org/10.1126/science.aar3958
1358 Salido-Vallejo, R., Gonzalez-Menchen, A., Alcantara-Reifs, C., & Espana, A. (2022). Treatment With
1359 Oral Propranolol for Refractory Classic Cutaneous Kaposi Sarcoma. *JAMA Dermatol*, *158*(7),
1360 832-834. https://doi.org/10.1001/jamadermatol.2022.1278
1361 Schock, E. N., & LaBonne, C. (2020). Sorting Sox: Diverse Roles for Sox Transcription Factors
1362 During Neural Crest and Craniofacial Development. *Front Physiol*, *11*, 606889.
1363 https://doi.org/10.3389/fphys.2020.606889
1364 Schoelz, J. M., & Riddle, N. C. (2022). Functions of HP1 proteins in transcriptional regulation.
1365 *Epigenetics Chromatin*, *15*(1), 14. https://doi.org/10.1186/s13072-022-00453-8
1366 Schulz, T. F., Freise, A., & Stein, S. C. (2023). Kaposi sarcoma-associated herpesvirus latency-
1367 associated nuclear antigen: more than a key mediator of viral persistence. *Curr Opin Virol*, *61*,
1368 101336. https://doi.org/10.1016/j.coviro.2023.101336
1369 Seebauer, C. T., Graus, M. S., Huang, L., McCann, A., Wylie-Sears, J., Fontaine, F., Karnezis, T.,
1370 Zurakowski, D., Staffa, S. J., Meunier, F., Mulliken, J. B., Bischoff, J., & Francois, M. (2022).
1371 Non-beta blocker enantiomers of propranolol and atenolol inhibit vasculogenesis in infantile
1372 hemangioma. *J Clin Invest*, *132*(3). https://doi.org/10.1172/JCI151109
1373 Serge, A., Bertaux, N., Rigneault, H., & Marguet, D. (2008). Dynamic multiple-target tracing to probe
1374 spatiotemporal cartography of cell membranes. *Nat Methods*, *5*(8), 687-694.
1375 https://doi.org/10.1038/nmeth.1233
1376 Shaban, H. A., Friman, E. T., Deluz, C., Tollenaere, A., Katanayeva, N., & Suter, D. M. (2024).
1377 Individual transcription factors modulate both the micromovement of chromatin and its long-
1378 range structure. *Proc Natl Acad Sci U S A*, *121*(18), e2311374121.
1379 https://doi.org/10.1073/pnas.2311374121
1380 Sherwood, R. I., Hashimoto, T., O'Donnell, C. W., Lewis, S., Barkal, A. A., van Hoff, J. P., Karun,
1381 V., Jaakkola, T., & Gifford, D. K. (2014). Discovery of directional and nondirectional pioneer
1382 transcription factors by modeling DNase profile magnitude and shape. *Nat Biotechnol*, *32*(2),
1383 171-178. https://doi.org/10.1038/nbt.2798
1384 Si, H., Verma, S. C., & Robertson, E. S. (2006). Proteomic analysis of the Kaposi's sarcoma-associated
1385 herpesvirus terminal repeat element binding proteins. *J Virol*, *80*(18), 9017-9030.
1386 https://doi.org/10.1128/JVI.00297-06
1387 Singh, A., Modak, S. B., Chaturvedi, M. M., & Purohit, J. S. (2023). SWI/SNF Chromatin Remodelers:
1388 Structural, Functional and Mechanistic Implications. *Cell Biochem Biophys*, *81*(2), 167-187.
1389 https://doi.org/10.1007/s12013-023-01140-5
1390 Srinivasan, R. S., Geng, X., Yang, Y., Wang, Y., Mukatira, S., Studer, M., Porto, M. P., Lagutin, O.,
1391 & Oliver, G. (2010). The nuclear hormone receptor Coup-TFII is required for the initiation and
1392 early maintenance of Prox1 expression in lymphatic endothelial cells. *Genes Dev*, *24*(7), 696-
1393 707. https://doi.org/10.1101/gad.1859310
1394 Strom, A. R., Emelyanov, A. V., Mir, M., Fyodorov, D. V., Darzacq, X., & Karpen, G. H. (2017).
1395 Phase separation drives heterochromatin domain formation. *Nature*, *547*(7662), 241-245.
1396 https://doi.org/10.1038/nature22989
1397 Tuohinto, K., DiMaio, T. A., Kiss, E. A., Laakkonen, P., Saharinen, P., Karnezis, T., Lagunoff, M., &
1398 Ojala, P. M. (2023). KSHV infection of endothelial precursor cells with lymphatic
1399 characteristics as a novel model for translational Kaposi's sarcoma studies. *PLoS Pathog*, *19*(1),
1400 e1010753. https://doi.org/10.1371/journal.ppat.1010753

Uppal, T., Banerjee, S., Sun, Z., Verma, S. C., & Robertson, E. S. (2014). KSHV LANA--the master regulator of KSHV latency. *Viruses*, *6*(12), 4961-4998. https://doi.org/10.3390/v6124961

Verma, S. C., Cai, Q., Kreider, E., Lu, J., & Robertson, E. S. (2013). Comprehensive analysis of LANA interacting proteins essential for viral genome tethering and persistence. *PLoS One*, *8*(9), e74662. https://doi.org/10.1371/journal.pone.0074662

Wang, H. W., Trotter, M. W., Lagos, D., Bourboulia, D., Henderson, S., Makinen, T., Elliman, S., Flanagan, A. M., Alitalo, K., & Boshoff, C. (2004). Kaposi sarcoma herpesvirus-induced cellular reprogramming contributes to the lymphatic endothelial gene expression in Kaposi sarcoma. *Nat Genet*, *36*(7), 687-693. https://doi.org/10.1038/ng1384

Wanior, M., Kramer, A., Knapp, S., & Joerger, A. C. (2021). Exploiting vulnerabilities of SWI/SNF chromatin remodelling complexes for cancer therapy. *Oncogene*, *40*(21), 3637-3654. https://doi.org/10.1038/s41388-021-01781-x

Weissmann, S., Robitaille, A., Günther, T., Ziegler, M., & A., G. (2025). *Polycomb group proteins protect latent Kaposi sarcoma-associated herpesvirus from episome clearance and HUSH-dependent chromatin silencing* [preprint]. https://www.biorxiv.org/content/10.1101/2025.02.10.637455v1

Zaneveld, J. R., McMinds, R., & Vega Thurber, R. (2017). Stress and stability: applying the Anna Karenina principle to animal microbiomes. *Nat Microbiol*, *2*, 17121. https://doi.org/10.1038/nmicrobiol.2017.121

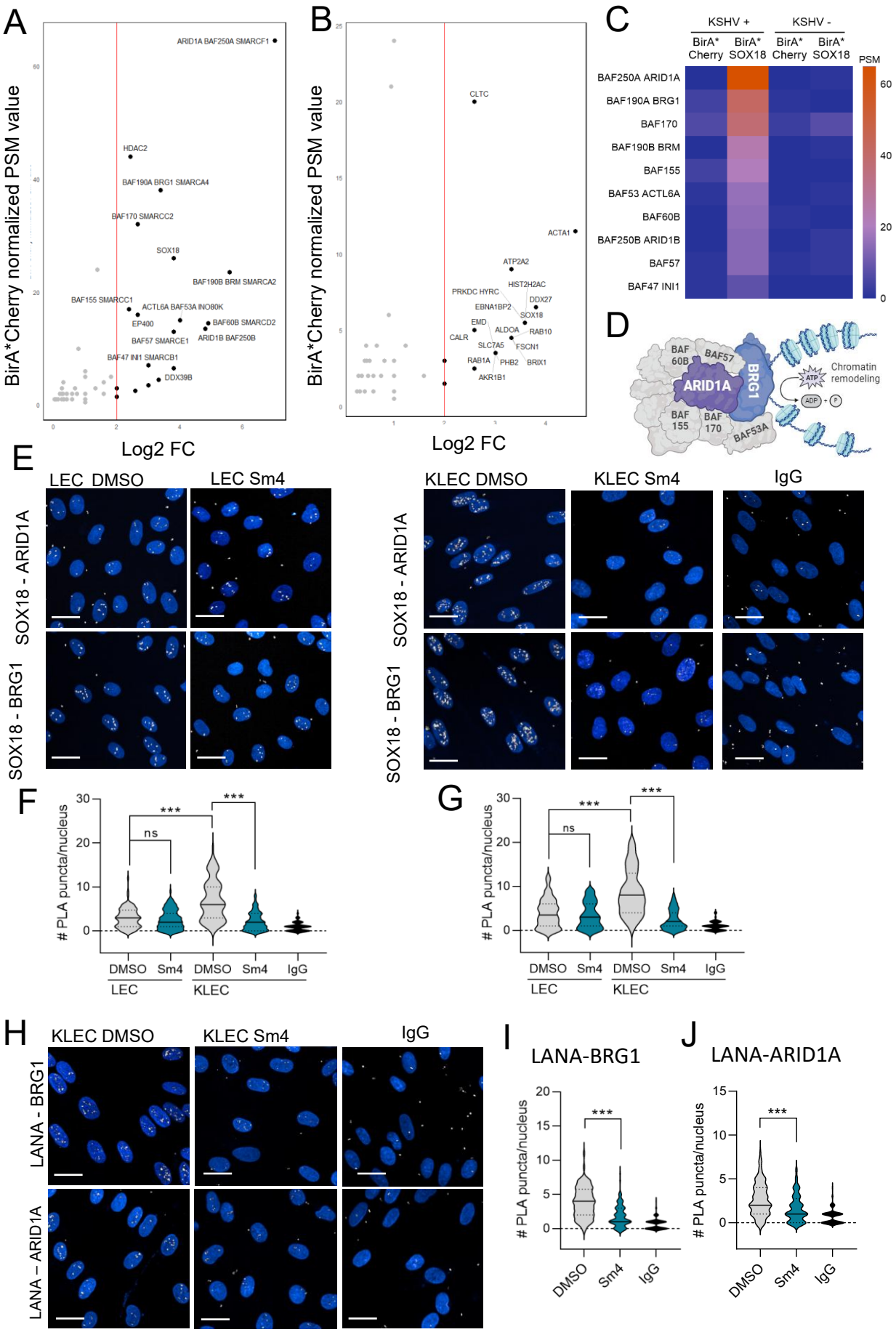
A
BirA*Cherry normalized PSM value
Log2 FC
ARID1A BAF250A SMARCF1
HDAC2
BAF190A BRG1 SMARCA4
BAF170 SMARCC2
SOX18
BAF190B BRM SMARCA2
BAF155 SMARCC1
ACTL6A BAF53A INO80K
EP400
BAF60B SMARCD2
BAF57 SMARCE1
ARID1B BAF250B
BAF47 INI1 SMARCB1
DDX39B
B
BirA*Cherry normalized PSM value
Log2 FC
CLTC
ACTA1
ATP2A2
HIST2H2AC
PRKDC HYRC
DDX27
EBNA1BP2
SOX18
EMD
ALDOA
RAB10
CALR
SLC7A5
FSCN1
RAB1A
PHB2
BRIX1
AKR1B1
C
KSHV +
KSHV -
BirA* Cherry
BirA* SOX18
BirA* Cherry
BirA* SOX18
PSM
BAF250A ARID1A
BAF190A BRG1
BAF170
BAF190B BRM
BAF155
BAF53 ACTL6A
BAF60B
BAF250B ARID1B
BAF57
BAF47 INI1
D
BAF 60B
BAF57
ARID1A
BRG1
BAF 155
BAF 170
BAF53A
ATP
Chromatin remodeling
ADP
P
E
LEC DMSO
LEC Sm4
KLEC DMSO
KLEC Sm4
IgG
SOX18 - ARID1A
SOX18 - BRG1
F
PLA puncta/nucleus
***
ns
DMSO
Sm4
IgG
LEC
KLEC
G
PLA puncta/nucleus
***
ns
DMSO
Sm4
IgG
LEC
KLEC
H
KLEC DMSO
KLEC Sm4
IgG
LANA - BRG1
LANA – ARID1A
I
LANA-BRG1
PLA puncta/nucleus
***
DMSO
Sm4
IgG
J
LANA-ARID1A
PLA puncta/nucleus
***
DMSO
Sm4
IgG

1442

1443 **Figure 1. SOX18 recruits SWI/SNF chromatin remodeling complex upon KSHV infection.**
1444 **A-B.** Bio-ID proximity-based protein-protein interaction screen using a BirA*-fusion of SOX18
1445 (BirA*SOX18) or Cherry (BirA*Cherry) as a control in **A.** stably KSHV-infected iSLK.219 cells or **B.**
1446 parental, uninfected SLK cells. The strength of the interaction of SOX18 with the indicated proteins is
1447 shown as ≥ 2 log2 fold change FC (x-axis) and BirA*Cherry bait-normalized PSM = peptide spectral
1448 matches (y-axis). All shown proteins have ≥2 unique peptides. **C.** Heatmap of the canonical SWI/SNF
1449 (cBAF) complex subunits in all conditions. **D.** A schematic of the cBAF complex; ARID1A and BRG1,
1450 the top interactors of SOX18, are highlighted in purple and blue, respectively. **E-H.** Validation of the
1451 selected interactions by PLA with the indicated antibodies. **E.** PLA images of uninfected LECs (LEC)
1452 and rKSHV.219 -infected LECs (KLEC) at 72 h.p.i (hours post infection) treated with Sm4 or DMSO
1453 for 72h and imaged with Opera Phenix 40x, nuclei were counterstained with Hoechst (33342), scale
1454 bar is 20μm. **F-G.** Quantification of nuclear PLA puncta from 10 fields (n=100 nuclei) for **F.** SOX18-
1455 ARID1A and **G.** SOX18-BRG1 interactions in all conditions. **H.** LANA-BRG1 and LANA-ARID1A PLA
1456 images and **I-J.** quantification of nuclear PLA puncta from 10 fields (n=100 nuclei) in KLECs.
1457 Statistical significance was determined by ordinary one-way ANOVA with Tukey correction for multiple
1458 comparisons; ***$p < 0.001$, **$p < 0.01$, *$p < 0.05$, ns = non-significant.

1459

1460

1461

1462

1463

1464

1465

1466

1467

1468

1469

1470

1471

1472

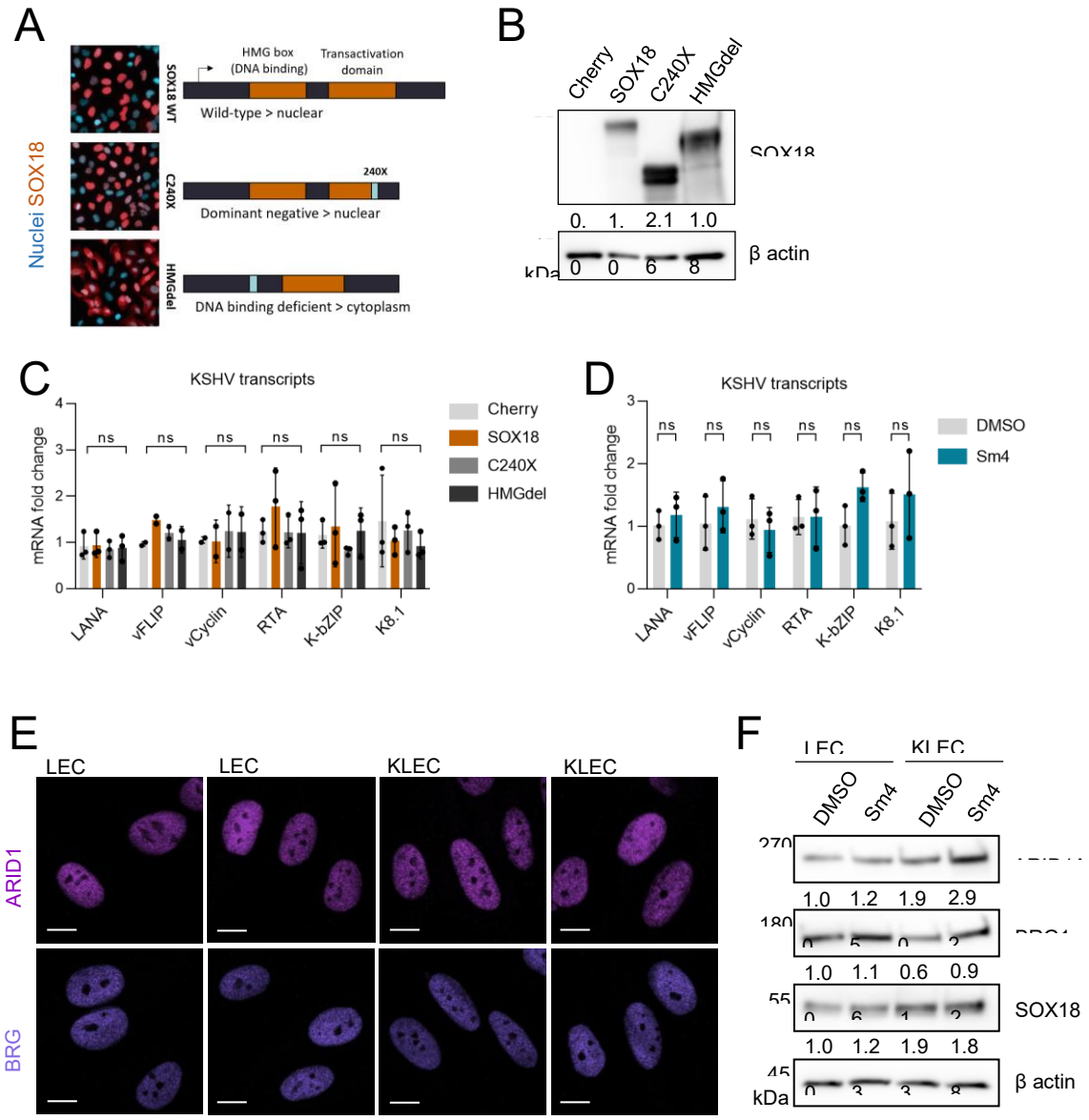

Supplementary Figure 1. Related to Fig 1.

A-C. HeLa cells expressing SOX18wt, mutants C240X (dominant-negative transactivation deficient) or HMGdel (DNA-binding deficient), or mCherry as a control, and thereafter infected with rKSHV.219 for 72h (KSHV-HeLa). **A.** IF images of the SOX18wt and mutants expressing cells labeled with anti-SOX18 antibody and a schematic of the constructs. **B.** Immunoblotting with anti-SOX18 antibody using β-actin as a loading control for normalization. **C.** RT-qPCR for the indicated viral genes in KSHV-HeLa. **D.** LECs infected with rKSHV.219 (KLECs) for 72 hours and treated with Sm4 or DMSO control for 24h and relative mRNA measured for indicated viral transcripts. Statistical significance was determined by one-way ANOVA with Dunnett correction for multiple comparisons; ns = non-significant. **E-F.** Uninfected LECs and KLECs 72h p.i. treated with DMSO or Sm4 for another 72h and E) labeled with anti-ARID1A and -BRG1 antibodies, nuclei were counterstained with Hoechst (33342), scale bar is 10μm, and F) immunoblotted for the indicated proteins and quantified as in B.

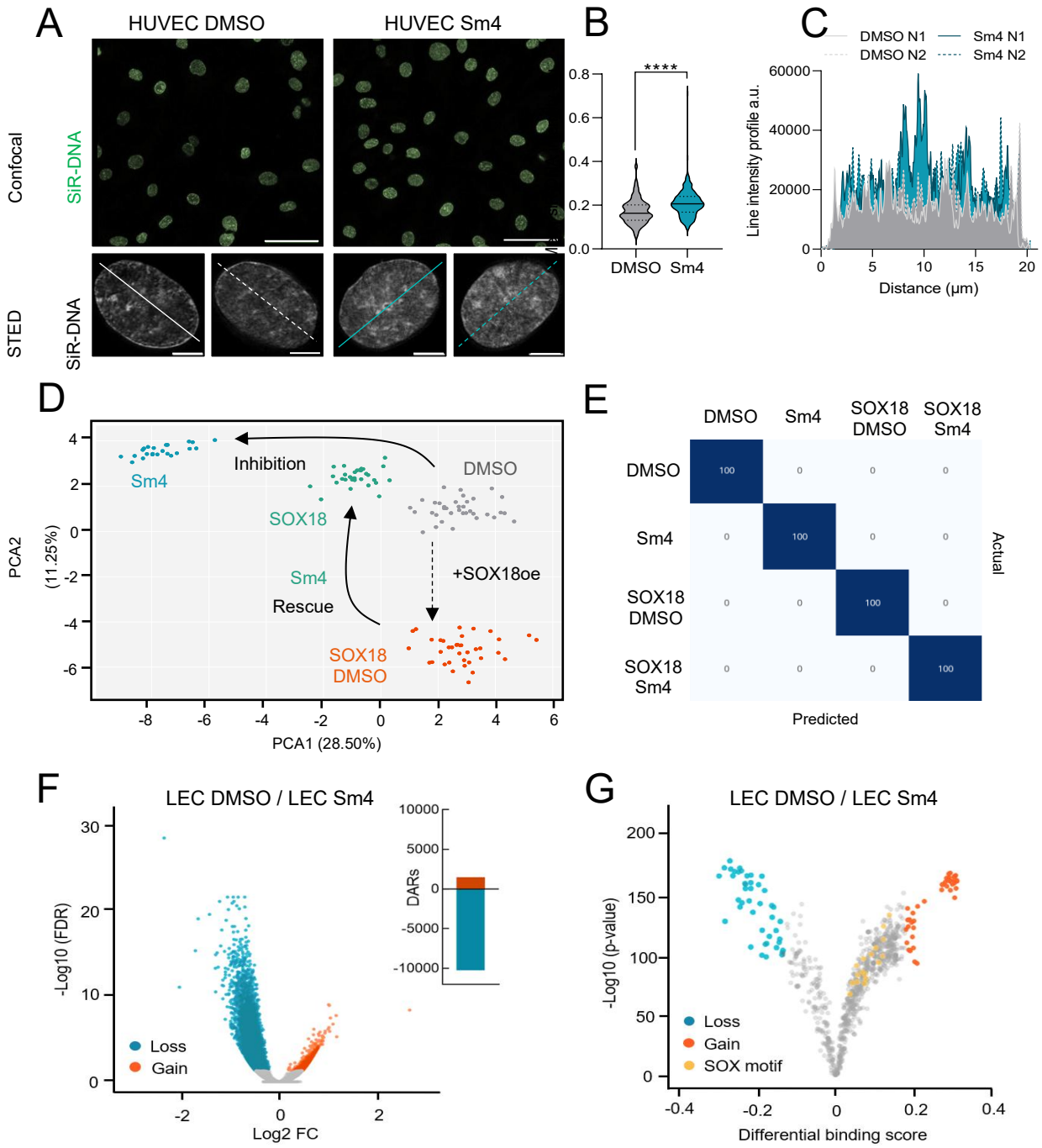

Figure 2. Perturbations to SOX18 causes changes in chromatin accessibility. **A.** Representative images of HUVECs treated with DMSO or Sm4 and stained with SiR-DNA, scale bar is 50µm for confocal images and 5µm for STED images. **B.** Mean intensity of SiR-DNA from cells in panel A, n ≥ 137 cells/condition. Statistical significance was determined by Mann-Whitney test ****p < 0.0001. **C.** Line intensity profile of STED images from panel A. Solid (N1) and dashed (N2) lines represent individual nuclei (N) line profiles. **D-E.** Quadratic discriminant MIEL analysis using texture features derived from images of HUVECs ± SOX18 over-expression and ± Sm4 treatment stained with DAPI. **D.** Scatter plot depict the first two discriminant factors for each cell population: each point

is a pool of 60 cells. **E.** Matrix showing results for the discriminant analysis. Numbers represent the percent classified correctly (diagonal) and incorrectly (off the diagonal). **F-G.** LECs treated with DMSO or Sm4 for 24h and subjected for ATAC-seq. **F.** Data presented as volcano plot showing the human genomic regions with significant loss (turquoise) or gain (red) of accessibility and as number of differentially accessible regions (DAR) that have changed and **G.** as TF differential binding score volcano plot.

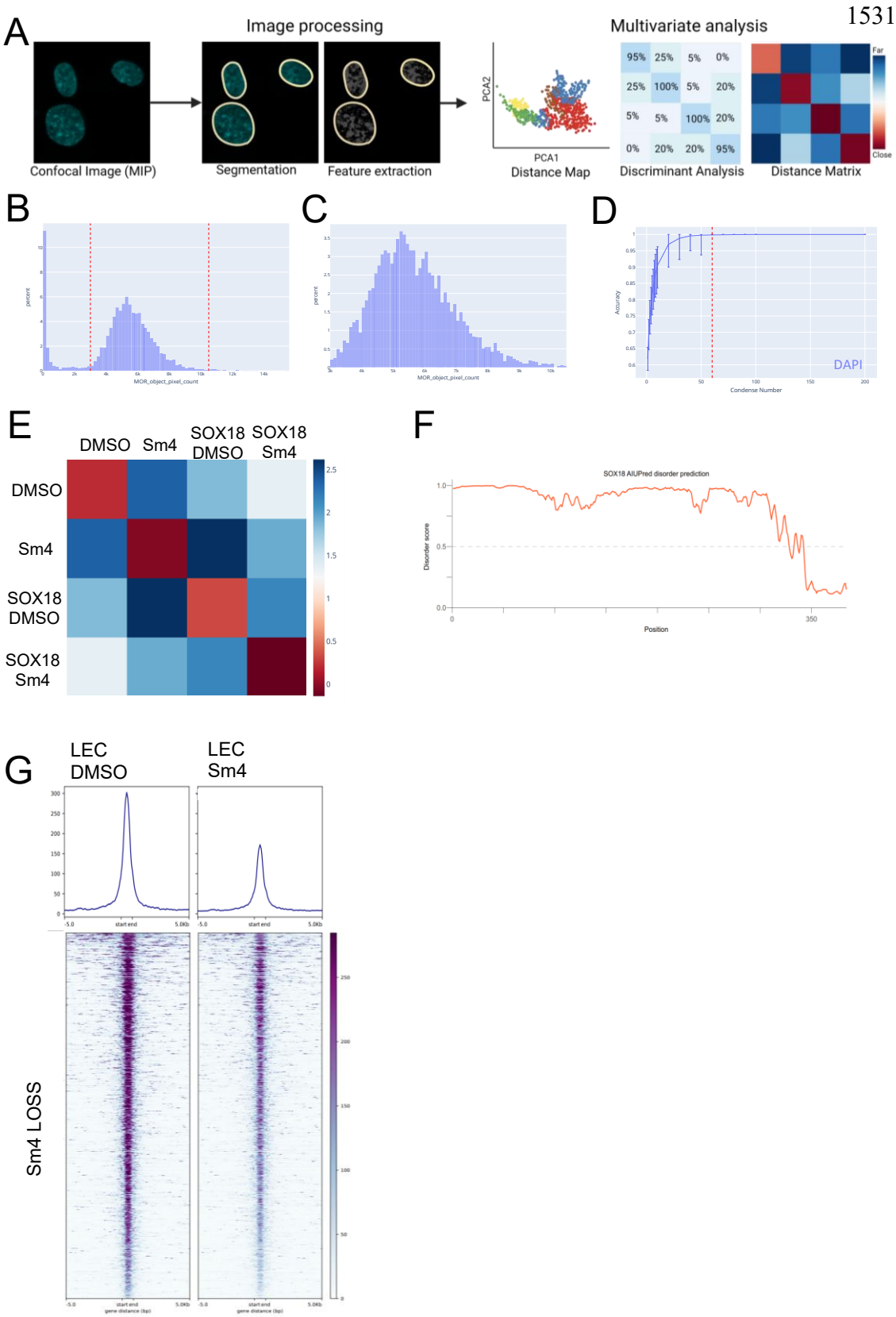

Supplementary Figure 2. Related to Fig 2.

A. Representative pipeline of unsupervised MIEL analysis. For each experimental condition, confocal images of the total cell population are acquired and separated by fluorescence channel. Individual nuclei are segmented using DAPI staining as a mask. Within each segmented nucleus, 253 texture-

and edge-based fluorescent features are extracted at the pixel level. These features are computed using the intensity relationships between each pixel and its surrounding neighbors, capturing spatial variation in signal distribution. The variation in the extracted nuclear features is quantified across all nuclei, and dimensionality reduction is performed using Principal Component Analysis (PCA). The top two principal components are used to visualize data structure and spread in a 2D PCA plot. To classify cell populations, a Support Vector Machine (SVM) algorithm is applied, enabling the identification of distinct clusters based on feature signatures. The average pairwise distances points in PCA space are then computed and represented as a similarity matrix. **B-C.** HUVECs ± SOX18 over-expression and ± Sm4 treatment stained with DAPI. **B.** Histogram displaying distribution of all object sizes (pixels) identified during segmentation, objects inside of red-dashed lines are used in analysis and **C.** zoom in on dashed lines in right panel. **D.** Line plots show accuracy measurements versus cell condense number; 95% confidence intervals are shown with red dotted line denotes smallest condense number above 95% accuracy. **E.** Average distance matrix calculated from the distance between each point per condition, with blue as farthest distances and red as closest distances. **F.** Intrinsic disorder prediction using AIUPred for SOX18 transcription factor (Uniprot ID: P35713). Y-axis represents the disorder prediction score and x-axis amino acid position. Scores over 0.5 (dashed line) are considered disordered. **G.** LECs treated with DMSO or Sm4 and subjected to ATAC-seq. Heatmap showing chromatin accessibility loss on the top 1000 sites of host genome (dark blue maps and line) upon Sm4 treatment.

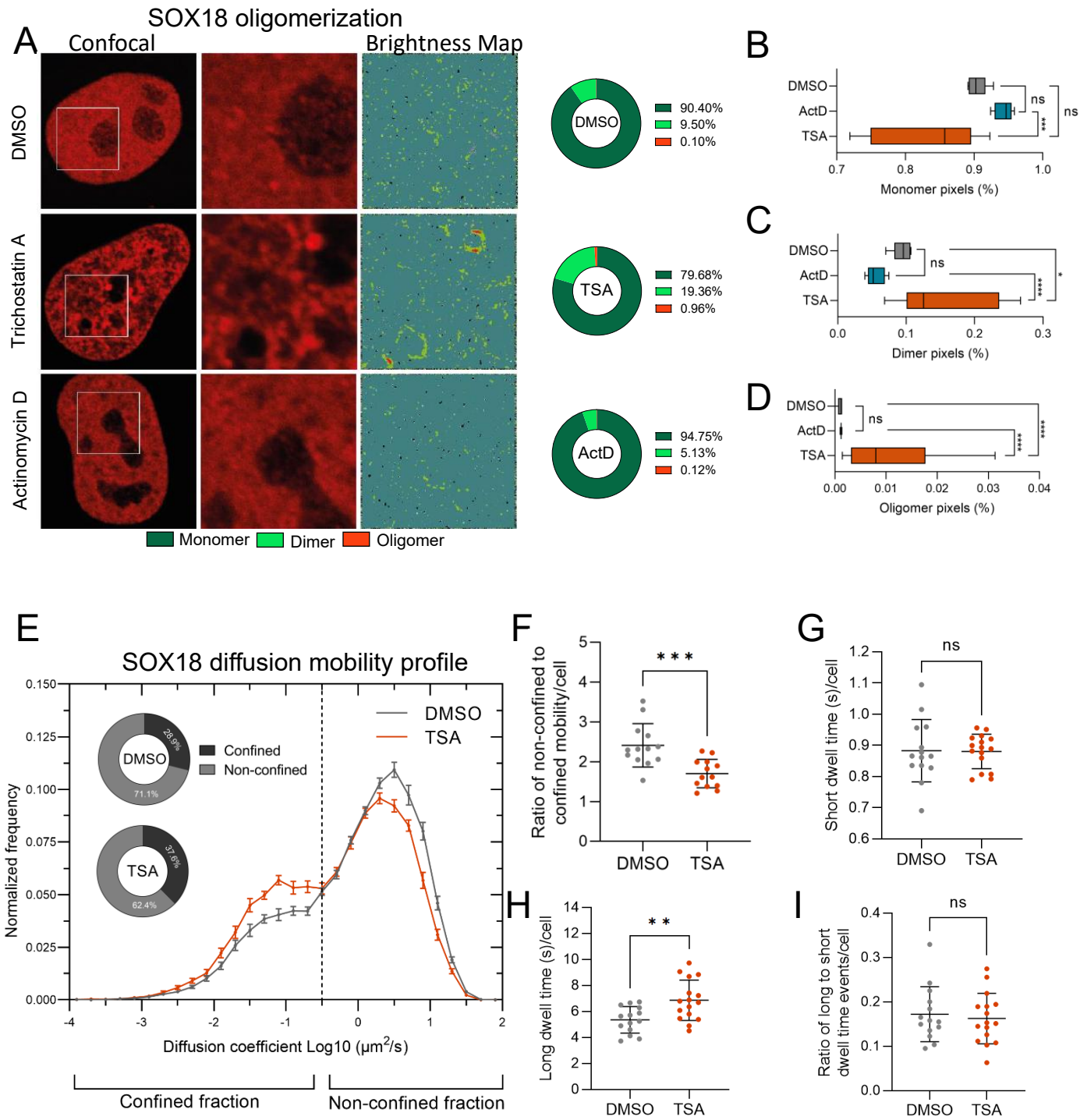

Figure 3. Chromatin compaction state feedback on SOX18 mobility and oligomeric states.

A. Representative images and maps of SOX18 oligomeric states (monomer – dark green, dimer – light green, and oligomer – red) of HeLa cells transfected with SOX18 and treated with either DMSO, Actinomycin D (ActD), or Trichostatin A (TSA) and measured by N&B. **B-D.** Quantification of oligomeric states by N&B. For panels B-D, n > 5 cells, statistical significance was determined by by one-way ANOVA with a Dunnett correction for multiple comparisons, *p < 0.05, **p < 0.01, ****p < 0.0001. **E.** Diffusion mobility graph from single molecule tracking

(SMT) acquisition comparing SOX18 mobility in HeLa cells that are transfected with Halo-SOX18 and treated either with DMSO or TSA. Pie charts represent the proportion of the trajectory population that is found in either the confined or non-confined states based on its diffusion coefficient. **F.** Ratio of non-confined to confined molecules per cell from F. **G-I.** Temporal occupancy characteristics for HeLa cells transfected with Halo-SOX18 and treated with TSA as G) short occupancy time, H) long occupancy time, I) ratio of long to short occupancy times. For panels G-I, n > 13 cells, statistical significance was determined by Welch's t-test, **$p < 0.01$, ***$p < 0.001$.

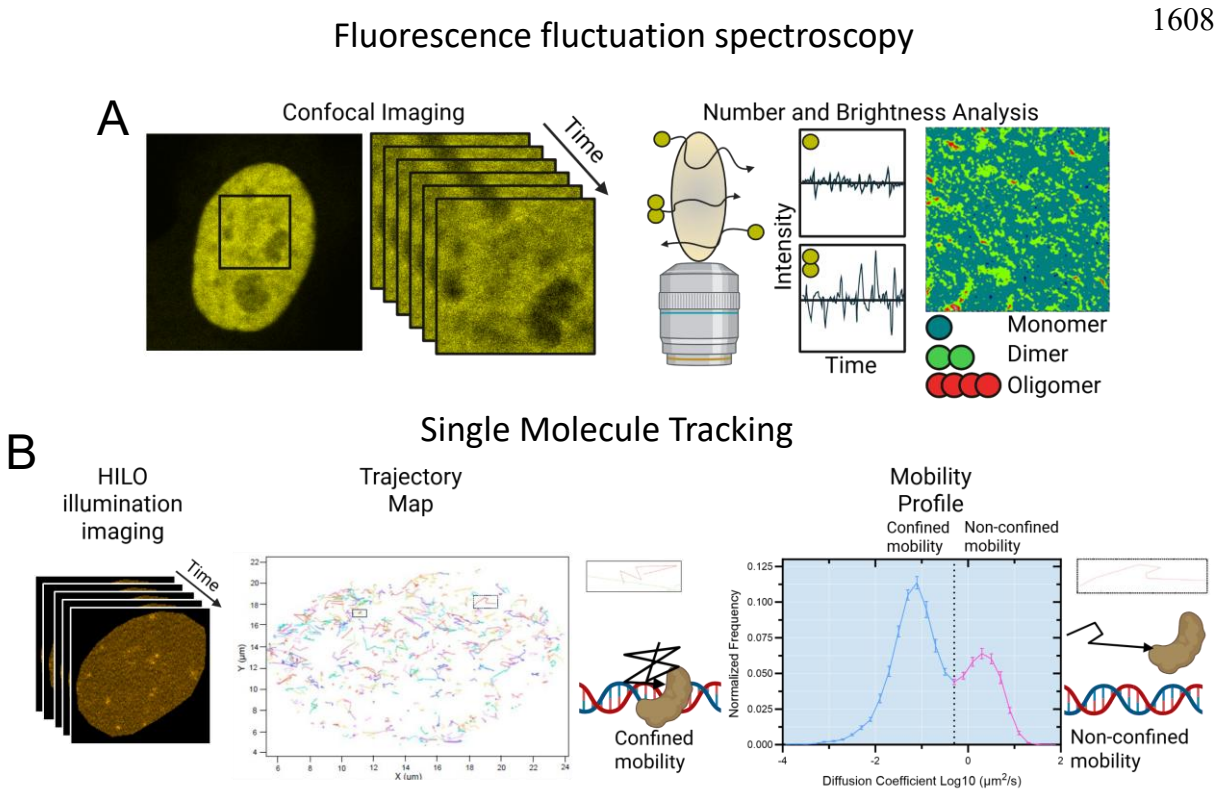

Supplementary Figure 3. Related to Fig 3.

A. Number and Brightness (N&B) analysis starts by identifying a cell and raster scanning to generate a confocal time series (100 frames). As the molecules move through the confocal volume the different oligomeric states will cause differences in fluorescence intensity. The intensity fluctuations are assessed over time and converted to fluctuations in molecular brightness for every pixel. The brightness is indicative of the average oligomeric state. In this way a dimer is twice as bright as a monomer and higher order oligomer are brighter than a dimer. **B.** Single molecule tracking (SMT) analysis starts by identifying a cell and imaging by highly inclined and laminated optical sheet (HILO) illumination to generate a time series (6000 frames). From the time series each Halo-tagged SOX18 molecule is identified per frame and stitched together to build a trajectory map. From each trajectory the diffusion coefficient is calculated as a measure of molecular mobility. Trajectories that have a low diffusion coefficient are defined as having a confined mobility (blue), whereas trajectories that have a higher diffusion coefficient are defined as being diffusive (non-confined mobility; pink). The diffusion coefficients are then graphed to assess the proportion of molecular populations that falls into either category.

SOX18 mobility and oligomeric state is effected by chromatin organization			
N&B (=PPI, oliogmeric status)	**Biophysical Observation**	**Biologlical interpretation**	**Fig**
ActD treatment relative to DMSO	No significant difference in the percentage of monomers and dimers, significant increase in oligomers	ActD treatment = loss of chromatin accessibility, leading to the loss of binding locations and subsequent decline in dimer formation.	Fig 3A-D
TSA treatment relative to DMSO	Significant increase in percentage of monomers & significant decrease in percentage of dimers, no significant difference in percentage of oligomers	TSA treatment = increase in chromatin accessibility, leading to increased binding locations and an increase in the dimer and higher order oligomer formation	Fig 3A-D
SMT (Diffusion)	**Biophysical Observation**	**Biologlical interpretation**	**Fig**
TSA treatment relative to DMSO: non-confined mobility (= target search pattern)	Significantly decreases	Increased chromatin accessiblity from TSA = more SOX18 molecules binding and less diffusing	Fig 3E-F
TSA treatment relative to DMSO: confined mobility (= PPI or protein-chromatin interaction)	Significantly increases		Fig 3E-F
SMT (Temporal occupancy)	**Biophysical Observation**	**Biologlical interpretation**	**Fig**
TSA treatment relative to DMSO: short occupancy (= searching behavior)	No significant differences	Increased chromatin accessiblity from TSA = SOX18 forming more dimers and higher order oligomers	Fig 3G-I
TSA treatment relative to DMSO: long occupancy (= PPI or protein-chromatin interaction)	Signficantly increases		Fig 3G-I
TSA treatment relative to DMSO: ratio of occupancy	No signifcant differences		Fig 3G-I

Table S1. Summary of biophysical experiments and biological interpretations.

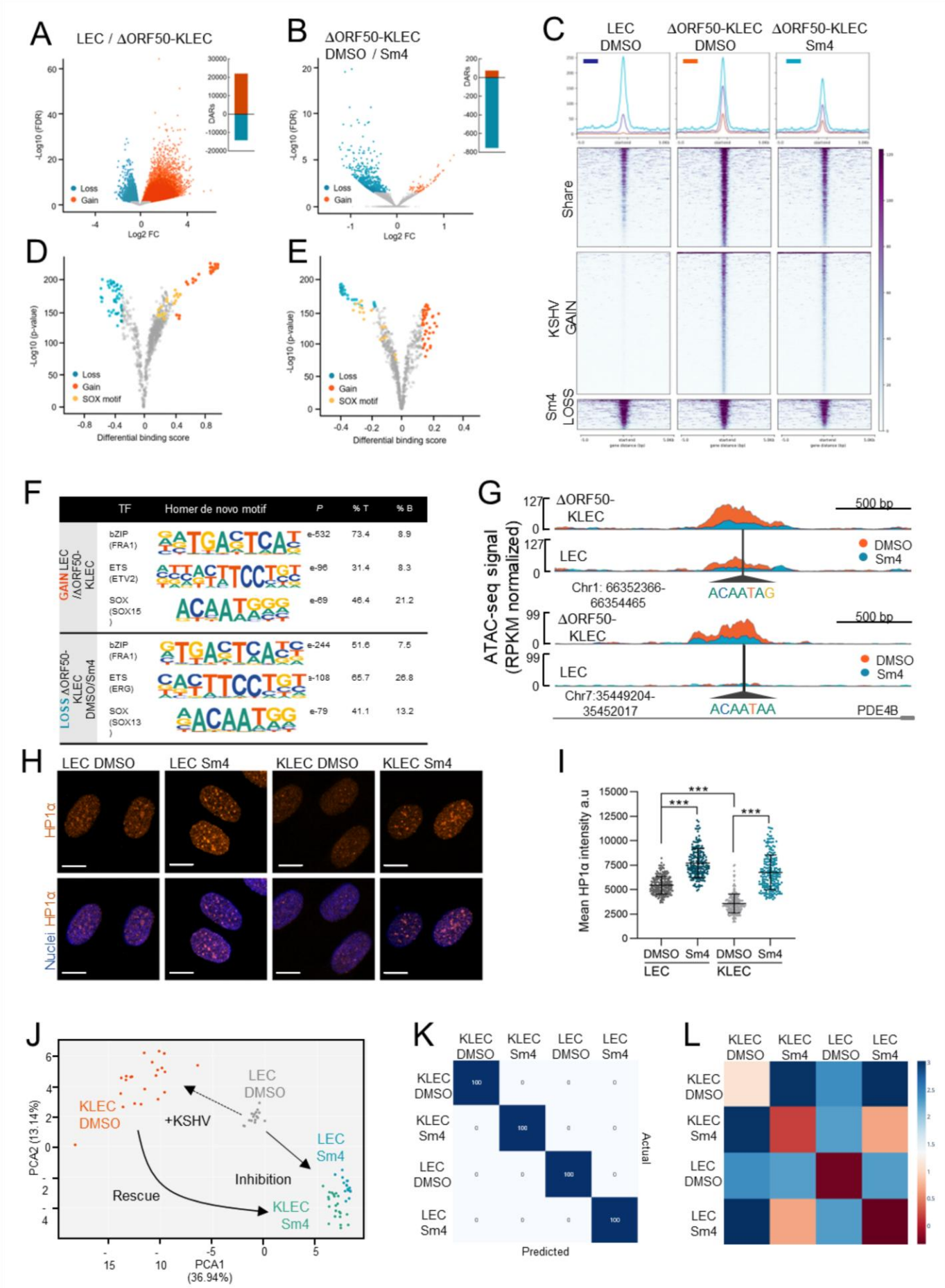
A
LEC / ΔORF50-KLEC
-Log10 (FDR)
Log2 FC
DARs
Loss
Gain
B
ΔORF50-KLEC
DMSO / Sm4
C
LEC DMSO
ΔORF50-KLEC DMSO
ΔORF50-KLEC Sm4
Share
KSHV GAIN
Sm4 LOSS
D
-Log10 (p-value)
Differential binding score
SOX motif
E
F
TF
Homer de novo motif
P
% T
% B
GAIN LEC /ΔORF50-KLEC
bZIP (FRA1)
e-532
73.4
8.9
ETS (ETV2)
e-96
31.4
8.3
SOX (SOX15)
e-69
46.4
21.2
LOSS ΔORF50-KLEC DMSO/Sm4
bZIP (FRA1)
e-244
51.6
7.5
ETS (ERG)
e-108
65.7
26.8
SOX (SOX13)
e-79
41.1
13.2
G
ΔORF50-KLEC
LEC
500 bp
DMSO
Sm4
ATAC-seq signal (RPKM normalized)
Chr1: 66352366-66354465
ACAATAG
Chr7:35449204-35452017
ACAATAA
PDE4B
H
LEC DMSO
LEC Sm4
KLEC DMSO
KLEC Sm4
HP1α
Nuclei HP1α
I
Mean HP1α intensity a.u
DMSO
Sm4
LEC
KLEC
J
KLEC DMSO
LEC DMSO
+KSHV
LEC Sm4
Inhibition
Rescue
KLEC Sm4
PCA2 (13.14%)
PCA1 (36.94%)
K
Actual
Predicted
L

1644 **Figure 4. KSHV hijacks SOX18 pioneer activity to increase chromatin accessibility in LECs.**
1645 **A-G.** Uninfected LECs (LEC) or LECs infected with KSHV-BAC16-ΔORF50 for 48h (ΔORF50-KLEC)
1646 were treated with DMSO or Sm4 for 24h and subjected for ATAC-seq. **A-B.** Volcano plots showing
1647 the human genomic regions with significant loss (turquoise) or gain (red) of accessibility upon A)
1648 KSHV infection and B) Sm4 treatment. **C.** Heatmap of the accessibility changes in the top 1000 sites
1649 upon KSHV infection (red line; KSHV gain), sites with accessibility loss after Sm4 treatment in
1650 ΔORF50-KLECs (light turquoise line; Sm4 loss) and sites with both accessibility gain upon infection
1651 and accessibility loss after Sm4 treatment (dark blue; shared). **D-E.** Volcano plots showing TF
1652 differential binding score prediction upon D) KSHV infection and E) Sm4 treatment in ΔORF50-
1653 KLECs. TFs with significant binding loss (turquoise), binding gain (red), and SOX family of TFs are
1654 marked (yellow). **F.** Top HOMER *de novo* transcription factor family motif enrichment gains upon
1655 infection and loss upon Sm4 treatment in ΔORF50-KLECs. **G.** Analysis of ATAC-seq peaks to show
1656 representative enhancer region with differential motifs and accessibility upon KSHV infection and
1657 SOX18 inhibition by Sm4 treatment in LECs and ΔORF50-KLECs. **H-I.** LECs infected with rKSHV.219
1658 for 72h (KLEC) and treated with DMSO or Sm4 for 24h were H) labeled with anti- HP1α antibodies
1659 and imaged with Zeiss LSM880 confocal 63x for heterochromatin regions, nuclei were counterstained
1660 with DAPI, scale is bar 10μm. I) The mean nuclear intensity a.u. (arbitrary units) of HP1α signal
1661 quantified (n=200). Statistical significance was determined by one-way ANOVA with a Tukey
1662 correction for multiple comparisons, ***$p < 0.001$. **J-K.** Quadratic discriminant MIEL analysis using
1663 texture features derived from images of LECs and KLECs treated with DMSO or Sm4 24h and stained
1664 with DAPI and anti-HP1α antibodies. **J.** Scatter plot depict the first two discriminant factors for each
1665 cell population. Each point is a pool of 60 cells. **K.** Matrix showing results for the discriminant analysis.
1666 Numbers represent the percent classified correctly (diagonal) and incorrectly (off the diagonal). **L.**
1667 Average distance matrix calculated from the distance between each point per condition, with blue as
1668 farthest distances and red as closest distances.

1669

1670

1671

1672

1673

1674

1675

1676

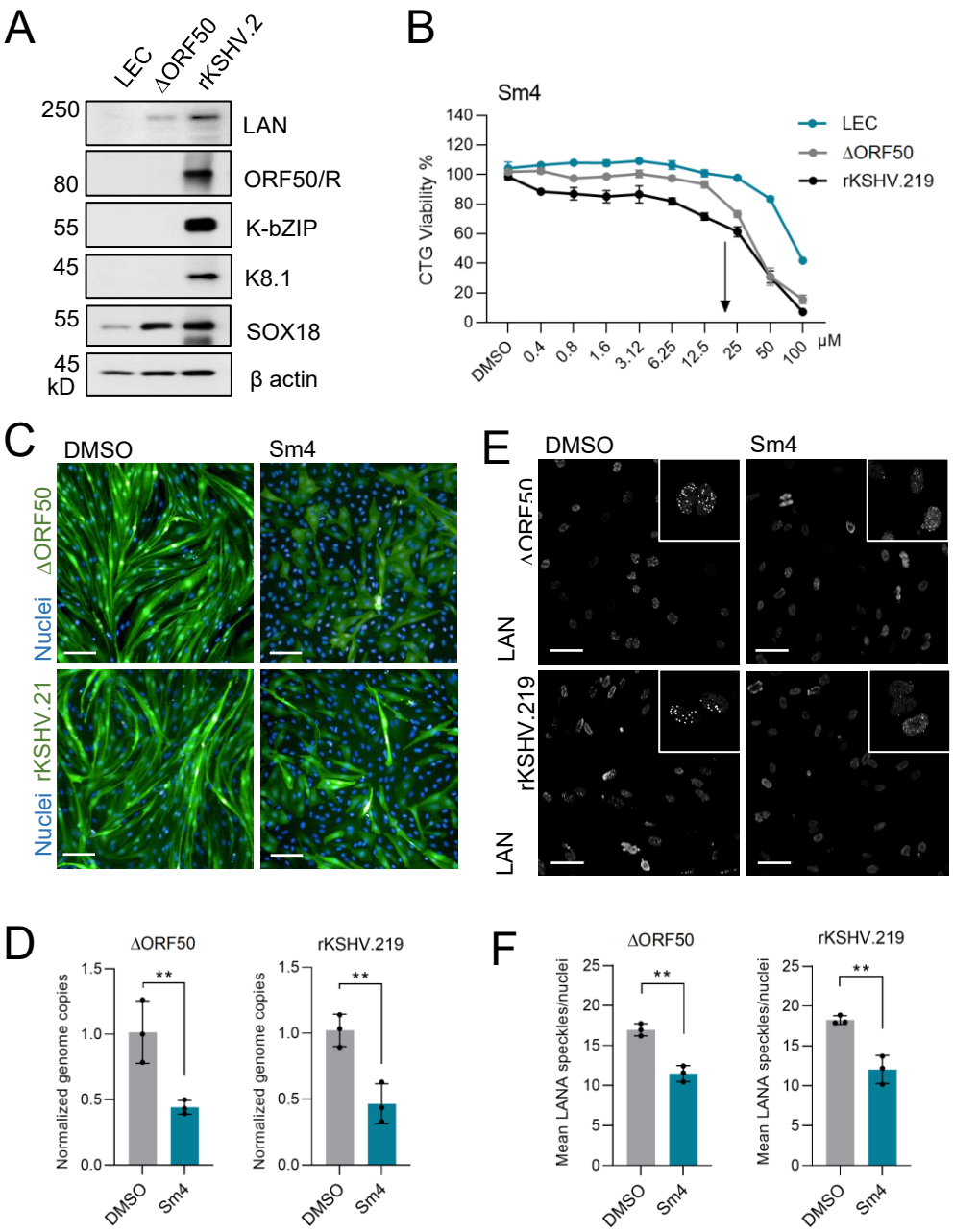

Supplementary Figure 4. Related to Fig 4.

A. LECs infected with latent KSHV-BAC16-ΔORF50 (ΔORF50-KLEC) or wildtype rKSHV.219 (rKSHV.219) for 72h and immunoblotted for the indicated viral proteins, and SOX18, using β-actin as a loading control. **B.** CTG viability assay of LECs infected with ΔORF50 or rKSHV.219 and treated with DMSO or with the indicated increasing Sm4 concentrations. **C-F.** Infection phenotypes of LECs infected with GFP-expressing ΔORF50-KLEC or rKSHV.219 and treated at 72h.p.i with Sm4 or DMSO control for 72h. **C.** GFP images of infected cells upon DMSO or Sm4 treatments. Nuclei were counterstained with Hoechst (33342), scale bar is 100μm. **D.** Relative KSHV DNA genome copies. **E.** Images of anti-LANA labeled infected cells and F) quantified as mean from 10 fields for each n=3 biological replicates. Nuclei were counterstained with Hoechst (33342), scale bar is 50μm. Statistical significance was determined by unpaired t-test, *$p < 0.05$, **$p < 0.01$.

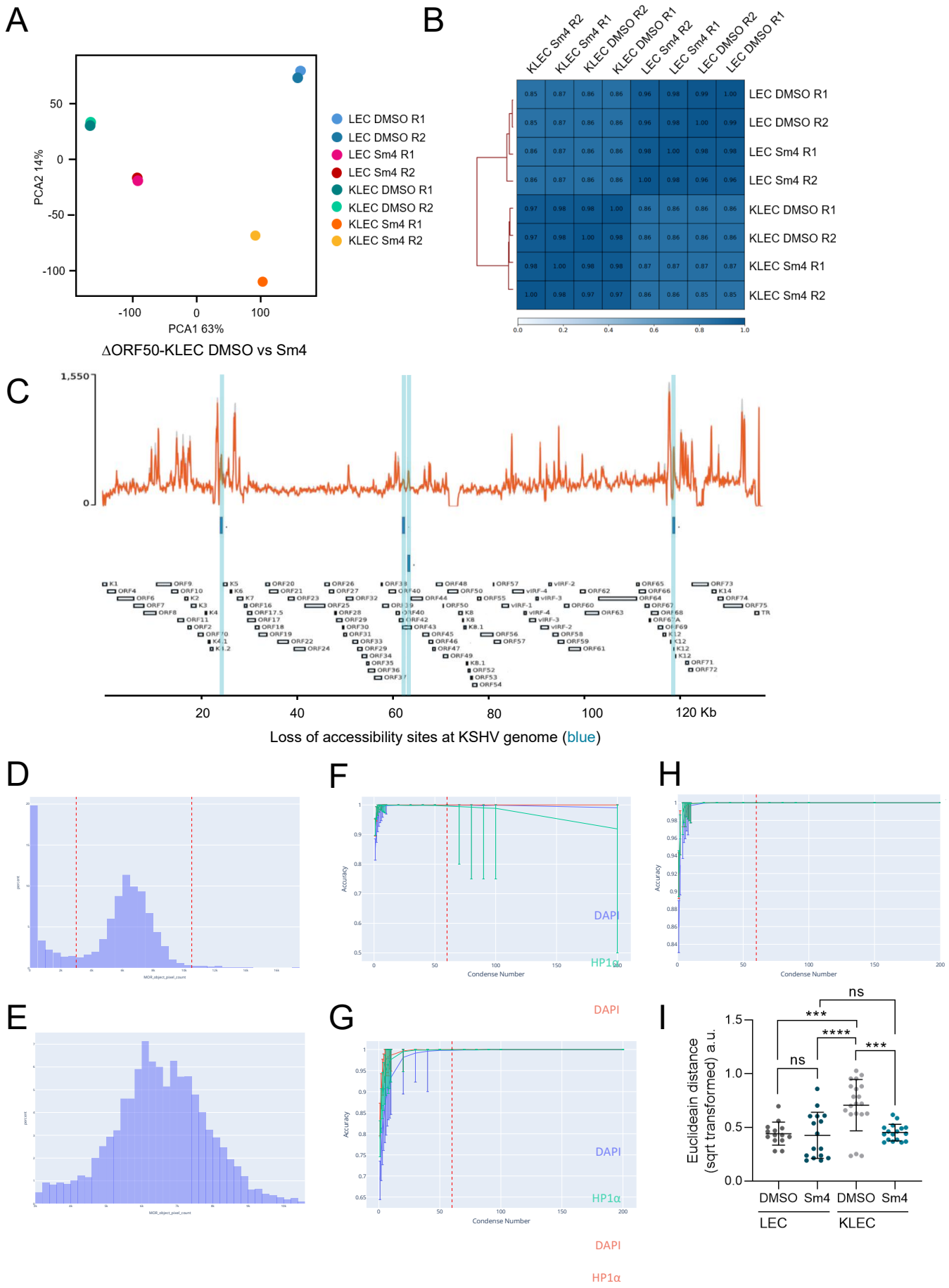
A
PCA2 14%
PCA1 63%
LEC DMSO R1
LEC DMSO R2
LEC Sm4 R1
LEC Sm4 R2
KLEC DMSO R1
KLEC DMSO R2
KLEC Sm4 R1
KLEC Sm4 R2
ΔORF50-KLEC DMSO vs Sm4
B
C
Loss of accessibility sites at KSHV genome (blue)
D
E
F
G
H
I
Condense Number
Accuracy
DAPI
HP1α
Euclideain distance (sqrt transformed) a.u.
DMSO
Sm4
LEC
KLEC
ns
***
****

1690 **Supplementary Figure 5. Related to Fig 4.**

1691 **A-C.** LECs infected with KSHV-BAC16-ΔORF50 (ΔORF50-KLEC) and treated with Sm4 or DMSO for
1692 24h and processed for ATAC-seq. **A.** Clustering and PCA analysis of the ATAC-seq data. **B.**
1693 Pearson's analysis of the replicate samples. **C.** Analysis of the ATAC-seq peaks on the KSHV genome
1694 in ΔORF50-KLECs treated with DMSO (grey) or Sm4 (red) indicating loss of accessibility sites (blue).
1695 **D.** Histogram displaying distribution of all object sizes (pixels) identified during segmentation, objects
1696 inside of red-dashed lines are used in analysis and **E.** zoom in on dashed lines in panel D. **F-H.** LEC
1697 and KLEC stained with DAPI and anti-HP1α antibody. Line plots showing accuracy measurements
1698 versus cell condense number, 95% confidence intervals are shown. **F.** Cell condensation between
1699 LEC and KLEC DMSO treatment. **G.** Cell condensation between LEC DMSO vs Sm4 treatment. **H.**
1700 Cell condensation between KLEC DMOS vs SM4 treatment **I.** Euclidean distances square root
1701 transformed of points from Fig 4L. n = 14 points or more. Statistical significance was determined by
1702 one-way ANOVA with Tukey correction for multiple comparisons, ***$p < 0.001$, ns = non-significant.

1703

1704

1705

1706

1707

1708

1709

1710

1711

1712

1713

1714

1715

1716

1717

1718

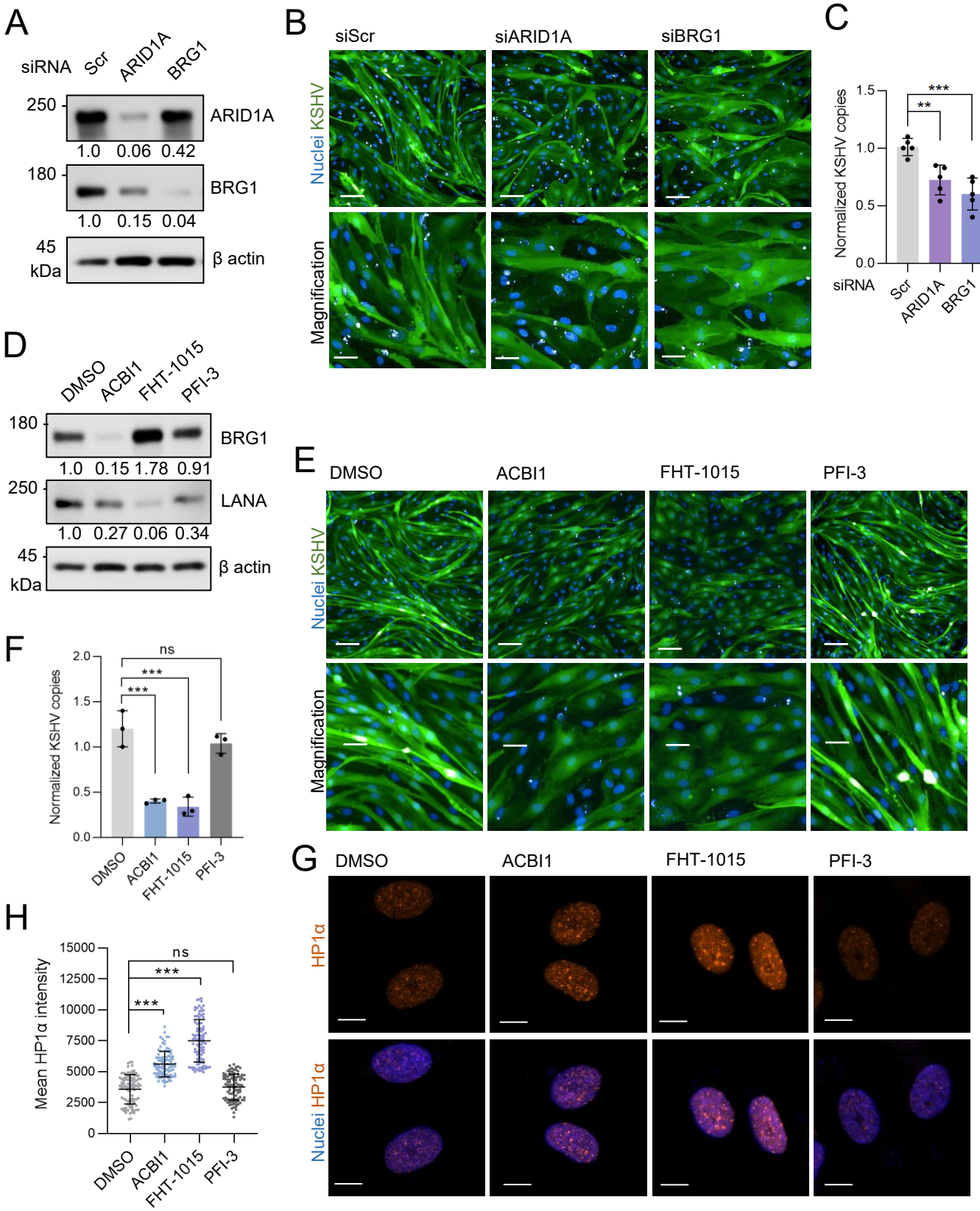
A
siRNA Scr ARID1A BRG1
250
ARID1A
1.0 0.06 0.42
180
BRG1
1.0 0.15 0.04
45
kDa
β actin
B
siScr
siARID1A
siBRG1
Nuclei KSHV
Magnification
C
Normalized KSHV copies
1.5
1.0
0.5
0.0
***
**
siRNA
Scr
ARID1A
BRG1
D
DMSO ACBI1 FHT-1015 PFI-3
180
BRG1
1.0 0.15 1.78 0.91
250
LANA
1.0 0.27 0.06 0.34
45
kDa
β actin
E
DMSO
ACBI1
FHT-1015
PFI-3
Nuclei KSHV
Magnification
F
Normalized KSHV copies
2.0
1.5
1.0
0.5
0.0
ns
***
***
DMSO
ACBI1
FHT-1015
PFI-3
G
DMSO
ACBI1
FHT-1015
PFI-3
HP1α
Nuclei HP1α
H
Mean HP1α intensity
15000
12500
10000
7500
5000
2500
0
ns
***
***
DMSO
ACBI1
FHT-1015
PFI-3

1722 **Figure 5. SWI/SNF ATPase activity is required for the hallmarks of KSHV infection in LECs.**
1723 **A-C.** LECs were transfected with siRNAs targeting ARID1A, BRG1 or scramble (siScr) as a control
1724 for 24h, and thereafter infected with rKSHV.219 for 72h (KLEC). **A.** Immunoblotting for ARID1A and
1725 BRG1, and β-actin as a loading control. **B.** GFP-expressing KLECs imaged with Opera Phenix 20x
1726 for changes in the cell spindling phenotype. Nuclei were counterstained with Hoechst (33342), scale
1727 bar 100 μm, in magnification 30μm. **C.** KLECs quantified for normalized KSHV episome genome
1728 copies by qPCR (n=5). **D-H.** LECs infected with rKSHV.219 for 72h were treated with SWI/SNF
1729 inhibitors ACBI1, FHT-1015 and PFI-3 for 72h. **D.** Immunoblotting of KLECs for the indicated host
1730 proteins and LANA, and β-actin as a loading control. **E.** GFP-expressing KLECs imaged with Opera
1731 Phenix 20x for changes in spindling phenotype. Nuclei were counterstained with Hoechst (33342),
1732 scale bar is 100μm, in magnification 30μm. **F.** KLECs quantified for normalized KSHV genome copies
1733 by qPCR (n=3). **G.** Inhibitor-treated KLECs were labeled forHP1α and imaged with LSM 880 confocal
1734 63x. Nuclei were counterstained with Hoechst (33342), scale bar is 10μm. **H.** The mean a.u. (arbitrary
1735 units) nuclear intensity of quantified HP1α signal (n=100 nuclei). Statistical significance was
1736 determined by one-way ANOVA with a Dunnett or Tukey correction for multiple comparisons, **$p < 0.01$,
1737 ***$p < 0.001$, ns = non-significant.

1738

1739

1740

1741

1742

1743

1744

1745

1746

1747

1748

1749

1750

1751

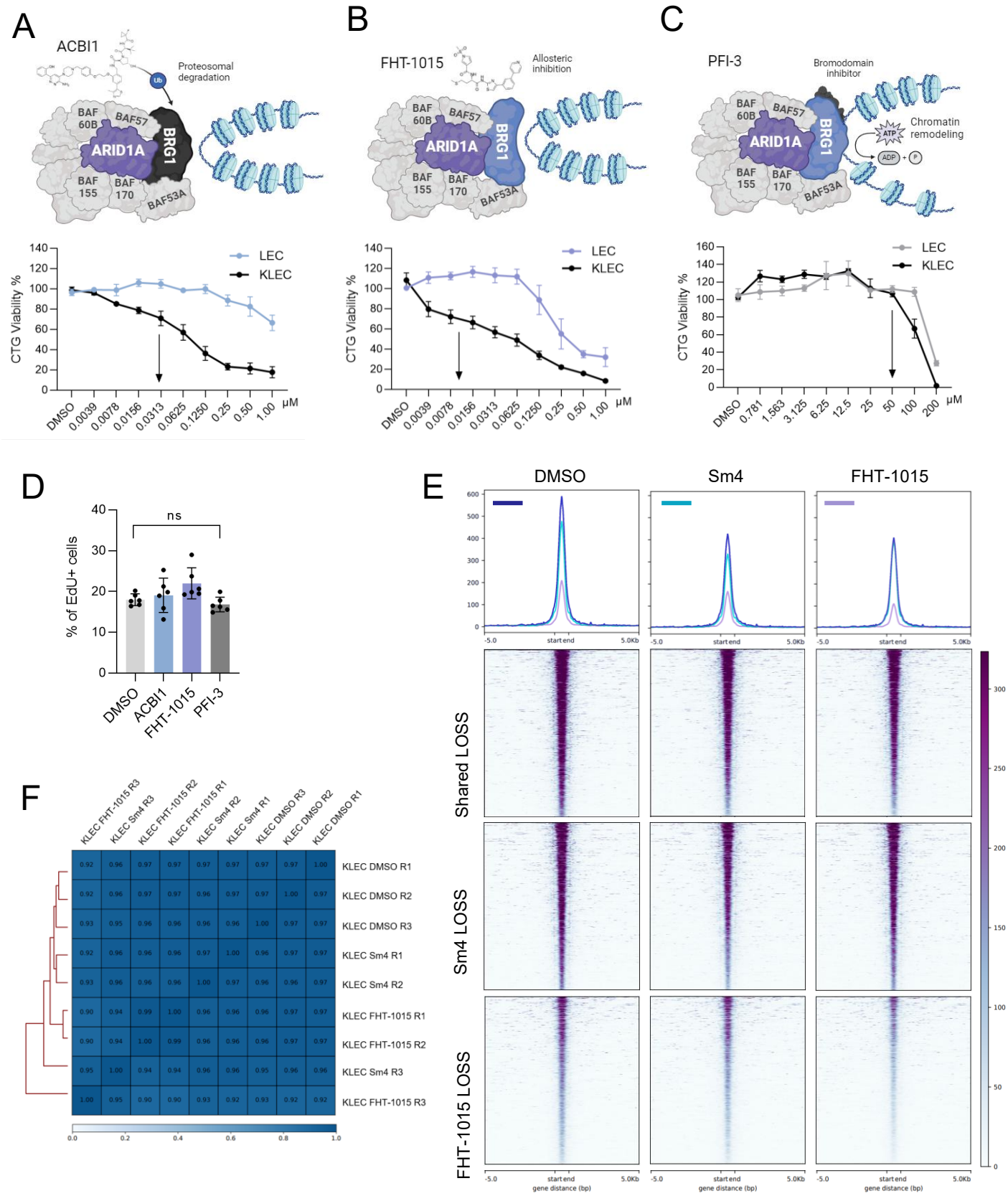

Supplementary Figure 6. Related to Fig 5.

A-C. A schematic of the inhibitor mode of action is shown in the top panels. CTG viability assay of uninfected LECs (LEC) or LECs infected with rKSHV.219 (KLEC) for 72h and treated with the

1756 indicated, increasing concentrations of BRG1 inhibitors A) ACBI1, B) FHT-1015 and C) PFI-3 (n=3),
1757 arrows indicate the selected concentration for following inhibitor assays. **D.** LECs and KLECs were
1758 treated with ACBI1 , FHT-1015 and PFI-3 and treated with EdU for 4h before subjecting to EdU Click-
1759 It, imaged with Opera Phenix 20x and quantified from (n=6 independent replicates, and from each
1760 n=100 nuclei). Statistical significance was determined by one-way ANOVA with Dunnett correction
1761 for multiple comparisons, ns = non-significant. **E-F.** LECs infected with ΔORF50 and treated with Sm4,
1762 FHT-1015, or DMSO for 72h and processed for ATAC-seq. **E.** Peaks and heatmaps of the top 1000
1763 genomic regions with reduced overall accessibility (dark blue maps) showing shared (dark blue line),
1764 unique to Sm4 (turquoise) and unique to FHT-1015 (purple) loss sites. **F.** Pearson's analysis of the
1765 replicate (n = 3) samples. ns = non-significant.

1766

1767

1768

1769

1770

1771

1772

1773

1774

1775

1776

1777

1778

1779

1780

1781

1782

1783

1784

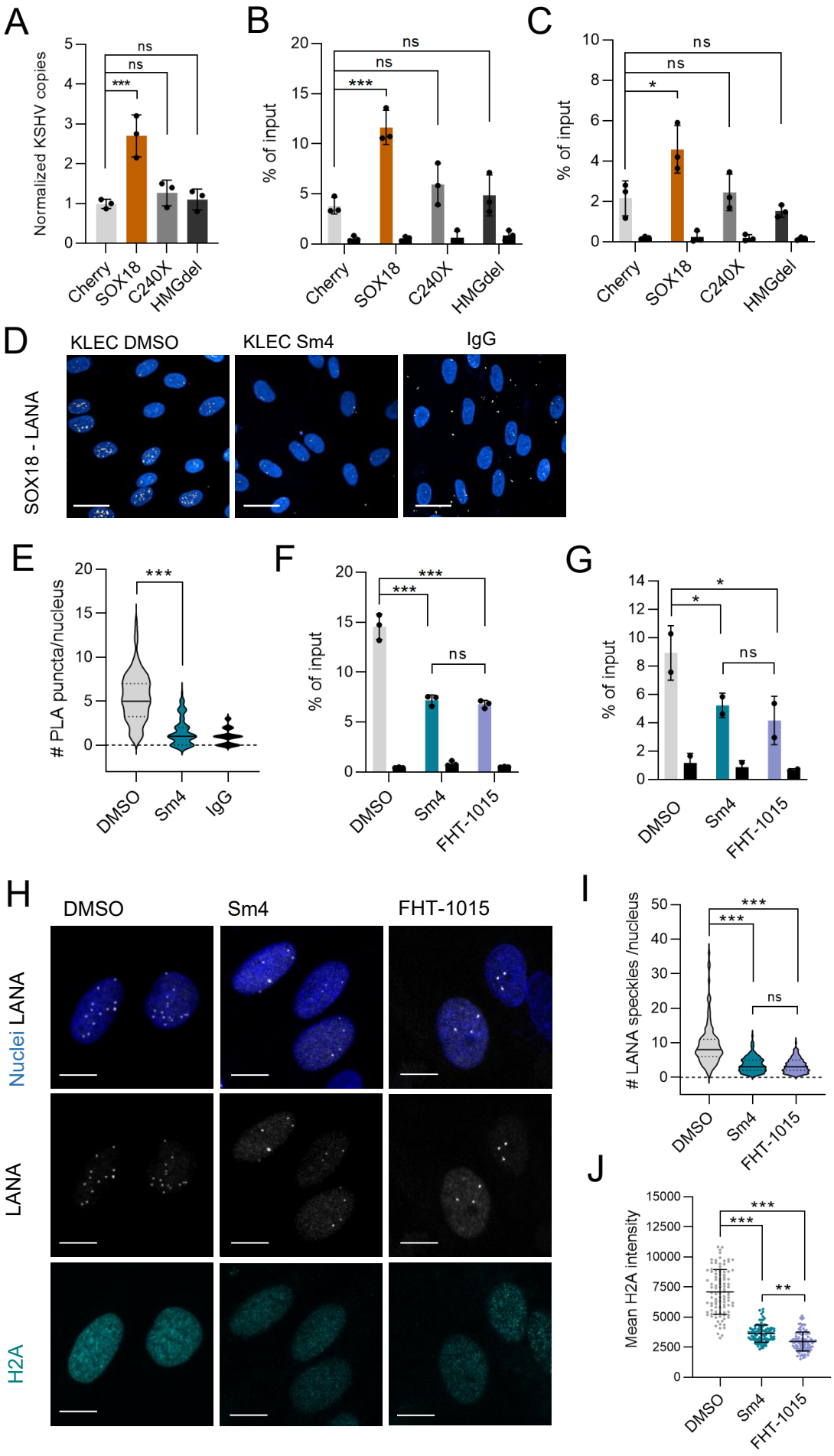
A
Normalized KSHV copies
ns
ns
***
Cherry
SOX18
C240X
HMGdel
B
% of input
ns
ns
***
Cherry
SOX18
C240X
HMGdel
C
% of input
ns
ns
*
Cherry
SOX18
C240X
HMGdel
D
KLEC DMSO
KLEC Sm4
IgG
SOX18 - LANA
E
PLA puncta/nucleus
***
DMSO
Sm4
IgG
F
% of input
***
***
ns
DMSO
Sm4
FHT-1015
G
% of input
*
*
ns
DMSO
Sm4
FHT-1015
H
DMSO
Sm4
FHT-1015
Nuclei LANA
LANA
H2A
I
LANA speckles /nucleus
***
***
ns
DMSO
Sm4
FHT-1015
J
Mean H2A intensity
***
***
**
DMSO
Sm4
FHT-1015

1786 **Figure 6. KSHV episome maintenance relies on a functional SOX18-BRG1 axis to increase**
1787 **LANA occupancy to KSHV TR.**
1788 **A-C.** HeLa cells expressing SOX18wt, mutants C240X (dominant negative transactivation deficient)
1789 or HMGdel (DNA-binding deficient), or mCherry as a control, and thereafter infected with rKSHV.219
1790 for 72h and A) measured for normalized KSHV genome copies by qPCR, B) subjected to ChIP-PCR
1791 with anti-LANA and IgG antibodies and analyzed for LANA binding at TR (n=3) or C) treated with
1792 BrdU for 4h and subjected to BrdU pulldown assay for nascent KSHV genome synthesis (n=3). **D-E.**
1793 KLECs treated with DMSO or Sm4 subjected to PLA assay using anti-SOX18 and anti-LANA
1794 antibodies, nuclei were counterstained with Hoechst (33342), D) imaged with Opera Phenix 40x,
1795 scale bar is 20μm and E) quantified as number of nuclear (n=100) PLA puncta (right panel). **F.** KLECs
1796 treated with DMSO, Sm4 or FHT-1015 for 24h were subjected to ChIP-PCR as described in B. (n=2).
1797 Two TR primers were used, and mean was taken for each replicate. **G.** KLECs treated with indicated
1798 inhibitors for 72h were subjected to BrdU pulldown assay as described in C (n=3). **H.** KLECs stained
1799 with anti-LANA and anti-H2A antibodies and imaged with LSM880 63x confocal, nuclei were
1800 counterstained with Hoechst (33342), scale bar is 10μm. **I-J.** Quantification of mean nuclear number
1801 of LANA speckles (n=100) and mean a.u. (arbitrary units) of H2A signal intensity (n=100). Statistical
1802 significance was determined by one-way ANOVA with Dunnett or Tukey correction for multiple
1803 comparisons, *$p < 0.05$, **$p < 0.01$, ***$p < 0.001$, ns = non-significant.
1804
1805
1806
1807
1808
1809
1810
1811
1812
1813
1814
1815
1816
1817
1818
1819
1820
1821
1822

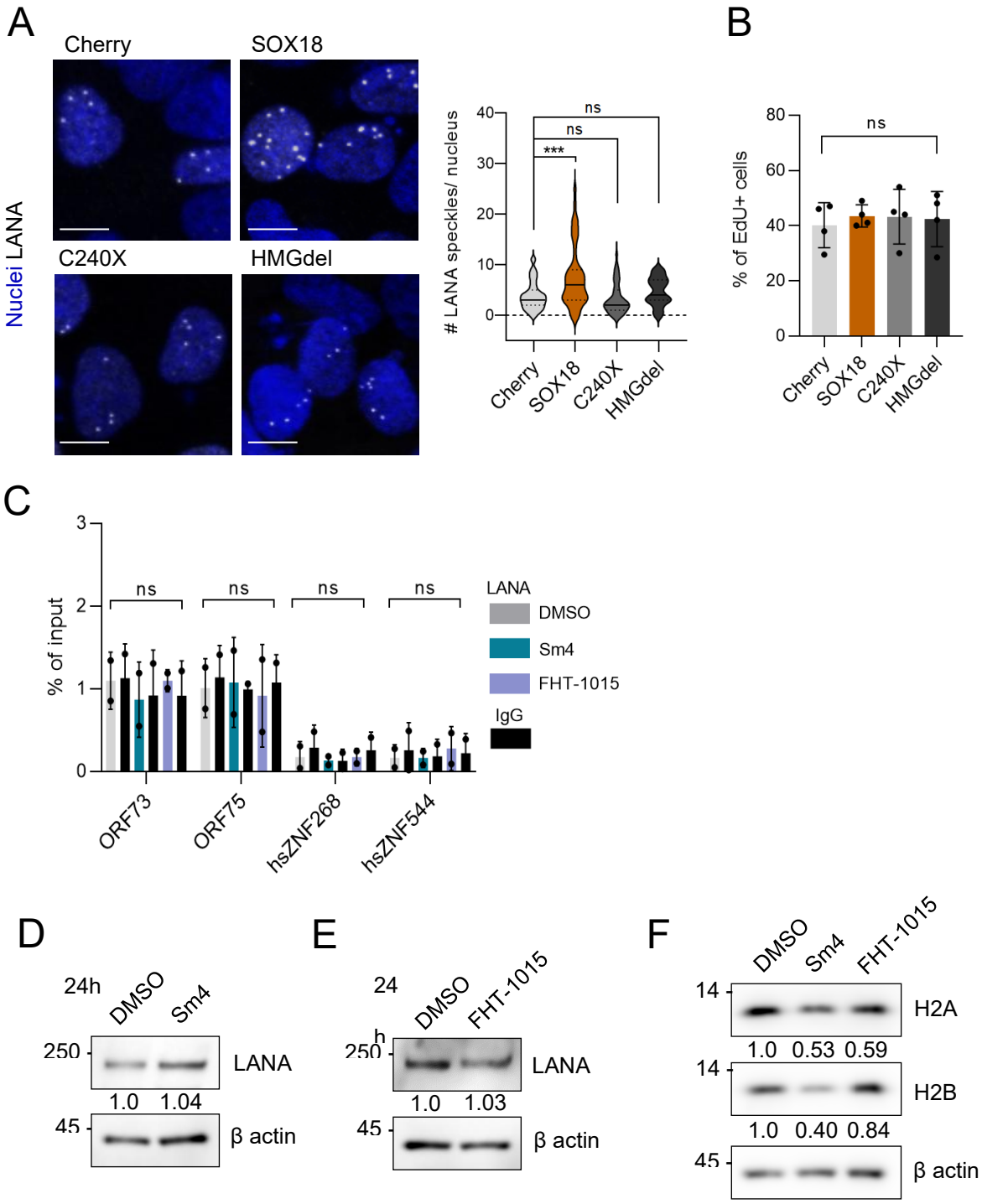

Supplementary Figure 7. Related to Fig 6.

A. Confocal images of LANA speckles (above panel) and quantified (bottom panel) as a number of nuclear speckles (n=50 nuclei), nuclei were counterstained with Hoechst (33342), scale bar is 10µm. **B.** HeLa cells expressing SOX18wt or the indicated mutants treated with EdU for 2h before fixing and subjected to EdU Click-It, imaged and quantified (n=4 independent replicates, and from each n=100 nuclei). **C-E.** LECs infected with rKSHV.219 for 72h were treated with DMSO, Sm4 or FHT-1015 for 24h and C) subjected to ChIP-PCR using anti-LANA and IgG antibodies for viral and human non-

1831 LANA binding control sites (n=2), and D-E) immunoblotted for LANA and β-actin as a loading control
1832 for normalization. **F.** KLECs treated for 72h and immunoblotted for H2A and H2B and quantified as in
1833 D-E. Statistical significance was determined by one-way ANOVA with either Dunnett or Tukey
1834 correction for multiple comparisons, ***$p < 0.001$, ns = non-significant.

1835